FELIPE MACHINI MALACHIAS MARQUES

Effects of Endowing Tilt-rotor Mechanisms in the Context of Multi-copters

UNIVERSIDADE FEDERAL DE UBERLÂNDIA
FACULDADE DE ENGENHARIA MECÂNICA

Janeiro - 2022

FELIPE MACHINI MALACHIAS MARQUES

Effects of Endowing Tilt-rotor Mechanisms in the Context of Multi-copters

Phd Dissertation presented to the Mechanical Engineering Graduate Program of the Federal University of Uberlândia, as a fulfillment of the requirements for the degree of **DOCTOR IN MECHANICAL ENGINEERING**.

Focus Area: Solid Mechanics and Vibrations.

Advisor: Prof. Dr. Roberto Mendes Finzi Neto

UBERLÂNDIA - MG
Janeiro - 2022

Ficha Catalográfica Online do Sistema de Bibliotecas da UFU
com dados informados pelo(a) próprio(a) autor(a).

M357
2022

Marques, Felipe Machini Malachias, 1992-
Effects of Endowing Tilt-rotor Mechanisms in the Context of Multi-copters [recurso eletrônico] / Felipe Machini Malachias Marques. - 2022.

Orientador: Roberto Mendes Finzi Neto.
Tese (Doutorado) - Universidade Federal de Uberlândia, Pós-graduação em Engenharia Mecânica.
Modo de acesso: Internet.
Disponível em: http://doi.org/10.14393/ufu.te.2022.15
Inclui bibliografia.

1. Engenharia mecânica. I. Finzi Neto, Roberto Mendes ,1974-, (Orient.). II. Universidade Federal de Uberlândia. Pós-graduação em Engenharia Mecânica. III. Título.

CDU: 621

Bibliotecários responsáveis pela estrutura de acordo com o AACR2:

Gizele Cristine Nunes do Couto - CRB6/2091

UNIVERSIDADE FEDERAL DE UBERLÂNDIA
Coordenação do Programa de Pós-Graduação em Engenharia Mecânica
Av. João Naves de Ávila, nº 2121, Bloco 1M, Sala 212 - Bairro Santa Mônica, Uberlândia-MG, CEP 38400-902
Telefone: (34) 3239-4282 - www.posgrad.mecanica.ufu.br - secposmec@mecanica.ufu.br

ATA DE DEFESA - PÓS-GRADUAÇÃO

Programa de Pós-Graduação em:	Engenharia Mecânica				
Defesa de:	Tese de Doutorado Acadêmico, nº 319, COPEM				
Data:	11/02/2022	Hora de início:	14:00	Hora de encerramento:	18:30
Matrícula do Discente:	11813EMC012				
Nome do Discente:	Felipe Machini Malachias Marques				
Título do Trabalho:	Effects of Endowing Tilt-rotor Mechanisms in the Context of Multi-copters				
Área de concentração:	Mecânica dos Sólidos e Vibrações				
Linha de pesquisa:	Dinâmica de Sistemas Mecânicos				
Projeto de Pesquisa de vinculação:					

Reuniu-se por meio de videoconferência a Banca Examinadora, designada pelo Colegiado do Programa de Pós-graduação em Engenharia Mecânica, assim composta: Professores Doutores: Aldemir Aparecido Cavalini Júnior - FEMEC/UFU; Rogério Sales Gonçalves - FEMEC/UFU; Fabian Andres Lara Molina - UTFPR; Guilherme Vianna Raffo - UFMG; Roberto Kawakami Harrop Galvão - ITA; e Roberto Mendes Finzi Neto - FEMEC/UFU, orientador do candidato. Ressalta-se que os Prof. Roberto Mendes Finzi Neto, Aldemir Aparecido Cavalini Júnior, Rogério Sales Gonçalves e o Discente participaram da defesa por meio de videoconferência desde a cidade de Uberlândia/MG; Fabian Andres Lara Molina desde a cidade de Cornélio Procópio/PR; Guilherme Vianna Raffo desde a cidade de Belo Horizonte/MG e Roberto Kawakami Harrop Galvão desde a cidade de São José dos Campos/SP, em atendimento a Portaria nº 36, de 19 de março de 2020, da Coordenação de Aperfeiçoamento de Pessoal de Nível Superior - CAPES.

Iniciando os trabalhos, o presidente da mesa, Dr. Roberto Mendes Finzi Neto, apresentou a Comissão Examinadora e o candidato, agradeceu a presença do público, e concedeu ao Discente a palavra para a exposição do seu trabalho. A duração da apresentação do Discente e o tempo de arguição e resposta foram conforme as normas do Programa.

A seguir o senhor(a) presidente concedeu a palavra, pela ordem sucessivamente, aos(às) examinadores(as), que passaram a arguir o(a) candidato(a). Ultimada a arguição, que se desenvolveu dentro dos termos regimentais, a Banca, em sessão secreta, atribuiu o resultado final, considerando o(a) candidato(a):

Aprovado.

Esta defesa faz parte dos requisitos necessários à obtenção do título de Doutor.

O competente diploma será expedido após cumprimento dos demais requisitos, conforme as normas do Programa, a legislação pertinente e a regulamentação interna da UFU.

Nada mais havendo a tratar foram encerrados os trabalhos. Foi lavrada a presente ata que após lida e achada conforme foi assinada pela Banca Examinadora.

Documento assinado eletronicamente por **Roberto Mendes Finzi Neto**, **Professor(a) do Magistério Superior**, em 11/02/2022, às 18:32, conforme horário oficial de Brasília, com fundamento no art. 6º, § 1º, do Decreto nº 8.539, de 8 de outubro de 2015.

Documento assinado eletronicamente por **Aldemir Aparecido Cavalini Junior**, **Professor(a) do Magistério Superior**, em 11/02/2022, às 18:32, conforme horário oficial de Brasília, com fundamento no art. 6º, § 1º, do Decreto nº 8.539, de 8 de outubro de 2015.

Documento assinado eletronicamente por **Guilherme VIanna Raffo**, **Usuário Externo**, em 11/02/2022, às 18:33, conforme horário oficial de Brasília, com fundamento no art. 6º, § 1º, do Decreto nº 8.539, de 8 de outubro de 2015.

Documento assinado eletronicamente por **Roberto Kawakami Harrop Galvão**, **Usuário Externo**, em 11/02/2022, às 18:33, conforme horário oficial de Brasília, com fundamento no art. 6º, § 1º, do Decreto nº 8.539, de 8 de outubro de 2015.

Documento assinado eletronicamente por **Rogerio Sales Gonçalves**, **Professor(a) do Magistério Superior**, em 11/02/2022, às 18:33, conforme horário oficial de Brasília, com fundamento no art. 6º, § 1º, do Decreto nº 8.539, de 8 de outubro de 2015.

Documento assinado eletronicamente por **Fabian Andres Lara Molina**, **Usuário Externo**, em 11/02/2022, às 18:33, conforme horário oficial de Brasília, com fundamento no art. 6º, § 1º, do Decreto nº 8.539, de 8 de outubro de 2015.

A autenticidade deste documento pode ser conferida no site https://www.sei.ufu.br/sei/controlador_externo.php?acao=documento_conferir&id_orgao_acesso_externo=0, informando o código verificador **3340018** e o código CRC **2F7A150A**.

ACKNOWLEDGEMENTS

First, I acknowledge the Federal University of Uberlândia where I have spent excellent years of my life. To the funding agency CAPES and UFU Mechanical Engineering Graduate Program for financial support and technical assistance.

I would like to acknowledge Prof. Dr. Roberto Mendes Finzi Neto for the hours dedicated to my mentoring and all the support given which made this project feasible.

I'm also grateful to Prof. Dr. Shawn Keshmiri, from the University of Kansas, for presenting me the beauty of Flight Dynamics and Control during my undergraduate period. Your inspiring lessons and our research project encouraged me to study further the subject.

I sincerely want to express my gratitude to Dr. Leonardo Sanches who accepted my challenge to start a project in UAVs at UFU from scratch. His dedication, character and passion for science have not only inspired me but guided my career. Thank you Leo for always being questioning me, for believing in my potential, for your friendship and for all your contributions to the academia.

To all the people involved in the Autonomous Flight Laboratory at UFU. Thank you Vitor, Gabriel Henrique, Bruno, Ivan, Matheus Jerônimo, Matheus Amarante and Douglas for your contribution to the research. It was a great pleasure to work with you guys. I dedicate a special thank to Prof. Dr. Pedro Augusto Queiroz de Assis for his friendship and the partnership in this project. Thank you Pedro for disposing from all the knowledge about MPC to contribute to this research.

To my family, Pedro, Deisi, João Pedro for your backup and for motivating me during all my academic years. To Flávia, my beloved partner, who consistently teaches me how to appreciate and enjoy life and has always encouraged my plans. Thank you all for being on my side all the way through.

To every person who believe, experiment, dedicate and contribute to science.

“Drop the idea of becoming someone, because you are already a masterpiece. You cannot be improved. You have only to come to it, to know it, to realize it.” - OSHO

MARQUES, F. M. M. 2022. **Effects of Endowing Tilt-rotor Mechanisms in the Context of Multi-copters**, Federal University of Uberlândia, Uberlândia.

ABSTRACT

Standard fixed-rotor multi-copters are classified as underactuated systems. For such cases, position and attitude control cannot be achieved independently due to the number of control inputs. To overcome this, novel multi-copter designs containing vectoring thrust mechanisms have been studied. This strategy, denominated tilt mechanism, has been widely employed on bi-copters, tri-copters, quad-copters and hexa-copters. In this context, this study concerns the dynamical modeling of a tilting rotor multi-copter aerial vehicle capable of tilting its motors laterally. Based on that, the control decoupling properties of the model are explored emphasizing the trade-off between mechanical complexity versus system maneuverability and controllability. For this, a tilt-rotor bi-copter test bench is developed for model and control validation. Then, two control design formulations are proposed and validated experimentally. First, the Linear Quadratic Tracking (LQT) is employed for trajectory tracking considering fixed and tilt-rotor configurations. In the sequel, a Model Predictive Controller (MPC) is designed for position tracking considering tilt deflection limitations, actuator dynamics and control decoupling between attitude and horizontal displacement. The results have shown that the tilt mechanism dynamics have major influence in lateral motion of the multi-copter. Moreover, the MPC dynamic decoupling control strategy presented some improvement over the LQT controller being able to properly handle the tilt-deflection constraints.

Keywords: *Multi-copters, Tilt-rotor, Unmanned Aerial Vehicle (UAV), Model Predictive Control (MPC), Linear Quadratic Regulator (LQR)*

MARQUES, F. M. M. 2022. **Efeitos da Inclusão de Mecanismos *Tilt-rotor* no Contexto de Multirrotores**, Universidade Federal de Uberlândia, Uberlândia.

RESUMO

Em geral, multirrotores com rotores fixos são classicados como sistemas subatuados. Nesses casos, o número de variáveis de controle torna inviável realizar o controle de posição e atitude de forma independente. A fim de reverter esse cenário, novas configurações de multirrotores contendo mecanismos de vetorização de empuxo têm sido estudadas. Essa estratégia, denominada *tilt-rotor*, vêm sendo empregada em bicópteros, tricópteros, quadcópteros e hexacópteros. Nesse contexto, o presente estudo trata da modelagem dinâmica e controle de um veículo multirrotor *tilt-rotor* capaz de rotacionar seus motores lateralmente. Assim, busca-se explorar as propriedades de desacoplamento de controle do sistema enfatizando a ponderação entre complexidade mecânica versus a controlabilidade e manobrabilidade do veículo. Para isso, é proposto o desenvolvimento de uma bancada contendo um bicóptero *tilt-rotor* para validação do modelo e leis de controle. Então, duas formulações de controle são propostas e validadas experimentalmente. A primeira delas é baseada na técnica *Linear Quadratic Tracking* (LQT) empregada para rastrear um sinal de referência considerando configurações com rotores fixos e *tilt*. Em seguida, projeta-se o controlador a partir da concepção do *Model Predictive Control* (MPC) para rastreamento de posição considerando limitações nas deflexões do *tilt*, a dinâmica do atuador e o desacoplamento de controle entre deslocamento horizontal e atitude. Os resultados obtidos mostram que a dinâmica do mecanismo de vetorização de empuxo tem grande influência sobre o movimento lateral do multirrotor. Ainda, a estratégia de desacoplamento de controle junto com a técnica MPC apresentou melhorias significativas sobre o LQT tendo em vista a sua capacidade de gerenciar as restrições de deflexão do mecanismo *tilt*.

Palavras Chave: *Multirrotores, Vetorização de Empuxo, Veículos Aéreos Não Tripulados (VANTs), Controle Preditivo, Regulador Linear Quadrático*

LIST OF FIGURES

LIST OF TABLES

LIST OF SYMBOLS

Latin Symbols

a	angle between two consecutive z joint axes measured with respect to x
$\mathbf{A}$	state-space state matrix
b	propeller drag constant
$\mathbf{B}$	state-space input matrix
c	joint disbalance
$\mathbf{C}$	state-space output matrix
$\mathbf{d}$	distance vector from motor to the vehicle CG
$\mathbf{e}$	error vector
ef	actuator or state effectiveness
ENC	rotary encoder sensor
f	motor thrust force
$\mathbf{F}$	Force vector
$\mathbf{H}$	Angular momentum vector
I_{xx}	vehicle inertia about x axis
I_{yy}	vehicle inertia about y axis
I_{zz}	vehicle inertia about z axis
J	cost performance index
$\mathbf{J}_{\bullet}^{\star}$	Jacobian matrix of element “$\bullet$” in frame “$\star$”

l	element length
L	multi-copter arm length
$\mathbf{L}$	state observer gain matrix
$\mathscr{L}$	Lagrangian
k	sample
$\mathbf{K}$	control gain matrix
$\mathscr{K}$	kinetic energy
k_p	propulsive set constant
m	element mass
$\mathbf{M}$	Moment vector
n_c	number of desired tracking variables
n_e	number of state observer variables to estimate
n_m	number of measured states
n_s	number of states
n_u	number of control variables
n_y	number of outputs
N_x	state prediction horizon
N_u	control horizon
$O_\bullet$	origin of reference frame “$\bullet$”
$\mathbf{O}_{\bullet\times\star}$	“$\bullet$” by “$\star$” zero matrix
$\mathscr{P}$	potential energy
$\mathbf{q}$	joints angular position vector or generalized coordinates
$\mathbf{Q}$	state weighting matrix
r	distance between joints axes
$\mathbf{r}$	reference vector
$\mathbf{R}$	control weighting matrix

$\mathbf{R}_\bullet^\star$	rotation matrix from reference system “•” to “⋆”
$\mathbf{t}_e^0$	forces and moments tensor applied by the manipulator end-effector
T_s	sample time
$\mathbf{T}_\bullet^\star$	homogeneous transformation matrix from reference system “•” to “⋆”
$\mathbf{u}$	input vector
$x_\bullet$	x direction in “•” reference frame
$\mathbf{x}$	state vector
$y_\bullet$	y direction in “•” reference frame
$\mathbf{y}$	output vector
$z_\bullet$	z direction in “•” reference frame
$\mathbf{z}$	augmented state vector
z_{CG}	motor vertical distance from the CG
$\mathbf{1}_{\bullet\times\star}$	“•” by “⋆” identity matrix

Greek Symbols

α	longitudinal tilt angle
β	lateral tilt angle
$\boldsymbol{\chi}$	test-bench state vector
γ	motor angular position with respect to body coordinate frame
$\boldsymbol{\gamma}$	test-bench output vector
Γ	generalized force
ω	vehicle angular velocity vector
Ω	motor set propeller angular speed
μ	joint friction
$\nu_\bullet^\star$	kinematic tensor of joint “⋆” with respect to frame “•”

$\sigma_{\bullet}^{\star}$	position vector of point "$\bullet$" of a component written in frame "$\star$"
$\theta_{\bullet}$	test bench rotation about joint "$\bullet$"
τ	thrust torque
$\boldsymbol{\upsilon}$	test-bench control vector

Acronyms

ABS	Acrylonitrile Butadiene Styrene
ADC	Analog-To-Digital
AFL	Autonomous Flight Laboratory
BCS	Body Coordinate System
CAD	Computer Aided Design
CCW	Counter-clockwise
CG	Center of Gravity
CW	Clockwise
CNC	Computer Numeric Control
DH	Denavit Hatenberg
DOF	Degrees of Freedom
ESC	Eletronic Speed Controller
HIL	Hardware-in-the-loop
HTOL	Horizontal Take-Off and Landing
IMU	Inertial Measuring Unit
I/O	Input/Output board pin
LQR	Linear Quadratic Regulator
LQT	Linear Quadratic Tracking
LTI	Linear Time Invariant
MAV	Micro Aerial Vehicle
MCS	Motor Coordinate System

MPC	Model Predictive Control
PC	Personal Computer
PWM	Pulse Width Modulation
SSH	Secure Shell communication protocol
TRBC	Tilt-Rotor Bi-Copter
UAV	Unmanned Aerial Vehicle
VTOL	Vertical Take-Off and Landing
ZOH	Zero Order Holder

CHAPTER I

Introduction

1.1 Background and motivation

In the last decade, Unmanned Aerial Vehicles, also known as UAVs or simply drones, have witnessed a substantial growth in different branches. Similarly to the internet and GPS before them, UAVs have surpassed their initial military purposes to become a potential business asset. At first sight, this novel technology had been seen as an alternative to create more safe, affordable and efficient aircraft. In this context, they should be able to accomplish the same tasks as manned vehicles with relative better performance. Nonetheless, UAV's versatility and miniaturization capacity have drawn the attention of the research community and business market for specific tasks that were previously unfeasible. Nowadays, these vehicles category has spread in many civilian application branches as: firefighting, construction, remote sensing, filming, product delivery, crop dusting, among others.

Regarding the ascending UAV technology, there is an increasing demand for more compact, versatile and efficient aerial vehicles. Therefore, among all the UAV classifications based on size and applications, a category which has been gaining prominence are the Micro Aerial Vehicles (MAVs). They can be defined as small scale UAVs capable of performing autonomous flight, generally employed in low range missions. One of the major advantage of the MAVs are their miniaturization capacity and ability to operate indoor or spatially restricted environments.

Even though many research efforts have been focused on the development of more suitable UAVs, design and operational features can still be optimized. Recently, a myriad of design improvements have been proposed in order to accomplish the requirements of endurance, range, maneuverability, cost, energy per mass relation and autonomous flight capacity.

For instance, distinct control techniques for vehicle stabilization or trajectory tracking have been studied to enhance the system robustness considering operational disturbances, sensor noise and model uncertainties. Furthermore, the development of more compact, light and efficient electronics can be profitable for new MAV designs. Mutually, other researches investigate different possibilities of actuation mechanisms which could be used for flight quality enhancement. One of these options is the tilt-rotor configuration which consists on vectoring the motor thrust force in different directions by using a proper actuation mechanism.

The tilt-rotor problematic on multi-copters rises intriguing questions about the system's dynamics and controllability. For instance, adding extra control degrees of freedom can be profitable to overcome underactuation and reduce motor control effort. Moreover, the vehicle can have more than one equilibrium point, being able to hover on a non-horizontal condition where roll and pitch angles are not zero. Nonetheless, the tilt dynamics increases the systems complexity, introducing non-linearities and coupling terms, affecting directly the vehicle response. In this sense, it is convenient for the designer, to account for the trade-off between mechanical complexity and system performance.

1.2 Aims and objectives

Considering this scenario, in regard to the tilt rotor state of art, the present study aims to explore the tilt mechanism influences on system dynamics and control performance. The proposed approach includes an experimental implementation of two control strategies. First, a modern control based technique applied for system stabilization and position tracking. Then, simulation and experimental results illustrates the advantages of tilt-rotor configuration over fixed rotors. Second, a novel control strategy is presented. In this case, an MPC is employed as the lateral controller considering the tilt deflection as the command input. In this case, the control design accounts for input constrains related to the mechanism excursion limitations. Simulation and experimental results furnished the basis to discuss about the system behavior in terms of model uncertainties, actuation influence and control performance.

It is worth to mention that this study was developed as part of a research project on UAVs at the Autonomous Flight Laboratory (AFL) at UFU. The lack of experimental apparatus led to the development of a tilt-rotor bi-copter test bench for control tests and validation. More precisely, it aims to present the design, dynamic model, parameter identification and control implementation for the required apparatus in order to test the proposed control formulations. The prototype was designed and constructed from scratch aiming experiment systematization and the vehicle safety. It was manufactured using low cost devices integrating sensors, actuators and an embedded controller programmed for autonomous operations. Therefore, the research interest comes not only from the dynamic and control analysis but also from the real implementation and design challenges.

1.3 Contributions

As will be discussed through the text, modelling and control of tilt-rotor multi-copters is the research subject of many works. These propose a myriad of structural design, actuation mechanisms and control strategies for different applications. Henceforth, on regarding the state of art of tilt-rotor vehicles, the main contributions of this study concerns the following:

- **Development of a tilt-rotor test bench**. For this study, it is proposed the design and construction, modelling and identification of an experimental test-bench in order to further investigate the tilt-rotor multi-copter dynamics. The apparatus allow multi-copter position tracking control experiments systematization so that the mathematical model and control law can be validated.

- **Tilt mechanism analysis**. Through the dynamic model and control architecture, it is expected to show how the tilt mechanism can interfere the controllability of the system in terms of the actuator mechanism dynamics. In order to accomplish this, different actuation and control formulations will be compared.
- **Control strategy**. Developing a control strategy based on the system behavior analysis will be pursued. The main goal is to decouple rotational and translation motion of the multi-copter also enforcing input and state constraints.
- **Control Formulation**. Use Model Predictive Control (MPC) technique to enhance the system tracking performance and to allow actuator constraint handling. The controller robustness is tested under the influence of model uncertainties and design properties.

1.4 Overview

The present document is outlined as follows. Firstly, in Chapter 2 a literature review of the current UAV's state of art is presented highlighting the tilt-rotor applications. The mathematical modelling of a generic multi-copter is presented in Chapter 3. Chapter 4 introduces the tilt-rotor bi-copter test bench apparatus discussing about the setup hardware and software architecture. The test-bench dynamic model is described in Chapter 5 while the model parameters system identification is presented in Chapter 6. Then, two control design strategies are proposed. In Chapter 7, a trajectory tracking controller is designed using Modern Control techniques. Chapter 8 brings a formulation for tilt-rotor multi-copter dynamic decoupling with a application of an MPC for horizontal position tracking. Conclusions, discussions and general remarks about the study are detailed in Chapter 9.

CHAPTER II

Literature Review

In this chapter the literature review concerning multi-copter UAVs is carried out. Primarily, a short historical evolution of UAVs is presented. In the sequence, classifications, applications and the state of art of these vehicles are discussed. An overview of existing tilt-rotor aircraft designs is outlined illustrating possible actuation mechanism configurations and applications. The chapter is concluded with a brief summary of the author's works related with the present study.

2.1 Historical evolution

One can simply imagine that a UAV is a flying device without a pilot on-board. By taking this perspective, anything as simple as a lunched rock could be included in this general aircraft category. Nonetheless, if a proper definition of a UAV as "*a vehicle that can generate aerodynamic lift*" is applied, a kite would probably be a candidate. This association raises a inconclusive discussion about the origin and a proper definition of the term UAV. Related to that, a good overview about the historical evolution of the UAVs can be found in Fahlstrom & Gleason (2012).

By assuming a contemporary definition, one may consider that the first world reconnaissance flying UAV should be granted to Douglas Archibald. In this case, he was able attach cameras and weather measuring devices to the line of kite in 1883.

Despite that, it was during World War I that UAVs had proven their value and became recognized systems. By that time, the US army developed an unmanned biplane capable of plunging itself to the ground as a bomb. In particular, the air vehicle was guided to the target using preset controls. In parallel to the aircraft development, it is noteworthy that other instruments boosted unmanned flight. As examples one can mention the automatic gyroscope stabilizer and the radio controller. Both devices made target drones feasible during World War II as the US RPs and German Vs family.

Later on, it was during the Vietnam-War era that UAVs had success in reconnaissance missions and had the chance to be extensively employed in combat. The vehicles were air launched from other airplanes and used a parachute for recovery. Approximately 20 years later, the Kuwait/Iraq war allowed military planners an opportunity to use UAVs in combat conditions. Even though the performance of the available systems was less than satisfactory in many ways, those vehicles were considered a highly desirable asset. By that time, popular military aircraft started to emerge as the US Air Force Pioneer and British CL 89 helicopter.

At the onset of the 21st century, the war in Afghanistan and Iraq has transformed the status of UAVs. This technology has become a potential key weapon system. In that case, they were able to search for opponents and missions to their rightful place, performing many roles that are central for military operations. The American Global Hawk and Predator were examples of efficiency specially on nocturnal missions. This examples and others are part of what now has become a prominent technology. For more information about the UAVs military ascension, one may consult Fahlstrom & Gleason (2012).

As can be perceived, UAV systems have tended to be driven by military applications throughout their history, as many areas of technology. Advances in manufacturing, navigation, remote control capabilities, and power storage systems have made possible the development of a wide range of drones which are more economically feasible. Therefore, such vehicles can be employed in situations where the presence of humans is difficult, impossible, or dangerous drawing the attention of companies in different segments (BACHMANN et al., 2009).

Potentially profitable for civilian applications, UAVs are being employed for different purposes. As it was witnessed, the drone market opportunities increased significantly in the past few years. Its growth is explained by the emerging investments on UAVs, principally in construction, agriculture and insurance claims. Experts believes that the recent drone technology had already overcome manned aircraft in range, endurance, reliability and cost.

Based on a future perspective, Castellano (2019) highlights two main aspects regarding UAV operations. Firstly, there are high expectations about autonomous aerial vehicles guided by artificial intelligence based algorithms. This first assumption creates an hypothesis that these vehicles will be able to fly using predictive analysis making the pilots obsoletes. Secondly, the UAVs multi-system cooperation intelligence will be important to accomplish multi-tasks concomitantly enabling multi-aircraft modular operations.

It is in this dynamic environment that a massive variety of UAV designs have emerged. Nowadays, the drones spreads from a simple leisure device to a potential military weapon. This effect demanded the development of criterias to classify and better understand the technology. The up-to-date UAV classification, based on a literature review, is presented in the sequel.

2.2 UAV classification

UAV applications have widely spread throughout the years, bringing with them a variety of platforms with different configurations. As the number of models is considerably increasing, it is suitable to classify them by identifying their common characteristics. Generally, features including weight, wing span, wing loading, range, maximum altitude, speed, endurance, motor-propulsive set and production costs, are important design parameters that distinguish different types of UAVs.

There is a series of UAV classifications used by national regulation agencies as Federal Aviation Administration (FAA) in USA and Agência Nacional de Aviação Civil (ANAC) in Brazil which can be found in Fahlstrom & Gleason (2012) and ANAC (2021), respectively. In such cases, the classifications aid the agencies to create regulatory policies for operation, manufacturing and maintenance.

Moreover, an alternative classification can be found in Hassanalian & Abdelke (2017). In this case, it was proposed a broader classification by identifying advantages of each platform as relevant to the demands of users. The authors consider a wide spectrum of drones from UAV class with maximum wing span of 61 m and weight of $15{,}000[kg]$ to smart dust (SD) with minimum size of $1mm$ and weight of $0.005[g]$. Between UAV and SD there are various types of drones, such as micro unmanned air vehicle (μUAV), micro air vehicle (MAV), nano air vehicle (NAV), and pico air vehicle (PAV). A myriad of vehicle configurations can be included in each class as illustrated in Fig. 2.1. As indicated in the figure, UAVs can be considered as HTOL (horizontal take off landing), VTOL (vertical take-off landing), hybrid model (tilt-wing, tilt-rotor, tilt-body, and ducted fan), rotary wing, flapping wings and unconventional types. Following the scope of this work, some of these configurations are worthy to be discussed.

2.2.1 HTOL vs VTOL UAVs

HTOL configurations are the most common designs in general aviation. Since the body of these vehicles are aerodynamic surfaces, they can generate lift, providing high endurance and range margins. Airplanes are included in this group and their most notable characteristic is the dependence of airspeed to be airborne.

On the other hand, there are missions that taking-off in limited space is required. If that is the case, VTOL configurations are recommended. In this class one can include rotary wing aircraft as multi-copters and helicopters which uses the power-train to generate lift. For

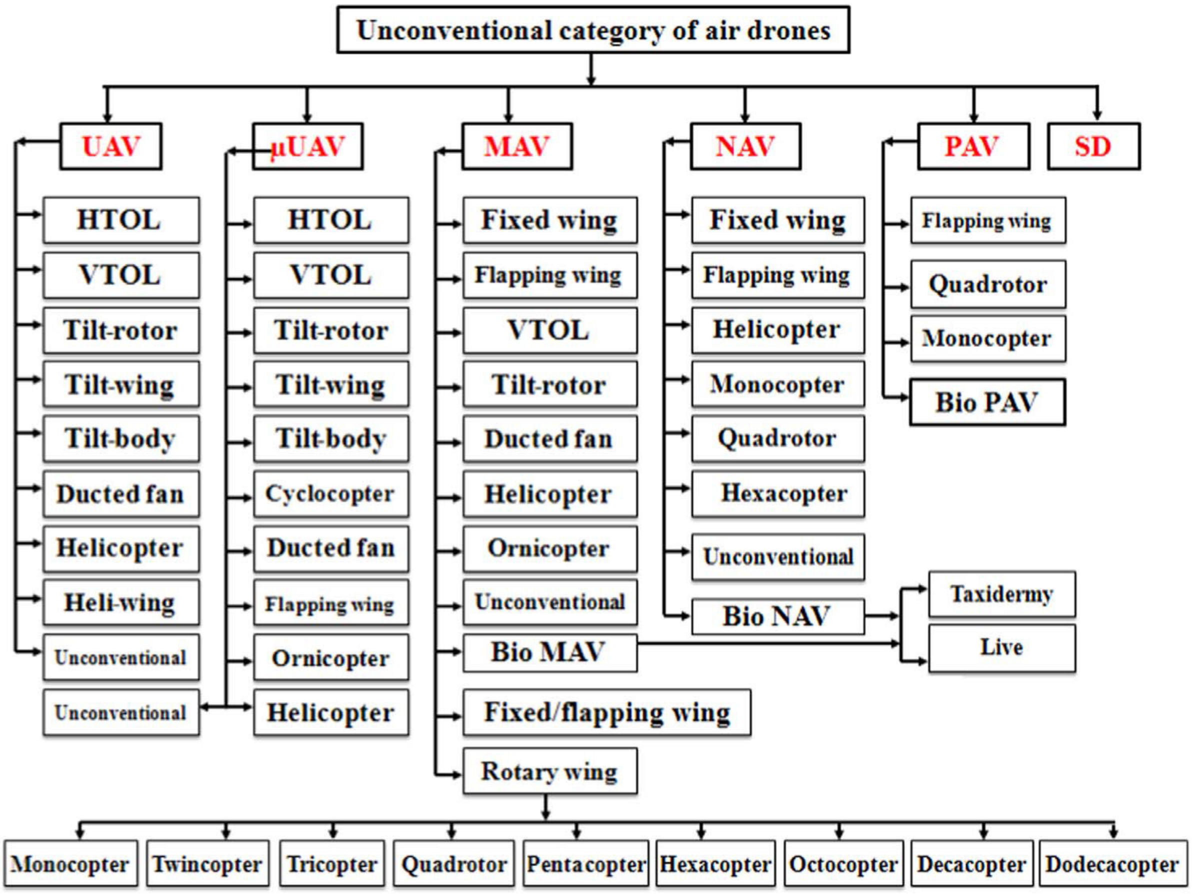

Figure 2.1: UAV classification. Source: (HASSANALIAN; ABDELKE, 2017)

hovering flight mode, VTOLs are more efficient than HTOLs dismissing a runway. Despite that, they have lower energy efficiency.

VTOLs usually have limitations in cruise speed for longer range missions. Aiming to mitigate this limitations, hybrid designs combining capabilities of both VTOL and HTOL were introduced. These aircraft are able to hover as a rotary wing and use fixed lift surfaces during cruise flight to enhance endurance. The key challenge for hybrid VTOLs is to perform a transition between vertical and horizontal flight which can be accomplished by using thrust vectoring mechanisms as tilt-rotor or tilt-wings. Both have been widely used in many aircraft designs. For instance, they are considered as a fundamental technology to make urban transportation feasible since the VTOL characteristic is demanded. Both Boeing PAV and the Lilium Jet, shown in Fig. 2.2, are good examples of this conceptual design.

Figure 2.2: VTOL concepts for urban transportation: Boeing PAV (left) and Lilium Jet (right). Source: sUAS News, 2019.

2.2.2 Multi-copter MAVs

Concerning VTOL and hover flight capabilities, rotary-wing aircraft are good candidates to be included in this category. It includes standard helicopters which can be subdivided in single, coaxial and/or tandem rotor. In particular, these vehicles use a spinning rotor to induce airspeed on a aerodynamic surface in order to generate the required lift to keep it airborne. Furthermore, the forces and moments are controlled by a mechanism that changes the incidence angle of the lift surface, i.e. the propeller pitch angle.

By contrast, multi-copters are often rotary-wing vehicles with fixed pitch propellers. In such configurations, the motor spinning speed variation is used to cause moments from differential thrust, enabling attitude and position control . As a consequence, multi-copters have advantages over other configurations due to mechanical simplicity, maneuverability and payload capacity. These characteristics, which are typical for MAVs, favor miniaturization, making multi-copters ideal vehicles to operate in restricted space environments (BOUABDALLAH, 2007).

Multi-copters can be sub-classified by their number of rotors. The most common configurations are: bi-copters, tri-copters, quad-copters and hexa-copters. One may note that adding more propulsive sets increases the payload capacity. On the other hand, it reduces energy efficiency and demands more from system integration design.

2.2.3 Tilt rotor UAVs

To combine the advantages of both HTOL and VTOL vehicles, many researches have been carried out on hybrid aircraft with high-speed cruise and VTOL capability. This led to the concept of tilt rotor aerial vehicle (TRUAV) which relies on wings and rotors for generating lift (LIU et al., 2017). The Boeing PAV and Lilium jet shown in Fig. 2.2 are examples of TRUAVs. Among different types of these drones, tilt-rotors have attracted many designers because of their energy efficiency, stability, and controllability in several missions. Despite that, the tilt-rotor mechanism may increase the systems mechanical complexity and affect system dynamic behavior. Usually, for hybrid TRUAVs, the degradation of stability is found at high-speed high-angle of attack in forward flight mode and the involved equations of motion are highly coupled and nonlinear (MORRIS, 1997).

Tilt-rotor actuation augmentation can be also used in multi-copter configurations. As aforementioned, for standard fixed rotor, attitude and position control relies on the propeller angular speed of each motor set. As long as there are less inputs than states, these dynamics cannot be controlled independently and, consequently, the system is said to be underactuated (BADR et al., 2016).

A possible solution for the underactuation issue is the control input augmentation that yields full actuation. Addressing to this, a myriad of actuation mechanisms were figured out as presented in Table 2.1. For illustration, in Cutler et al. (2011) the multi-copter's propeller blades are able to change the pitch angle, similarly to conventional helicopters. Another actuation strategy is the tilt-rotor mechanism. It consists on the rotor rotation w.r.t. the multi-rotor's arms so that the thrust force vector can be oriented in a desired direction. The motor tilt capability was explored in several multi-copter MAVs. For instance, Ryll et al. (2012) proposed a quad-copter design whose four propulsive sets can rotate laterally w.r.t. the arm longitudinal axis. The addition of the new control made full controllability to all states feasible, providing actuation redundancy and also optimizing energy-efficiency.

Analogously, longitudinal tilt mechanisms were also employed as in Nemati & Kumar (2014) and Badr et al. (2016). In such cases the motor set is capable of tilting in a direction perpendicular to the multi-copter's arm. Comparing the two actuation features, one can highlight that lateral tilt mechanisms have higher controllability over yaw orientation. Moreover, tilt mechanisms, either lateral or longitudinal, can be also used on bi-copters (KENDOUL et al., 2005), tri-copters (SERVAIS et al., 2015), quad-copters (OOSEDO et al., 2016), hexa-copters (RYLL et al., 2016) and VTOL fixed-wing aircraft (ONEN et al., 2015) either to improve stability or to perform autonomous flight.

Another perspective is the vehicle's actuation properties in the case of system failure. As an example, in the case of rotor-loss the propellers mutual orientations affect the multi-copter control properties. Related to that, Du et al. (2015) proposes a controllability analysis based on the system approximation around hovering. It has been shown that in the case of a rotor failure the *controlability* strongly depends on the propeller spinning direction. Similarly, the concept of *maneuverability* has been introduced and investigated by Wen et al. (2021). In the fault-motor case, the vertical maneuverability reduces due to the loss of control authority, and the hoovering condition is still possible only for some tilt of the propellers.

By looking at the studied variations, some important remarks must be taken regarding tilt-rotor multi-copters as:

- They can reduce energy consumption once the system control does not rely entirely on thrust force variation,
- Attitude and position control decoupling, i.e. non-horizontal equilibrium condition and/or shift its position without changing its attitude,
- Can present better maneuverability,
- Increase system controllability,

- Can provide more input degrees of freedom to the control system which can be substantial for handling system constraints,
- Controller is able to reject external disturbances even with a failed motor.

Table 2.1: Tilt rotor multi-copters state of art

Author	Rotor Number	Specification	Validation	Contribution
(KENDOUL et al., 2005)	2	Lateral and longitudinal tilt	Simulation	Design of a bi-copter with tilt capability. Stabilization and trajectory tracking using backstepping control
(RYLL et al., 2012)	4	Lateral tilt	Simulation	A control law is proposed for trajectory tracking
(BARSK, 2012)	3	Lateral tilt	Experimental	Modelling and system identification of the real model. Used a model predictive controller for system stabilization subjected to physical limitations
(GASCO, 2012)	4	Longitudinal and lateral tilt	Experimental	Design and construction of a dual axis tilt quadrotor. Attitude control system design using PD controller
(NEMATI; KUMAR, 2014)	4	Lateral tilt	Simulation	Design of a position and attitude controller using PD technique
(SERVAIS et al., 2015)	3	Lateral tilt	Simulation	Design of a bi-copter with tilt capability. Stabilization and trajectory tracking using backstepping control
(BADR et al., 2016)	4	Longitudinal tilt	Simulation	Trajectory tracking of 5th order polynomials using PID control
(ŞENKUL; ALTUG, 2016)	4	Lateral tilt	Simulation	Evaluate system robustness and stability using a cascaded PID controller for regular and tilt quad-copters
(PAPACHRISTOS; ALEXIS, 2016)	3	Lateral tilt	Experimental	Modelling of a tri-copter with tilt capabilities. Optimal control using Model Predictive Control technique for autonomous operation subjected to actuation restrictions
(RYLL et al., 2016)	6	Longitudinal tilt	Experimental	Novel UAV concept wich is able to smoothly change its configuration using only one additional motor that tilt all propellers simultaneously
(MARQUES, 2018)	4	Longitudinal and lateral tilt	Simulation	Development of a generic model for multi-copter endowed with tilt mechanism. Trajectory tracking using modern control technique.
(SRIDHAR et al., 2019)	4	Lateral tilt	Simulation	Attitude and position control using a sliding mode controller under wind disturbances. Model aerodynamic forces were obtained via CFD simulations.

2.3 Control techniques

During the development of a multi-copter MAV project, one of the main steps concerns the design of a closed-loop controller as these vehicles usually have an open-loop unstable dynamics. Generally, UAVs control task consists on system stabilization and autonomous operation considering a trajectory path following capability. As a consequence, the control design challenges for MAVs have attracted the attention of researchers on recent years. Additionally, they can be considered as an ideal robotic platform for the development and testing of control strategies (SUIÇMEZ, 2014).

In fact, multi-copter control has been widely investigated in the literature. As an example, Bouabdallah et al. (2004) compares PID and LQ control techniques applied for a quad-copter stabilization. In Lee et al. (2009), feedback linearization and sliding mode control techniques are used in a quad-copter for autonomous operations limiting its control effort under the presence of uncertainties and noisy conditions. Likewise, Alexis et al. (2011) proposes a Model Predictive Controller for a quad-copter stabilization subjected to gust disturbances taking into account the system physical constraints. Moreover, Smeur et al. (2018) uses a cascaded incremental nonlinear dynamic inversion for attitude and position control of a MAV highlighting its improvements over conventional PID control.The scientific contribution fot multi-copter control can be corroborated by Table 2.1. On studying the proposed control techniques, one can conclude that not only the choice of the control formulation is important but also its architecture and actuation strategy.

Taking Marques (2018) as an example, a linear state-space model is used for control design. In such case, the input vector was chosen as the motor angular velocity and the tilt angles. Consequently, by mapping the poles and zeros for the longitudinal, lateral and no tilt scenarios, the author has shown that the system presents non-minimum phase zeros. Henceforth, the system could not be steered to stability for a unbounded reference signals as ramp position signals.

Notwithstanding, other authors as Ryll et al. (2012) and Nemati & Kumar (2014) have considered that the model input vector is represented by the resulting forces and moments. Then, the tilt angles are estimated from the kinematic relations while the motor angular velocities were calculated from the system equilibrium equations. In this case, the controller must have information of the desired resultant thrust force direction. Likewise, Badr et al. (2016) investigates two distinct applications for a multi-copter: non-horizontal hover flight and horizontal plane shifting without using the propeller variation. The above mentioned examples illustrates how the control actuation strategy can be profitable for the system performance and versatility.

Under those circumstances, it is suitable to associate the tilt actuation with MPC formulation bearing in mind its mechanical limitations and inputs augmentation. For instance, in Papachristos & Alexis (2016) an explicit MPC is used for controlling a tri-copter containing lateral tilt mechanisms. For this application, the control exploits the combined capabilities of direct longitudinal tilt-actuation and underactuated body-pitching. Besides state and input restrictions, a terminal constraint is also added in the MPC formulation to guarantee system stability. Experimental results validated the proposed scheme evidencing the increased performance results.

In addition to the classical control formulations employed on multi-copters, more sophisticated control techniques have been investigated. As examples Sumantri et al. (2016) and Lee et al. (2009) used sliding mode control for quad-copter attitude and translational control. The technique is picked up based on robust system performance under the influence of uncertainties and external disturbances.

More recently, Artificial Intelligence (AI) based control techniques are being explored as presented in Koch et al. (2019), Hwangbo et al. (2017) and Pi et al. (2020). In such cases, the system is heuristically trained applying Reinforcement Learning technique. The implementation has shown good system performance specially for high attitude maneuvers. It must be pointed out that, for classical control implementations, these maneuvers are beyond the linear regime of the system which makes the control design a hard task. From a practical perspective, AI based controllers may gain prominence in the next years.

2.4 Author's Related Works

As aforementioned, the present work is the part of the development of a research project from the Autonomous Flight Laboratory (AFL) at UFU. The team's main goal is to study flight dynamics and control of UAVs. More specifically, the research focus on:

- aerodynamic modelling of fixed wing UAVs,
- identification of multi-copter parameters,
- development of embedded systems for multi-copters,
- flight simulators and Hardware-In-the-Loop (HIL) simulations,
- Artificial Neural Fuzzy Inference System (ANFIS) applications for control and system identification and
- tilt-rotor multi-copters modelling and control.

As a result of the group effort put on the above mentioned research topics, some related contributions can be highlighted. For instance, the early studies in multi-copter dynamics and control can be found in Marques et al. (2017) and Tarifa et al. (2017). In the first case, the authors studied the implementation of a LQT control strategy on a hexa-copter for trajectory tracking purposes. Similarly, the second explored a non-linear control law strategy on a tilted tri-copter UAV. The system modelling included the tilt kinematics which enabled the tri-copter controllability facing the underactuated system characteristic.

Later, aiming to develop an experimental tilt-rotor multi-copter, the structural project of a quadcopter was conceived. The embedded system containing the control law an sensor communication was developed as presented in Jeronimo (2019). Concomitantly, the kinematic relations of the tilt-rotor mechanism were further investigated in Marques (2018). The two studies led to the HIL implementation. As discussed in Marques et al. (2018), this approach was helpful to test embedded system communication, the control law and the actuator performance. These were the early steps for the tilt-rotor bi-copter test bench development.

Cooperatively with the hardware and embedded system development, control and dynamic analysis regarding tilt-rotor multi-copters were carried out aiming to further understand how it affects the system dynamics. For instance, a stability perspective of the effect of endowing tilt-rotor mechanism in multi-copters was studied in Marques (2019) focusing on pole and zero distribution of different types of tilting deflection. In this case, the control performance of fixed, lateral and longitudinal tilt rotors was evaluated. Likewise, in Marques et al. (2019), an LQT control formulation was employed for position and attitude tracking control of a lateral-tilted quad-copter UAV.

In order to further investigate the problem, an MPC control formulation for position control of a tilt-rotor quad-copter was proposed in Marques et al. (2020). In particular, the study employed a dual mode controller, composed by an LQR and an MPC. The first is used for attitude regulation while the second is responsible for position tracking. As a result, the strategy has shown to be a good approach for tilt-rotor control, specially if the mechanisms deflections limitations are considered as input constraints.

In summary, the above mentioned contributions describe the project evolution through the AFL history. They compose the fundamental resources for understanding and developing a tilt-rotor multi-copter for autonomous operations as will be discussed in this study.

2.5 Chapter Summary

- The historical evolution of the UAVs has shown that its technology has been expanding in the recent years boosting scientific researches related to the topic.

- There is an increasing demand for more agile, robust, versatile and low cost drones.
- Multi-copters are just one of a myriad of UAV classifications which has rotary wing configuration.
- The main benefits of multi-copters are their controllability, maneuverability, and payload capacity.
- Tilt-rotor configurations can benefit the vehicle energy efficiency, stability and versatility.
- Standard multi-copters, with parallel fixed rotors, can be classified as underactuaded systems since their spatial displacement relies on the combination of the motor thrust force.
- Multi-copters with tilt rotor capabilities has the number of control inputs increased which can be helpful to deal with underactuation.
- Related works found in the literature point out the benefits of endowing tilt-rotor mechanisms in multi-copters in terms of attitude and position control decoupling and control efficiency.
- Many control strategies can be found in the recent literature about trajectory tracking of multi-copters, and the MPC has shown to be worthy considering its constraint handling capabilities.

CHAPTER III

Tilt-rotor Dynamics

In this early chapter, the required kinematic relations of the tilt-rotors with the moving vehicle are presented. For such approach, it is considered that the mechanism is attached to a multi-copter's structure. The goal is to establish a relation between the rigid body dynamics and the thrust direction from each motor propulsive set. In advance of the mathematical model development, some considerations must be taken. Firstly, each rotor is capable of tilting either laterally and/or longitudinally with respect to the rotor's arm. Secondly, the tilt mechanism is attached to a multi-copter whose structure and propellers are rigid. All rotors, propeller blades and tilting mechanisms are the same. Lastly, the vehicle and its components mass/inertia properties and gravitational force are constant.

3.1 Kinematic Relations

To derive the kinematic relation between the multi-copter and the tilt-rotor, two different reference frames are adopted as illustrated in Fig. 3.1. Firstly, a body fixed coordinate frame, represented by $BCS : \{O_B; x_B; y_B; z_B\}$, fixed at the vehicle's center of gravity (CG) and capable of translating and rotating with it. Second, a motor reference frame $MCS : \{O_{M_i}; x_{M_i}, y_{M_i}, z_{M_i}\}$,

$i = 1, 2, \ldots, n$ which is also a non-inertial coordinate frame attached to each of the i^{th} propulsive set, with x_{M_i} and y_{M_i} representing the lateral and longitudinal tilting actuation axes, respectively. The z_{M_i} axis is normal to the propeller disc spinning plane and is coincident with the produced thrust force direction. Each vectoring rotor is located at the extremities of the UAV's arms at point O_{Mi} by an angle $\gamma_i = \pi(2i-1)/n$, $i = 1, 2, \ldots, n$ w.r.t the x_B axis direction of the *BCS*.

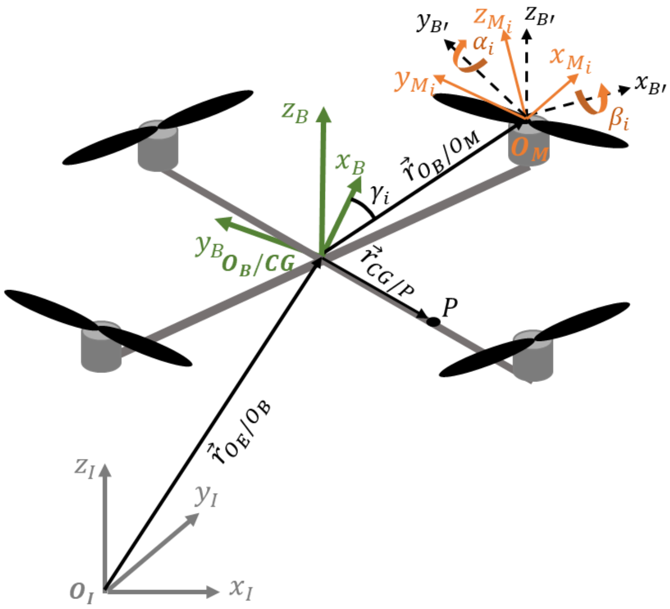

Figure 3.1: Coordinates frames representation: *ICS*, *BCS* and *MCS*

Then, the rotation matrix to project a vector on *MCS*, corresponding to the i^{th} propulsive set, on the *BCS*, is

$$\mathbf{R}_M^B = \mathbf{R}_M^B(\gamma_i)\mathbf{R}_M^B(\alpha_i)\mathbf{R}_M^B(\beta_i) \tag{3.1}$$

with

$$\mathbf{R}_M^B(\gamma_i) = \begin{bmatrix} \cos\gamma_i & -\sin\gamma_i & 0 \\ \sin\gamma_i & \cos\gamma_i & 0 \\ 0 & 0 & 1 \end{bmatrix}, \tag{3.2}$$

$$\mathbf{R}_M^B(\alpha_i) = \begin{bmatrix} \cos\alpha_i & 0 & \sin\alpha_i \\ 0 & 1 & 0 \\ -\sin\alpha_i & 0 & \cos\alpha_i \end{bmatrix} \text{ and} \tag{3.3}$$

$$\mathbf{R}_M^B(\beta_i) = \begin{bmatrix} 1 & 0 & 0 \\ 0 & \cos\beta_i & -\sin\beta_i \\ 0 & \sin\beta_i & \cos\beta_i \end{bmatrix} \tag{3.4}$$

being α_i and β_i the longitudinal and the lateral tilt angles about y_{M_i} and x_{M_i}, respectively.

Additionally, assuming $\mathbf{R}_M^B$ orthogonality, the inverse transformation of (3.1) can be performed by using the transpose matrices $(\mathbf{R}_M^B)^T$.

3.2 Forces and Moments

For multi-copter UAVs, the required thrust force to maintain the vehicle in flight is generated by its propulsive set. Herein, it is assumed that each of them is equipped with a DC brushless electric motor driving a propeller. During nominal operation, the spinning propellers produces a resultant thrust acting on the z_{Mi} direction given by:

$$f_i = k_p \Omega_i^2 \tag{3.5}$$

where k_p is a propulsive set constant relating the electric torque, current, motor voltage, blade disc radius and surrounding air properties (HUANG et al., 2009). Additionally, Ω_i is the angular speed of the motor shaft.

For control applications, the model presented in (3.5) can be representative, especially if the linear stated space model is considered. As in Conroy et al. (2014), the motor relation with propeller angular speed can be obtained from a static test. Moreover, for the sake of simplicity, the desired thrust force can be used as the control command variable. If the aerodynamic effect in the rotor performance has to be accounted, approaches presented in Huang et al. (2009) or Yang et al. (2020) can be used. Also, the frame aerodynamics depends on higher fidelity models/experiments as presented in Yoon et al. (2017). In such circumstances, the models approximate aerodynamic effects which significantly influence the vehicle dynamics when it is under the presence of high airspeed profiles. Since those effects are beyond the scope of this work, they can be neglected.

Since the resultant thrust force acts on the z_{M_i} direction, f_i can be written in the MCS as

$$\mathbf{F}_{T_{Mi}} = \begin{bmatrix} 0 & 0 & f_i \end{bmatrix}^T \tag{3.6}$$

Henceforth, by using the coordinate transformation $\mathbf{R}_M^B$, the net thrust force for n propulsive sets is

$$\mathbf{F}_{T_{BCS}} = \begin{bmatrix} \sum_{i=1}^{n} \left(s(\gamma_i)s(\beta_i) + c(\gamma_i)s(\alpha_i)c(\beta_i)\right)k_p\Omega_i^2 \\ \sum_{i=1}^{n} \left(-c(\gamma_i)s(\beta_i) + s(\gamma_i)s(\alpha_i)c(\beta_i)\right)k_p\Omega_i^2 \\ \sum_{i=1}^{n} c(\alpha_i)c(\beta_i)k_p\Omega_i^2 \end{bmatrix} \tag{3.7}$$

where k_p is a propulsive set constant relating the electric torque, current, motor voltage, blade disc radius and surrounding air properties and Ω_i is the angular speed of each of the n motor shafts. Moreover, it is considered that $\cos(x) = c(x)$ and $\sin(x) = s(x)$ for now on.

Addressing to the external toques acting on the vehicle, they are mainly caused by the distribution of f_i w.r.t the CG. Hence, the torque produced by the spinning propellers can be expressed as:

$$\mathbf{M}_{T_B} = \sum_{i=1}^{n} \mathbf{d}_i \times \mathbf{F}_{T_{B_i}} \tag{3.8}$$

where $\mathbf{d}_i = [L_i \cos\gamma_i \; L_i \sin\gamma_i \; z_{CGi}]^T$ is the distance from the motor position O_{Mi} to CG being L_i the multi-copter arm length. Therefore,

$$\mathbf{M}_{T_B} = \begin{bmatrix} \sum_{i=1}^{n} \left(L_i s(\gamma_i)c(\alpha_i)c(\beta_i) - z_{CGi}\left(s(\gamma_i)s(\alpha_i)c(\beta_i) - c(\gamma_i)s(\beta_i)\right)\right)k_p\Omega_i^2 \\ \sum_{i=1}^{n} \left(-L_i c(\gamma_i)c(\alpha_i)c(\beta_i) + z_{CGi}\left(c(\gamma_i)s(\alpha_i)c(\beta_i) - s(\gamma_i)s(\beta_i)\right)\right)k_p\Omega_i^2 \\ \sum_{i=1}^{n} \left(L_i c(\gamma_i)(s(\gamma_i)s(\alpha_i)c(\beta_i) - c(\gamma_i)s(\beta_i)) - L_i s(\gamma_i)(c(\gamma_i)s(\alpha_i)c(\beta_i) - s(\gamma_i)s(\beta_i))\right)k_p\Omega_i^2 \end{bmatrix} \tag{3.9}$$

Assuming that the MAVs mass are generally small, the gyroscopic effect of the spinning propellers must be accounted. This torque is an outcome of the in-flight propeller's angular momentum direction variation. As long as the propulsive set is attached to a tilt mechanism, the angular momentum direction change is caused by two main phenomenons. First, the mechanism movement, expressed as the rate of change of the tilt angles ($\dot{\beta}_i$, and $\dot{\alpha}_i$). Second, the vehicle angular velocity $\boldsymbol{\omega}$. Therefore, the propeller disc angular speed $\boldsymbol{\omega}_{p_{B_i}}$, in the *BCS*, can be written as

$$\boldsymbol{\omega}_{p_{B_i}} = \mathbf{R}(\gamma_i)\left[\mathbf{R}(\alpha_i)\begin{bmatrix} 0 \\ \dot{\alpha}_i \\ 0 \end{bmatrix}\mathbf{R}(\alpha_i)\mathbf{R}(\beta_i)\begin{bmatrix} \dot{\beta}_i \\ 0 \\ 0 \end{bmatrix}\right] + \boldsymbol{\omega} \tag{3.10}$$

being $\boldsymbol{\omega}$ the vehicle angular velocity with respect to the BCS. Considering that the propeller blades are spinning around the z_{M_i} direction of the *MCS*, one can state that the angular momentum for each propeller can be written as follows:

$$\mathbf{H}_{M_{G_i}} = \begin{bmatrix} 0 & 0 & I_{M_i}\Omega_i \end{bmatrix}^T \tag{3.11}$$

where I_{M_i} is the propeller moment of inertia and assumed as constant.

From (3.10) and (3.11), using the matrix rotation $\mathbf{R}_M^B$ to write $\mathbf{H}_{M_{g_i}}$ on *BCS*, the resultant torque due the propeller gyroscopic effect $\mathbf{M}_{G_B}$ can be calculated by

$$\mathbf{M}_{G_B} = \sum_{i=1}^{n} \boldsymbol{\omega}_{p_{B_i}} \times \begin{bmatrix} \sum_{i=1}^{n} \left(s(\gamma_i)s(\beta_i) + c(\gamma_i)s(\alpha_i)c(\beta_i)\right)I_{M_i}\Omega_i \\ \sum_{i=1}^{n} \left(-c(\gamma_i)s(\beta_i) + s(\gamma_i)s(\alpha_i)c(\beta_i)\right)I_{M_i}\Omega_i \\ \sum_{i=1}^{n} c(\alpha_i)c(\beta_i)I_{M_i}\Omega_i \end{bmatrix} \tag{3.12}$$

It is worth mentioning that, in this case, the propeller angular speed variation are small and can be neglected.

The last accounted torque is due to the air aerodynamic drag on the propeller blades cross section. Its component acts on the rotor spinning axis z_{M_i} and it can be modeled as

$$\mathbf{M}_{F_{M_i}} = \begin{bmatrix} 0 & 0 & -b\Omega_i^2\mathbf{sign}(\Omega_i) \end{bmatrix}^T \tag{3.13}$$

being b the propeller drag constant. The function $\mathbf{sign}(x)$ extracts the sign of the propeller angular speed direction where $\Omega_i > 0$ or $\Omega_i < 0$ for clockwise and counter-clockwise propeller spinning direction, respectively. Thus, projecting $\mathbf{M}_{F_{M_i}}$ on the BCS, it follows that

$$\mathbf{M}_{F_B} = \sum_{i=1}^{n} \mathbf{R}_M^B \mathbf{M}_{F_{M_i}} \tag{3.14}$$

Then, adding (3.8), (3.12) and (3.14), the resultant torque is

$$\mathbf{M}_B = \mathbf{M}_{T_B} + \mathbf{M}_{G_B} + \mathbf{M}_{F_B} \tag{3.15}$$

3.3 Chapter Summary

- The tilt-rotor mechanism can be used to change the motor thrust force direction along flight increasing the control degrees of freedom of the system.
- The thrust force components, expressed in the BCS, are function of kinematic relations presented in Eq. (3.1).
- For the proposed formulation, the motor is able to rotate longitudinally (α) and laterally (β).
- Including the tilt deflections as degrees of freedom includes non-linear terms in the thrust forces and moments components in x_B, y_B and z_B as shown in Eqs. (3.7), (3.9), (3.12) and (3.14) .

- It can be seen in Eq. (3.12) that the rate of change of the spinning propeller direction induces a gyroscopic effect in the vehicle CG.
- The propeller drag torque (3.14), used for yaw control in fixed rotor multi-copters, has components in x_B, y_B and z_B in tilt-rotor configurations.

CHAPTER IV

Apparatus and Procedures

In this study, it is proposed that the control application will be evaluated through two methods: numerical simulations and experimental testing. Thus, for the first case, the equations of motion and control law can be solved using Matlab / Simulink® interface in order to obtain preliminary results. This tool is valuable to illustrate the dynamical behavior of closed loop system and tune the embedded controller. Meanwhile, for the experimental tests, the development of a proper apparatus is required. In this case a 3 DOF tilt-rotor bi-copter test bench is proposed. The prototype gives support for the control law evaluation and also investigate real implementation challenges. The test-bench design, its components and software architecture will be presented in this section.

4.1 Test-bench setup

One may consider that, for the development of a control system used in flying robots, an adequate test-bench should be developed for preliminary experiments. In this manner, some degrees of freedom can be locked in order to reduce control complexity and avoid system damage. Several research projects developed their own experimental setup to validate control laws and make experimental analysis.

For instance, the OS4 test-bench developed by Bouabdallah (2007) was employed to test attitude regulation of a quadcopter. In such case, the multi-copter movement is restricted to only three degrees of freedom about the vehicle CG, represented by the yaw, pitch and roll rotations. Moreover, the vehicle is equipped with 4 motor propulsive sets, an IMU and the rigid structure where the quadcopter can be attached. Similarly, in Cutler et al. (2011), the quadcopter is attached to a test fixture that restricts the motion to a single axis. Then, the vehicle is commanded to follow a series of roll and roll rate commands in order to test the designed PD controller.

In some research projects, many authors choose to use commercial test-benches to validate their studies. Examples are the apparatus developed by Quanser® which can be useful to validate control studies (QUANSER, 2020). The company offers 2 different models: a 3 DOF helicopter equipped with 2 rotors, named the Quanser® AERO, which is a fully integrated dual-motor capable of 3 rotations that represents the vehicle 1 axis attitude, altitude and lateral motion. Secondly is the Quanser® 3 DOF Hover equipped with 4 rotors and a pivot joint that enables the body to rotate about the roll, pitch and yaw axes. Examples of control studies validated in commercial test-benches experiments as presented can be found in Pandey et al. (2017), Hernandez-Gonzalez et al. (2012) and Jafri et al. (2017). For this particular study, the design and construction of a prototype to test tilt-rotor control applications mitigates the lack of apparatus at AFL. In addition, it is worth to mention that there is no commercially available device which includes the tilt-rotor capabilities to the attached actuators.

To accomplish the study objectives, the proposed structure is composed of a tilt-rotor bi-copter supported by an articulated arm as illustrated in Fig. 4.1. The support base (1), the articulated arm (2) and the element (4) are mounted using rotary bearing joints. These elements are able to rotate about z_1, z_2 and z_4. Further, a tilt-rotor bi-copter is fixed at point P_4 which allows the rotation about a single axis z_4 denoted by the angle θ_4. This DOF represents a rotation about its own axis characterizing the vehicle's attitude. Moreover, the rotations of elements (1) and (2) permit the vehicle to operate in a semi-sphere, defined by the angles θ_1 and θ_2, with respect to an inertial coordinate frame positioned at P_1, corresponding to the lateral and vertical displacement.

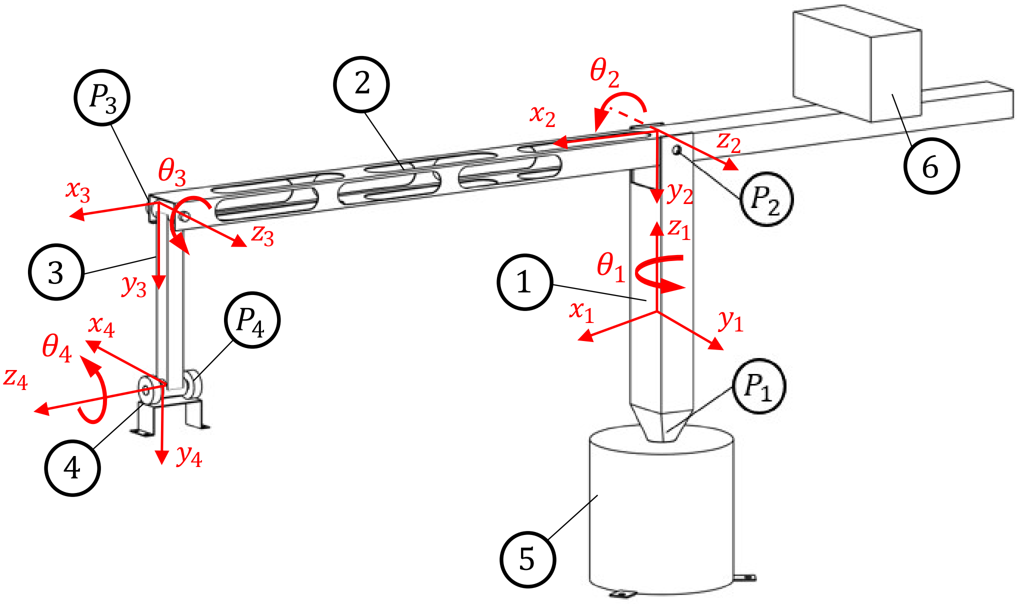

Figure 4.1: Test-bench 3D CAD model.

It must be noted that the assumption of a single attitude movement takes into account that the majority of multi-copters configurations are symmetrical in $x-z$ and $y-z$ plane. Also, the yaw movement is generally controlled by the operator or by an dedicated guidance control law. Therefore, the proposed apparatus tries approximates the behavior of a free multi-copter reducing the risks of possible damages due to operational failures.

The mechanism was modeled with the aid of a CAD software. Figure 4.2 shows a side view with the dimensions of elements 1 to 5. Its structure is made of steel and its dimensions, mass and inertia properties of each element are presented in Table 4.1. The last were estimated from the virtual model but also experimentally as will be discussed in the next sections. It must be emphasized that the structure base (6) cannot rotate and must be fixed on a surface to guarantee system's stability. Moreover, a counter-weight (5) is attached to element (2) so that the arm structure weight is in balance w.r.t point P_2, i.e. components (2), (3), (4) and (6) CG is coincident with the rotation axis z_2.

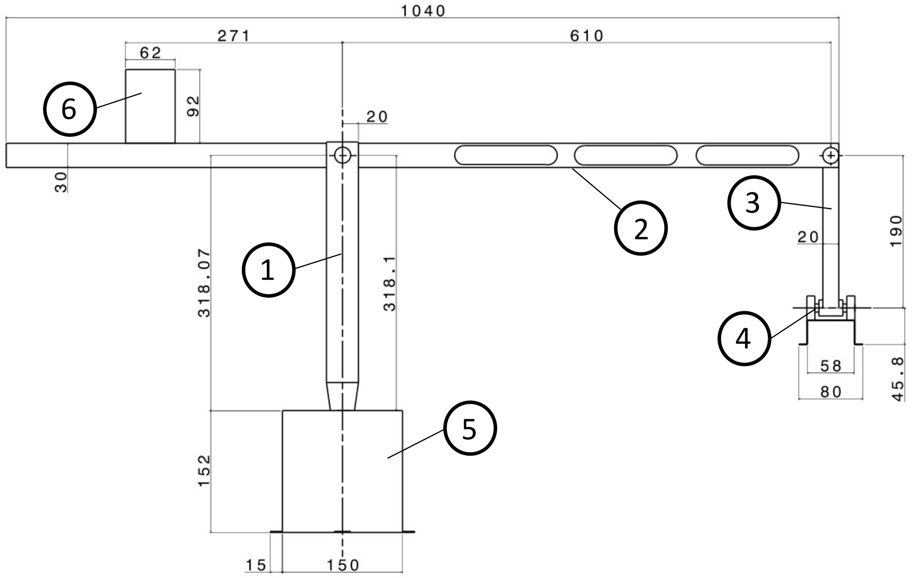

Figure 4.2: Test-bench side view with dimensions.

Table 4.1: Test-bench mass and inertia properties.

Component	Mass [kg]	Inertia* [kg.m^2]		
		I_{xx}	I_{yy}	I_{zz}
1	0.3662	0.003	0.003	1.1250e-07
2	0.7413	1.1250e-07	0.0226	0.0226
3	0.115	3.145e-07	1.4341e-04	1.4341e-04
4**	0.090	0	0	0
5	0.834	0.0016	0.0016	0.0186
6**	1.7	0	0	0
Total	3.8465	0.156	0.641	0.509

* All inertia properties are taken w.r.t. the component CG

** Element is considered as point mass and inertia properties are neglected

4.2 The tilt-rotor bi-copter

The designed tilt-rotor bi-copter (TRBC) is illustrated in Fig. 4.3. It consists of two arms fixed to a center body. All the elements of the TRBC were manufactured with the aid of a CNC 3D printing router. The selected material was the ABS (Acrylonitrile Butadiene Styrene) due to its density, low cost and 3D printing capability. The vehicle weight, with all components installed, is approximately 0.559 [kg].

Each arm contains a tilt rotor mechanism which acts as a push-pull servo and enables the installed motor to tilt along the arm direction. The tilt mechanism is a four-bar linkage, driven by a Hightech HS-65MG DC servo, as shown in Fig. 4.4. As illustrated in the figure, it permits the motor bed to rotate about its center axis from 0 to 35 degrees. In order to measure the tilt angle, a potentiometer is connected to the bed axis. The sensor is primarily used to estimate the mechanism dynamics and establish a servo PWM to angle relation experimentally as will be later discussed.

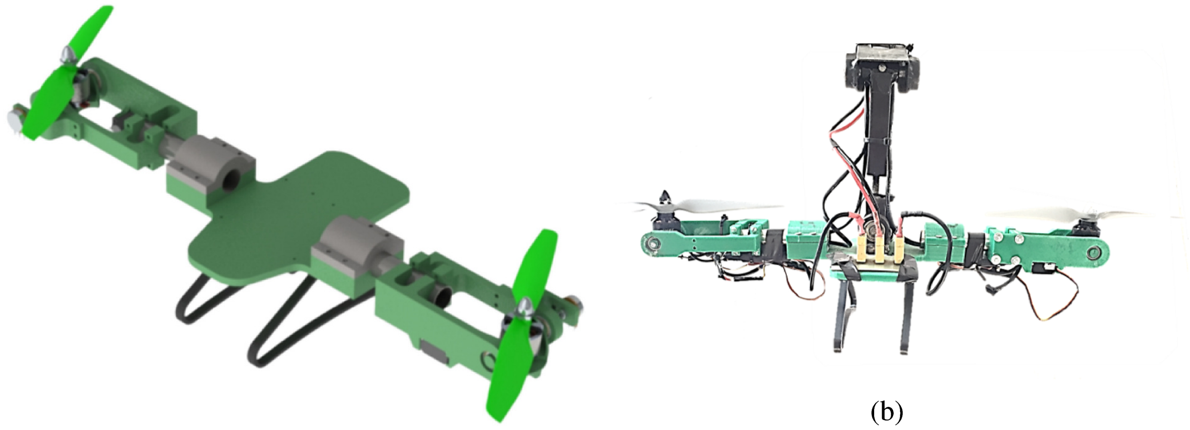
(a)

(b)

Figure 4.3: Tilt-rotor bi-copter CAD model. (a) CAD Model. (b) Final assembly.

Moreover, the TRBC propulsion system is composed of 2 EMAX® MT2216/810 KV brushless DC motors equipped with E300 ESC system and APC® 1045 composite propellers. Additionally, motors 1 and 2 have counter-rotating propellers. Their thrust coefficients and

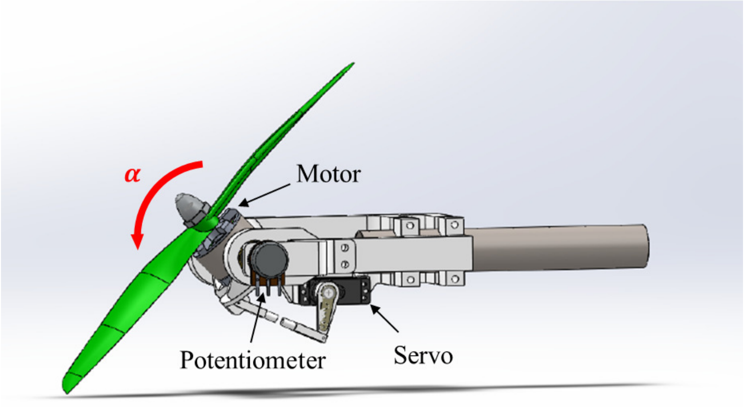

Figure 4.4: Tilt mechanism CAD model.

transfer functions (Pulse Width Modulation (PWM) signal to gross thrust force) were obtained experimentally from static tests. Table 4.2 summarizes the EMAX MT2216 data sheet mechanical and operational properties.

Table 4.2: Emax® MT2216 properties.

Property	Parameter	Value	Unit [SI]
Max Current	i_m	9.8	A
Voltage	V_m	11.1	V
Max thrust @ Max Current	T_{max}	670	g/axis
Max RPM @ Max Current	Ω_{max}	6620	RPM
Propeller Diameter	D_p	0.25	m

4.3 Data Processing

The experimental procedures in this study require an embedded controller to manage all the experiment process, control the actuators and read sensor data. A schematic architecture of the test-bench data processing system is shown in Fig. 4.5. All the data acquisition, processing, control implementation and hardware communication is under responsibility of a micro-controller. For this project, the BeagleBone® Green board (Fig. 4.6) micro-computer was selected as an off shelf option. The device is equipped with a Texas Instruments Sitara AM3358 processor with maximum speed of 1 GHz and a 512 MB DDR3 RAM. The board also contains 7 analog I/O pins, 65 digital I/O and 8 PWM I/O. The BeagleBone® Green main advantages over other micro-controllers (Arduino, Raspberry Pi, etc.) are: the processing capability, the number of PWM outputs, the board is pre-loaded with a Linux operating system, the capability to interact with external sensors and an Ethernet connection boosting up the communication between the micro-controller and a PC device (KUMAR, 2018). For this reason, one may consider that the BeagleBone® board is a good choice for projects that want both the functionality of Linux (such as networking and USB) and real-time connection with the embedded system.

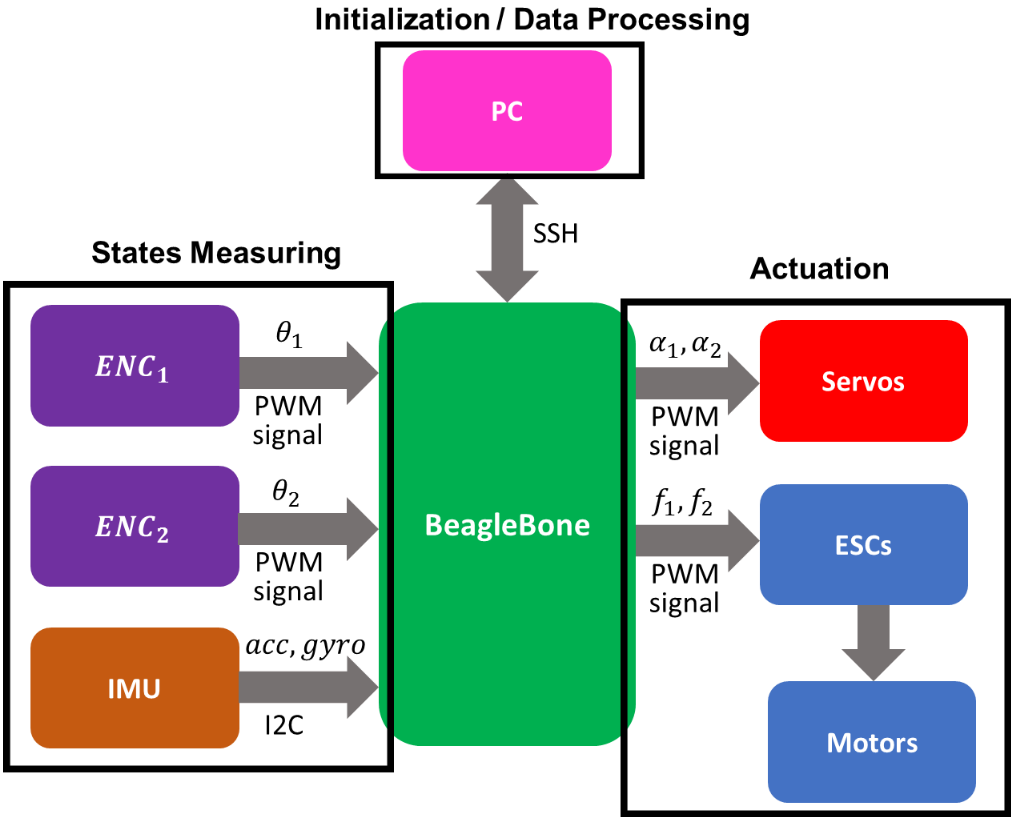

Figure 4.5: Test-bench hardware architecture

The test-bench is also instrumented with a set of sensors to estimate vehicle's orientation and position. For instance, a MPU-60X0 IMU, which is an integrated 6 motion tracking device with accelerometers, gyros and magnetometers, is attached to the TRBC's CG. Therefore, the vehicle attitude (θ_4) is basically obtained from a combination of the accelerometers and gyros

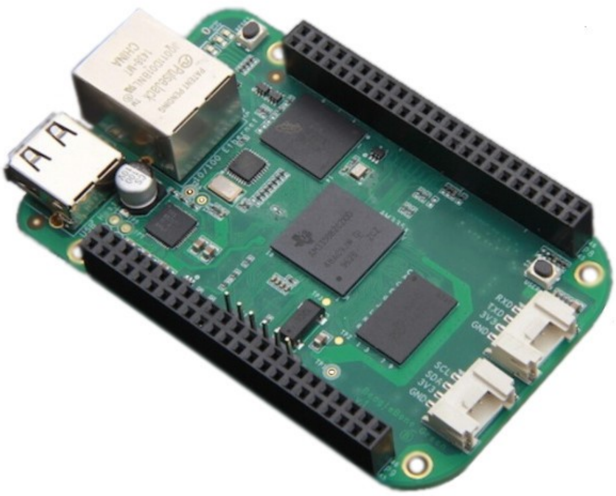

Figure 4.6: BeagleBone Green micro-controller board. Source: (BROWN, 2018)

signal. Once measured IMU raw data is very noisy, the output signal is filtered using a Kalman Filter to attenuate the external disturbances. The Kalman code is released under the General Public Lincence available at Lauszus (2017).

For the purpose of estimating the vehicle's position, two Autonics® E40S6-1000-6-L-5 incremental rotary encoders, namely ENC_1 and ENC_2, with 1000 pulse per revolution, are installed at points P_1 and P_2 illustrated in Fig. 4.1. As a result, ENC_1 and ENC_2 are used to estimate the TRBC lateral and vertical position and velocity, respectively. The encoders properties are described in Table 4.3

Table 4.3: Autonics® E40S6-1000-6-L-5 rotary encoder.

Property	
Type	Incremental
Shaft type	40 mm shaft
Resolution	1000 pulses
Voltage	5 VDC
Maximum current	80 mA

All the electric systems are connected to the same power supply. The two motors receive 12V while the low load devices (encoders and servos) are connected to a 5V source. A personal computer (PC) with Linux operational system is connected to the BeagleBone remotely via SSH communication. The device is used for code development, experiment initialization and data processing.

4.4 Software Implementation

All the codes for state estimation, data filtering, control law, motors and servos actuation were developed in C++ language and embedded in the BeagleBone. The software implementation was adapted from Jeronimo (2019). An schematic architecture of the software routine is shown in Fig. 4.7. The role of each of the steps are detailed below.

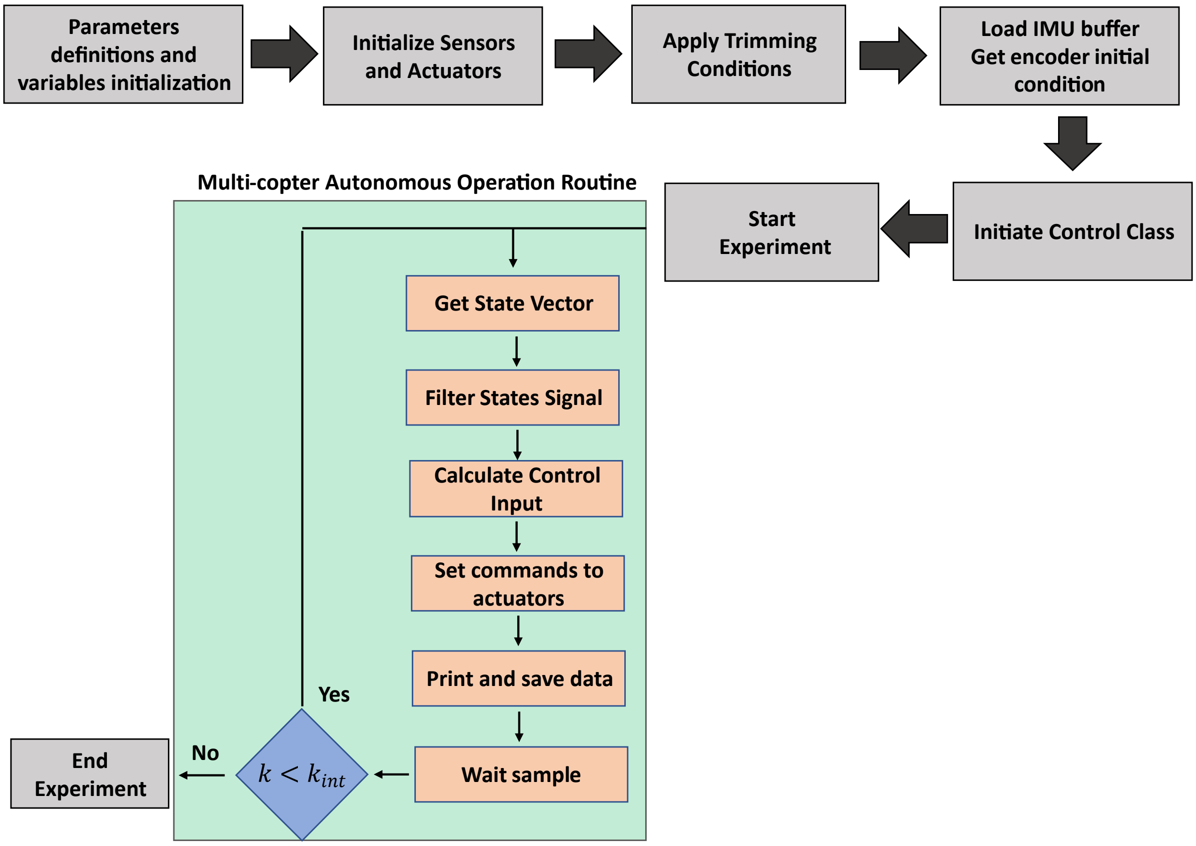

Figure 4.7: Test-bench software implementation architecture.

4.4.1 Parameters definitions and variables initialization

When the software routine starts, the first step is to initiate all the variables used in the process. In this case, most of them, e.g. state and control vectors, are defined as matrices using the Armadillo library (SANDERSON; CURTIN, 2016). The choice of data manipulation using vectors and arrays was based on the idea that matrix operations become more intuitive.

Further, some parameters regarding the experiment process are defined. They are: sample time, number of iterations, file name to save data, actuators trimming conditions and control reference values. These can be specified by the user in advance of starting the algorithm.

4.4.2 Initialize Sensors and Actuators

Once the experiment parameters are defined, the IMU, encoders, motors and servos are initialized. Each of them has its own C++ class containing specific functions for their operation.

For instance, in the *Motor* class, first is it specified the PWM address connection for each motor. Then, the motors period and the activation duty-cycle are set as 3.333 $[ns]$ and 1.000 $[ns]$, respectively, in order to create a *Motor* object. The class also has functions to: set duty-cycle, convert a force from Newton to duty-cycle and saturation of motor maximum and minimum forces. Analogously, the *Servo* class creates an object specifying a PWM address and setting the period to 2.000 $[ns]$. Tilt servo specific functions are available such as: set duty-cycle, convert angle to duty-cycle and deflection saturation.

The *Sensor* class is responsible for getting all the measurements from the encoder and IMU sensors, pre-process the data and return the state vector at each time sample. For the IMU device, there are functions to initialize, get the accelerometer and gyro raw data, correct the offset and filter the data using a Kalman filter. Similarly, the encoder is initialized setting a PWM address and defining the sampling period of 2.000 $[ns]$. A function is available to get the encoder position and calculate the angular velocity. These two are calculated based on the number pulses counted during the encoder sampling period. The *Sensor* class has also functions to filter the data using move average filter or low pass filter, arrange the state vector, hold process to reach the desired sample time and print data.

4.4.3 Apply Trimming Conditions

In this study, it is assumed that the TRBC linear model, which is used for the control design, is valid around the hover equilibrium condition. Thus, it is required to set the actuators to the control design trimming condition before starting the operational control test. This is accomplished by setting the thrust force of motors 1 and 2 to 1.7 $[N]$ and positioning them vertically ($\alpha_{1,2} = 0$). It must be recalled that the equilibrium trust can be adjusted by the user by positioning the counter-weight position and mass.

4.4.4 Load IMU buffer and get encoder initial condition

Once the installed encoders are incremental, it is important to define the initial condition before starting the experiment in order to get the correct relative angular position. In addition, it is recommended to acquired the IMU signal through a range of samples so that the Kalman filter output reaches steady state condition. As a result, a set of sequential readings through 100 time samples is collected to estimate the experiment initial conditions.

4.4.5 Initiate Control Class

The *Control* class is the one responsible for calculating the required commands to accomplish the control task according to a control law. In particular, the class receives as input the state vector of each time step and returns the motor forces and angular velocities. As mentioned previously, in this work, two control techniques are studied and their control laws are programmed in the micro-controller. They are the LQR and MPC.

For the LQR controller, the *Control* object is initiated importing the gain matrices from an '*.txt*' file. Also, the number of states and control commands as the reference tracking positions are defined.

For the MPC class initialization, all the matrices are imported from external files. They include prediction, constraint and other matrices used to solve the quadratic optimization problem. From its part, the MPC solution is obtained with the aid of the *qpOASES* toolbox (FERREAU et al., 2014). This library is an open source C++ implementation of the active set optimization which can be employed to solve parametric quadratic programming problems. Then, using the *qpOASES*, the *qProblem* is initiated. From the latter, the MPC optimal solution sequence is calculated recursively and the tilt angles and motor forces are estimated at each time step.

4.4.6 Multi-copter autonomous operation routine

As soon as all the objects are created and the parameters are defined, the test is ready to start. The experiment follows the routine illustrated inside the green box in Fig. 4.7. All the steps are performed by the class functions presented earlier. It is worth to mention that the servos and motors commands can be calculated either using the MPC or the LQR control rule. Then, the input signals are set in the actuator bus by converting the calculated tilt angles and motor forces to PWM signal. Moreover, the time to execute each routine step is monitored to avoid system delays specially due to the quadratic programming optimization performed by qpOASES. In the *wait sample* task, the algorithm holds its execution until the sample time clock is reached.

Finally, the experiment ends when the number of iterations is achieved. Then, the actuators are deactivated. The data becomes available for analysis in a '*.txt*' file.

4.5 Chapter Summary

- In order to accomplish the study objectives, the real implementation of the proposed control laws demanded the design and construction of a tilt-rotor bi-copter test bench.

The apparatus was designed selecting off the shelf components with relative low cost.

- The study is carried out assuming a TRBC with two tilt-rotor mechanisms capable of deflecting longitudinally. The mechanism dynamics can be modeled as a four bar linkage. Additionally, it excursion is limited between 0 and 35 $[deg]$.
- The test bench allow 3 DOF rotations which are analogous to an UAV lateral position (θ_1), altitude (θ_2) and attitude (θ_4).
- All the test bench processes - sensor reading, control law algorithm, actuation and data processing - are executed by a dedicated embedded micro-controller. For test systematization, a software framework was developed and implemented in the system.

CHAPTER V

Test Bench Dynamics

In this section, the dynamic model of the bi-copter test bench, presented in Section 4, is derived. The proposed structure can be studied as an open chain robotic manipulator whose end-effector is the TRBC. Therefore, its direct kinematic problem can be addressed using the classical formulation from robotics literature. First, the serial chain kinematics is presented assuming 4 degrees of freedom. Later, the equations of motion are derived using Lagrange formulation. Finally, the model is linearized assuming small perturbations.

5.1 Test Bench Kinematics

Pursuing the systematization of joints modelling, the Denavit-Hatenberg (DH) convention is adopted to define the relative position and orientation of each link of the test bench structure (SICILIANO et al., 2009).

5.1.1 Homogeneous Transformations

Two different reference systems are used to represent the robotic arm, as illustrated in Fig. 5.1. First, an inertial, global fixed coordinate system denoted by $\{O_g; x_g, y_g, z_g\}$. Second, a set of reference systems attached to the center of each robotic joint designated by $\{O_{ji}; x_{ji}, y_{ji}, z_{ji}\}$. According to the DH convention, it is convenient to adopt some rules to define the link frames as follows:

1. the z_{ji} axis corresponds to the revolution axis of the i-th joint;
2. the x_{ji} corresponds to the normal common to the z_{ji-1} and z_{ji} axes;
3. if the axes of the joints $i-1$ and i are concurrent, O_{ji-1} and O_{ji} are defined in the intersection point.

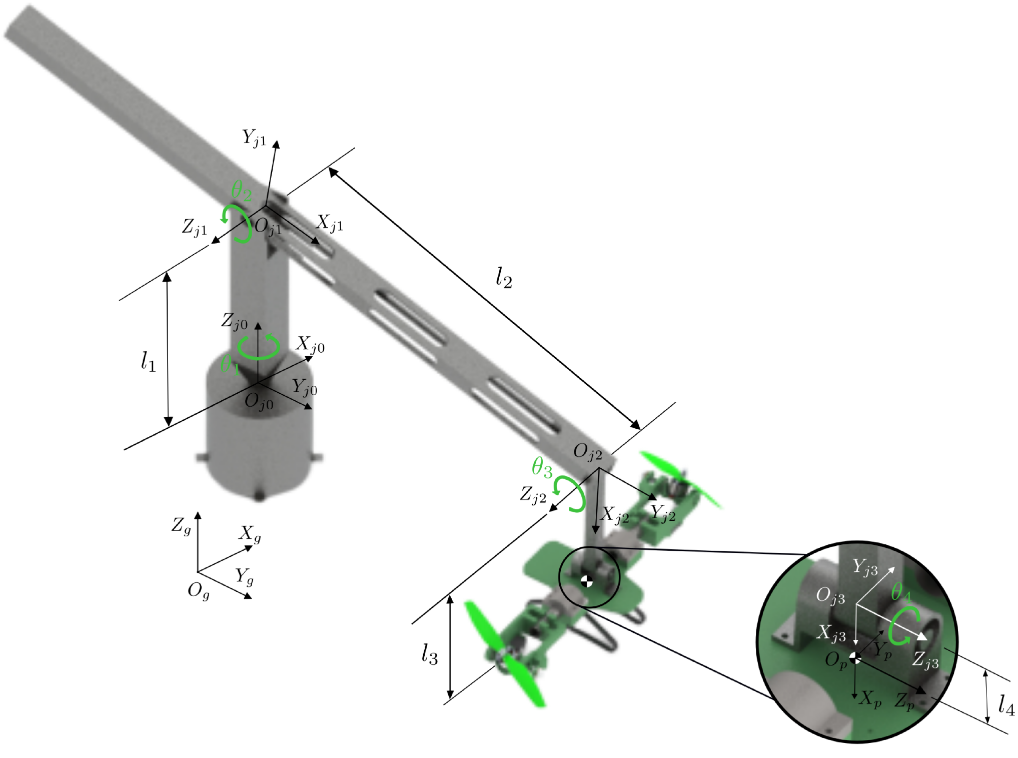

Figure 5.1: Test bench scheme.

Once the link frames have been established, the position and orientation of Frame i with respect to Frame $i-1$ are specified using four DH parameters:

- a_i: angle between z_{ji-1} and z_{ji} axes measured with respect to the x_{ji} axis;

- d_i: distance between z_{ji-1} and z_{ji} in x_{ji} direction;
- θ_i: angle between the x_{ji-1} and x_{ji} axes measured with respect to the z_{ji-1} axis;
- r_i: distance between x_{ji-1} and x_{ji} in z_{ji-1} direction;

It is worth mentioning that two of the four parameters (a_i and d_i) are always constant and depend only on the geometry of the connection between consecutive joints. Moreover, the articular variable q_i can assume the values of θ_i or r_i for a revolute or prismatic joint, respectively.

By using these parameters, it is possible to define a homogeneous transformation matrix $\mathbf{T}^i_{i-1}$, for the i-th joint reference frame, as follows:

$$\mathbf{T}^i_{i-1} = \begin{bmatrix} \cos\theta_i & -\sin\theta_i\cos a_i & \sin\theta_i\sin a_i & d_i\cos a_i \\ \sin\theta_i & \cos\theta_i\cos a_i & -\cos\theta_i\sin a_i & d_i\sin a_i \\ 0 & \sin a_i & \cos a_i & r_i \\ 0 & 0 & 0 & 1 \end{bmatrix} = \begin{bmatrix} \mathbf{R}^i_{i-1} & \mathbf{r}^i_{i-1} \\ \mathbf{0}_{3\times 3} & 1 \end{bmatrix} \tag{5.1}$$

Notably, $\mathbf{T}^i_{i-1}$ is composed by the rotation matrix $\mathbf{R}^i_{i-1} \in \mathbb{R}^{3\times 3}$ and the position vector $\mathbf{r}^i_{i-1} \in \mathbb{R}^3$, which represents the origin of Frame i with respect to Frame $i-1$. Henceforth, by using the DH convention, the homogeneous transformation matrices, for each frame with respect to Frame 0, can be expressed as:

$$\mathbf{T}^0_n = \prod_{i=1}^{n} \mathbf{T}^i_{i-1} \tag{5.2}$$

Specifically, the test bench structure is composed by 4 revolute joints which rotations are represented by the angles (θ_1, θ_2, θ_3 and θ_4), as described in Section 4 whose DH parameters are presented in Table 5.1.

Table 5.1: Test Bench DH parameters.

Frame	r_i	a_i	d_i	θ_i
1	0	$\frac{\pi}{2}$	0	θ_1
2	0	0	l_2	θ_2
3	0	$-\frac{\pi}{2}$	l_3	θ_3
4	0	0	l_4	θ_4

For the sake of simplicity, some assumptions can be made regarding the test bench structure:

- O_{j0} is adopted to be coincident with O_{j1};
- components 1 CG is coincident with O_{j1} (this assumption is valid assuming that a counterweight is positioned to balance the TRBC and component 2);
- component 3 is always aligned with z_3 direction due TRBC weight. Henceforth, $\theta_3 = (-\pi/2 - \theta_2)$, $\sin(\theta_2 + \theta_3) = -\sin(-\pi/2) = -1$ and $\cos(\theta_2 + \theta_3) = -\cos(-\pi/2) = 0$;
- the TRBC CG is coincident with O_{j3} (assuming that l_{cg} distance is small);
- external forces and moments, due to the TRBC motors, are expressed in $\{O_p; x_p, y_p, z_p\}$.

As a result, the homogeneous transformation matrices $\mathbf{T}_1^0$, $\mathbf{T}_2^0$ and $\mathbf{T}_3^0$ are:

$$\mathbf{T}_1^0 = \begin{bmatrix} \cos\theta_1 & 0 & \sin\theta_1 & 0 \\ \sin\theta_1 & 0 & -\cos\theta_1 & 0 \\ 0 & 1 & 0 & 0 \\ 0 & 0 & 0 & 1 \end{bmatrix} \tag{5.3}$$

$$
\mathbf{T}_2^0 = \begin{bmatrix} \cos\theta_1\cos\theta_2 & -\cos\theta_1\sin\theta_2 & \sin\theta_1 & l_2\cos\theta_1\cos\theta_2 \\ \sin\theta_1\cos\theta_2 & -\sin\theta_1\sin\theta_2 & -\cos\theta_1 & l_2\sin\theta_1\cos\theta_2 \\ \sin\theta_2 & \cos\theta_2 & 0 & l_2\sin\theta_2 \\ 0 & 0 & 0 & 1 \end{bmatrix} \tag{5.4}
$$

$$
\mathbf{T}_3^0 = \begin{bmatrix} 0 & -\sin\theta_1 & \cos\theta_1 & l_2\cos\theta_1\cos\theta_2 \\ 0 & \cos\theta_1 & \sin\theta_1 & l_2\sin\theta_1\cos\theta_2 \\ -1 & 0 & 0 & l_2\sin\theta_2 - l_3 \\ 0 & 0 & 0 & 1 \end{bmatrix} \tag{5.5}
$$

$$
\mathbf{T}_4^0 = \begin{bmatrix} -\sin\theta_1\sin\theta_4 & -\sin\theta_1\cos\theta_4 & \cos\theta_1 & l_2\cos\theta_1\cos\theta_2 \\ \cos\theta_1\sin\theta_4 & \cos\theta_1\cos\theta_4 & \sin\theta_1 & l_2\sin\theta_1\cos\theta_2 \\ -\sin\theta_4 & \sin\theta_4 & 0 & l_2\sin\theta_2 - l_3 \\ 0 & 0 & 0 & 1 \end{bmatrix} \tag{5.6}
$$

In this manner, any vector $\mathbf{s}_p$ described in homogeneous coordinates in $\{O_p; x_p, y_p, z_p\}$ can be written in $\{O_0; x_0, y_0, z_0\}$ by using the transformation $\mathbf{s}_0 = \mathbf{T}_4^0 \mathbf{s}_p$.

5.1.2 Joints Kinematics

By assuming the test bench as an open chain manipulator, in order to define the TRBC trajectory, one must derive a relationship between the joint velocities and the end-effector linear an angular velocities. This can be expressed by means of each i-th joint kinematic tensor with respect to Frame $i-1$ ($v_{i-1}^i(P) \in \mathbb{R}^3$) as follows

$$v_{i-1}^{i}(P) = \begin{bmatrix} \kappa_{i-1}^{i} \times (\mathbf{R}_{i-1}^{i} \sigma_P^{R_i}) \\ \kappa_{i-1}^{i} \end{bmatrix} \dot{q}_i \tag{5.7}$$

where κ_{i-1}^{i} denotes the rotation axis of joint i, $\sigma_P^{R_i} \in \mathbb{R}^3$ represents the position vector of point P of any i component written in frame R_i and $\dot{q}_i$ the angular velocity of joint i. By assuming that O_1, O_3 and O_4 are coincident with their respective component CG position (G_i), vector $\sigma_{G_i}^{R_i}$ will be zero for those elements. For element 2, $\sigma_{G_2}^{R_2} = [l_3/2\ 0\ 0]$.

Therefore, from Eq. (5.7), the kinematic tensor of each test bench element can be described with respect to G_i as

$$v_1^0(G_1) = \begin{bmatrix} z_{j1}^{j0} \times (\mathbf{R}_1^0 \mathbf{0}_{3\times1}) \\ z_{j1}^{j0} \end{bmatrix} \dot{\theta}_1 = \begin{bmatrix} \mathbf{0}_{5\times1} \\ 1 \end{bmatrix} \dot{\theta}_1 \tag{5.8}$$

$$v_2^1(G_2) = \begin{bmatrix} z_{j2}^{j1} \times (\mathbf{R}_2^1 \sigma_{G_2}^{R_2}) \\ z_{j2}^{j1} \end{bmatrix} \dot{\theta}_2 = \begin{bmatrix} -0.5 l_2 \sin\theta_2 \\ 0.5 l_2 \cos\theta_2 \\ 0 \\ 0 \\ 0 \\ 1 \end{bmatrix} \dot{\theta}_2 \tag{5.9}$$

$$v_3^2(G_3) = \begin{bmatrix} z_{j3}^{j2} \times (\mathbf{R}_3^2 \mathbf{0}_{3\times1}) \\ z_{j3}^{j2} \end{bmatrix} \dot{\theta}_3 = \begin{bmatrix} \mathbf{0}_{5\times1} \\ 1 \end{bmatrix} \dot{\theta}_3 \tag{5.10}$$

$$v_4^3(G_4) = \begin{bmatrix} z_{j4}^{j3} \times (\mathbf{R}_4^3 \mathbf{0}_{3\times 1}) \\ z_{j4}^{j3} \end{bmatrix} \dot{\theta}_4 = \begin{bmatrix} \mathbf{0}_{5\times 1} \\ 1 \end{bmatrix} \dot{\theta}_4 \tag{5.11}$$

As a direct result of the kinematic tensor definition, it is convenient to write Eqs. (5.8) to (5.11) from Frame $i-1$ to Frame 0 in order to evaluate the trajectory of the end-effector with respect to a fixed frame. Consequently, its angular and linear velocity can be described as function of the joints position an velocities ($\mathbf{q}$ and $\dot{\mathbf{q}}$) in the form:

$$v_n^0(P) = \mathbf{J}_n^0(\mathbf{q})\dot{\mathbf{q}} \tag{5.12}$$

where $\mathbf{J}_n^0(\mathbf{q})$ is known as the kinematic Jacobian matrix.

For the purpose of describing the kinematic tensors in Frame 0, the composition law can be applied (SICILIANO et al., 2009)

$$v_n^0(P) = \sum_{i=0}^{n-1} \begin{bmatrix} \mathbf{R}_{i-1}^0 & \mathbf{0}_{3\times 3} \\ \mathbf{0}_{3\times 3} & \mathbf{R}_{i-1}^0 \end{bmatrix} v_{i+1}^i(P) \tag{5.13}$$

Thereby, by applying Eq. (5.13) in Eqs. (5.8) to (5.11), one can obtain, from Eq. (5.12), the kinematic Jacobian matrix in Frame 0 for each element i

$$\mathbf{J}_1^0(\mathbf{q}) = \begin{bmatrix} 0 & 0 & 0 & 0 \\ 0 & 0 & 0 & 0 \\ 0 & 0 & 0 & 0 \\ 0 & 0 & 0 & 0 \\ 0 & 0 & 0 & 0 \\ 1 & 0 & 0 & 0 \end{bmatrix} \tag{5.14}$$

$$\mathbf{J}_2^0(\mathbf{q}) = \begin{bmatrix} 0 & \frac{-l_2 \cos\theta_1 \sin\theta_2}{2} & 0 & 0 \\ 0 & \frac{-l_2 \sin\theta_1 \sin\theta_2}{2} & 0 & 0 \\ 0 & \frac{-l_2 \cos\theta_2}{2} & 0 & 0 \\ 0 & \sin\theta_1 & 0 & 0 \\ 0 & -\cos\theta_1 & 0 & 0 \\ 1 & 0 & 0 & 0 \end{bmatrix} \tag{5.15}$$

$$\mathbf{J}_3^0(\mathbf{q}) = \begin{bmatrix} 0 & \frac{-l_2 \cos\theta_1 \sin\theta_2}{2} & 0 & 0 \\ 0 & \frac{-l_2 \sin\theta_1 \sin\theta_2}{2} & 0 & 0 \\ 0 & \frac{-l_2 \cos\theta_2}{2} & 0 & 0 \\ 0 & \sin\theta_1 & \sin\theta_1 & 0 \\ 0 & -\cos\theta_1 & -\cos\theta_1 & 0 \\ 1 & 0 & 0 & 0 \end{bmatrix} \tag{5.16}$$

$$\mathbf{J}_4^0(\mathbf{q}) = \begin{bmatrix} 0 & \frac{-l_2 \cos\theta_1 \sin\theta_2}{2} & 0 & 0 \\ 0 & \frac{-l_2 \sin\theta_1 \sin\theta_2}{2} & 0 & 0 \\ 0 & \frac{-l_2 \cos\theta_2}{2} & 0 & 0 \\ 0 & \sin\theta_1 & \sin\theta_1 & \cos\theta_1 \\ 0 & -\cos\theta_1 & -\cos\theta_1 & \sin\theta_1 \\ 1 & 0 & 0 & 0 \end{bmatrix} \tag{5.17}$$

5.2 Lagrange Formulation

As aforementioned, the definition of kinematic tensors is helpful to describe the angular velocities of each joint. As a result, the motion of the TRBC can be evaluated for a fixed base frame. Nevertheless, in order to establish a relationship between the forces and torques applied by the TRBC motors and the motion of structure, a dynamic model of the manipulator is required. In the present study, Lagrange formulation is employed to derive the equations of motion in terms of the generalized coordinates $\mathbf{q} = [\theta_1 \ \theta_2 \ \theta_4]$, which effectively describe the link positions. The Lagrangian of the mechanical system can be defined as

$$\mathscr{L} = \mathscr{K} - \mathscr{P} \tag{5.18}$$

where $\mathscr{K}$ and $\mathscr{P}$ denote the total kinetic and potential energy of the system, respectively.

Then, the Lagrange equations are expressed by

$$\frac{d}{dt}\left(\frac{\partial \mathscr{L}}{\partial \dot{q}_i}\right) - \frac{\partial \mathscr{L}}{\partial q_i} = \Gamma_i \tag{5.19}$$

being Γ_i the generalized force associated with the generalized coordinate q_i. It is worth to mention that, the contributions to the generalized forces are given by the nonconservative forces, i.e., the joint actuator torques, the joint friction forces, as well the joint torques induced by end-effector interaction forces with the environment. For the test-bench scenario, the last is the most relevant since represents the forces and torques produced by the motors which are associated with the flying capability of the vehicle.

5.2.1 *Kinetic Energy*

The kinetic energy of element i can be described as function of the kinematic tensor

$$\mathscr{K}_i = \frac{1}{2}\dot{q}_i^T \underbrace{[\mathbf{J}_i^0(\mathbf{q})]^T \begin{bmatrix} m_i & 0 & 0 & \mathbf{0}_{1\times 3} \\ 0 & m_i & 0 & \mathbf{0}_{1\times 3} \\ 0 & 0 & m_i & \mathbf{0}_{1\times 3} \\ \mathbf{0}_{3\times 3} & \mathbf{0}_{3\times 3} & \mathbf{0}_{3\times 3} & \mathbf{I}_i \end{bmatrix} [\mathbf{J}_i^0](\mathbf{q})}_{\mathbf{D}_i(\mathbf{q})} \dot{q}_i \tag{5.20}$$

where m_i denotes the mass and $\mathbf{I}_i$ the matrix representing the moments of inertia with respect to the element CG of element i.

Henceforth, the manipulator total kinetic energy can be written as

$$\mathscr{K} = \sum_{i=1}^{n} \mathscr{K}_i = \sum_{i=1}^{n} \frac{1}{2}\dot{q}_i^T \mathbf{D}_i(\mathbf{q})\dot{q}_i = \frac{1}{2}\dot{\mathbf{q}}^T \mathbf{D}(\mathbf{q})\dot{\mathbf{q}} \tag{5.21}$$

5.2.2 *Potential Energy*

The potential energy of element i can be defined as

$$\mathscr{P}_i = m_i g z_{G_i}^{R_0} \tag{5.22}$$

being $z_{G_i}^{R_0}$ the projection of the vector representing each element CG position in z_0 direction.

$$\begin{aligned}
z_{G_1}^{R_0} &= 0 \\
z_{G_2}^{R_0} &= \tfrac{l_3 \sin\theta_2}{2} \\
z_{G_3}^{R_0} &= l_3(\cos\theta_2{}^2 - \cos\theta_2 - 1) \\
z_{G_4}^{R_0} &= l_3(\cos\theta_2{}^2 - \cos\theta_2 - 1)
\end{aligned} \tag{5.23}$$

Consequently, the total potential energy will be

$$\mathscr{P} = \sum_{i=1}^{n} \mathscr{P}_i(\mathbf{q}) \tag{5.24}$$

5.2.3 Final Dynamic Model

After deriving the manipulator kinetic and potential energy, one can substitute Eqs. (5.21) and (5.24) in Eq. (5.18) to define the Lagrangian. Then, the final dynamic model is obtained from Eq. (5.19), for each generalized coordinate q_i, resulting in

$$\mathbf{D}(\mathbf{q})\ddot{\mathbf{q}} + \mathbf{C}(\mathbf{q}, \ddot{\mathbf{q}}) + \mathbf{G}(\mathbf{q}) = \Gamma \tag{5.25}$$

It is worth to define the terms in Eq.(5.25). The term $\mathbf{D}(\mathbf{q})\ddot{\mathbf{q}}$ was presented in Eq. (5.21) and is related to the inertial contributions. Moreover, $\mathbf{C}(\mathbf{q}, \dot{\mathbf{q}})$ assign the centrifugal and

Coriolis contributions:

$$\mathbf{C}(\mathbf{q},\dot{\mathbf{q}}) = \left(\sum_{i=1}^{n} \frac{\partial \mathbf{D}(\mathbf{q})}{\partial q_k}\dot{q}_k\right)\dot{\mathbf{q}} - \begin{bmatrix} \frac{1}{2}\dot{\mathbf{q}}^T \frac{\partial \mathbf{D}(\mathbf{q})}{\partial q_1}\dot{\mathbf{q}} \\ \vdots \\ \frac{1}{2}\dot{\mathbf{q}}^T \frac{\partial \mathbf{D}(\mathbf{q})}{\partial q_n}\dot{\mathbf{q}} \end{bmatrix} \tag{5.26}$$

and $\mathbf{G}(\mathbf{q})$ is related to the gravity contributions:

$$\mathbf{G}(\mathbf{q}) = \begin{bmatrix} \frac{\partial \mathscr{P}(\mathbf{q})}{\partial q_1} \\ \vdots \\ \frac{\partial \mathscr{P}(\mathbf{q})}{\partial q_n} \end{bmatrix} = \sum_{i=1}^{n} m_i g \begin{bmatrix} \frac{\partial z G_{i/R0}}{\partial q_1} \\ \vdots \\ \frac{\partial z G_{i/R0}}{\partial q_n} \end{bmatrix} \tag{5.27}$$

Furthermore, the articulations efforts Γ can be defined by the following equation:

$$\Gamma = \Gamma_m - \Gamma_e - \Gamma_f(\mathbf{q},\dot{\mathbf{q}}) \tag{5.28}$$

where Γ_m represents the actuators efforts in the links of the robot arm, $\Gamma_f(q,\dot{q})$ is related to the viscous and friction efforts and Γ_e express interaction efforts between the kinematic chain and the environment. For instance, in this particular case, the motor thrust force is a result of the aerodynamic interaction of the propeller blade with the surrounding air.

One must recall that, in the present study, there is no actuator on the links and, for simplicity, the viscous and friction efforts are modeled as torque proportional to each joint velocity, i.e

$$\Gamma_f(\dot{q}) = [\mu_1 \; \mu_2 \; \mu_3 \; \mu_4]\dot{\mathbf{q}} \tag{5.29}$$

where μ_1, μ_2, μ_3 and μ_4 are constants. Moreover, it is necessary to substitute Γ_e, which represents the effort that is applied to the environment, by Γ_b, which represents the effort that the environment (the efforts generated by the TRBC motors), following the $\Gamma_b = -\Gamma_e$ relation. As a result,

$$\mathbf{D}(\mathbf{q})\ddot{\mathbf{q}} + \mathbf{C}(\mathbf{q}, \ddot{\mathbf{q}}) + \mathbf{G}(\mathbf{q}) - \Gamma_b + \Gamma_f(\dot{q}) = \mathbf{0}_{4\times 6} \tag{5.30}$$

5.2.4 Mechanism External Forces and Moments

The interaction forces between the TRBC and the environment Γ_e can be directly calculated using the kinematic Jacobian matrix. Assuming that $\mathbf{t}_e^0$ is the tensor representing the forces and moments applied by the manipulator end-effector, at its *CG*, over the environment expressed in Frame 0 as

$$\mathbf{t}_e^0 = [f_x \; f_y \; f_z \; \tau_x \; \tau_y \; \tau_z]^T \tag{5.31}$$

By applying the virtual work principle in Eq. (5.31)

$$\Gamma_e^T \cdot \dot{\mathbf{q}} = \mathbf{J}_{CG}^0 \cdot \mathbf{t}_e^{0^T} \cdot \dot{\mathbf{q}} \tag{5.32}$$

being $\mathbf{J}_{CG}^0$ the kinematic Jacobian matrix of the TRBC *CG* written in Frame 0 which, in particular, is given by

$$\mathbf{J}_{CG}^{0} = \begin{bmatrix} \sin(\theta_4) l_2 \cos(\theta_2) & -\cos(\theta_4) l_2 \cos(\theta_2) & 0 & 0 \\ \cos(\theta_4) l_2 \cos(\theta_2) & \sin(\theta_4) l_2 \cos(\theta_2) & 0 & 0 \\ 0 & -l_2 \sin(\theta_2) + l_3 & l_3 & 0 \\ -\cos(\theta_4) & -\sin(\theta_4) & -\sin(\theta_4) & 0 \\ \sin(\theta_4) & -\cos(\theta_4) & -\cos(\theta_4) & 0 \\ 0 & 0 & 0 & 1 \end{bmatrix} \tag{5.33}$$

Therefore, Γ_e can be written as

$$\Gamma_e = [\mathbf{J}_{CG}^{0}]^T \cdot \mathbf{t}_e^0 \tag{5.34}$$

5.2.5 TRBC Forces and Moments

As long as the the open chain manipulator has the TRBC as end-effector, the forces acting on its CG are related with the motor and tilt mechanism actuation. As discussed in Chapter 3, the net thrust force produced by each of motor propulsive set acts in the normal direction of the propeller disk. Considering the longitudinal tilt capability of the TRBC, as presented in Section 4, one can write the thrust force of the two motors f_1 and f_2 in Frame P as function of the tilt angles α_1 and α_2

$$\mathbf{F}_{T_B} = \begin{bmatrix} f_1 \cos\alpha_1 + f_2 \cos\alpha_2 \\ f_1 \sin\alpha_1 - f_2 \sin\alpha_2 \\ 0 \end{bmatrix} \tag{5.35}$$

It is worth noting that, as depicted in Fig. 5.1, x_P is point down (vertical direction) and

y_P is pointing in the lateral direction. Moreover, due to the test bench physical constraints, there is no effort in the z_P direction.

The thrust force asymmetry between motors 1 and 2 also induce a resulting torque the TRBC CG. As a result, the torque due to thrust can be written as

$$\mathbf{M}_{T_B} = \begin{bmatrix} 0 \\ 0 \\ f_1 \cos\alpha_1 L_1 - f_2 \cos\alpha_2 L_2 \end{bmatrix} \tag{5.36}$$

where L_1 and L_2 are the arm's length of the TRBC associated with motors 1 and 2, respectively.

As can be perceived from Eq. (5.36), the test bench physical constrains prevents torques to be induced in x_P and y_P directions. Additionally, the fan torque and the gyroscopic effect has no consequence since the system is locked to rotate about x_P and $f_{y_P} = 0$.

Now, substituting (5.35) and (5.36) in (5.31), the effort tensor $\mathbf{t}_e^0$ can be redefined

$$\mathbf{t}_e^0 = \begin{bmatrix} \cos\alpha_1 & \cos\alpha_2 \\ \sin\alpha_1 & -\sin\alpha_2 \\ 0 & 0 \\ 0 & 0 \\ 0 & 0 \\ L_1 \cos\alpha_1 & -L_2 \cos\alpha_2 \end{bmatrix} \begin{bmatrix} f_1 \\ f_2 \end{bmatrix} \tag{5.37}$$

In conclusion, the test bench dynamics can be mathematically represented by Eq. (5.30). By integrating this set of non-linear differential equations, it is possible to estimate the vehicle trajectory in terms of the link position, with respect to the fixed base frame, under the influence of the motor thrust force f_1 and f_2. As can be noted, the solution of Eq. (5.30) is not trivial and require numerical integration to determine the state evolution over time.

5.3 Linearization

In the present study, the LQR and MPC control formulations are based on a discrete linear state-space representation. Hence, for control purposes, the model must be linearized in order to form a first order derivative LTI (Linear Time Invariant) state-space system. To accomplish this, the small perturbation theory is applied. Then, all the equations can be written in a Taylor Series form truncated on its first order derivatives, assuming that each state and input is a small perturbation around its steady state operating condition. In particular, in order to represent the system dynamics, the adopted state vector is

$$\chi = [\theta_1\ \theta_2\ \theta_4\ \dot{\theta}_1\ \dot{\theta}_2\ \dot{\theta}_4]^T \tag{5.38}$$

which represents the angular position and velocities of links 1, 2 and 4. Moreover, the considered control vector includes the forces f_1 and f_2, and longitudinal tilt angles α_1 and α_2 of the two motors. Then,

$$\upsilon = [f_1\ f_2\ \alpha_1\ \alpha_2]^T \tag{5.39}$$

One may note that χ and υ represent perturbations around the equilibrium condition. For instance, the steady state condition is represented by the TRBC operating in a hover condition where $\chi = 0$ and $f_1 + f_2$ is in equilibrium with the TRBC weight. Then, the steady state variables can be calculated from Eq. (5.30). Additionally, for the sake of simplicity, the state and input vector are assumed as perturbed variables.

Given the state and input vectors, the resulting LTI model can be written as

$$\begin{aligned}
&\dot{\chi} = \mathbf{A}_{TB}\chi + \mathbf{B}_{TB}\upsilon \\
&\gamma = \mathbf{C}_{\mathbf{TB}}\chi
\end{aligned} \tag{5.40}$$

where

$$\mathbf{A}_{TB} = \begin{bmatrix} 0 & 0 & 0 & 1 & 0 & 0 \\ 0 & 0 & 0 & 0 & 1 & 0 \\ 0 & 0 & 0 & 0 & 0 & 1 \\ 0 & 0 & \frac{-l_2 f_{x0}}{den_1} & -\mu_1 & 0 & 0 \\ 0 & 0 & \frac{l_2 f_{y0}}{den_2} & 0 & -\mu_2 & 0 \\ 0 & 0 & \frac{-c}{I_{zz4}} & 0 & 0 & \frac{-\mu_4}{I_{zz4}} \end{bmatrix}, \tag{5.41}$$

$$\mathbf{B}_{TB} = \begin{bmatrix} 0 & 0 & 0 & 0 \\ 0 & 0 & 0 & 0 \\ 0 & 0 & 0 & 0 \\ 0 & 0 & \frac{l_2 f_{1_0}}{den_1} & \frac{-l_2 f_{2_0}}{den_1} \\ \frac{l_2}{den_2} & \frac{l_2}{den_2} & 0 & 0 \\ \frac{L_1}{I_{zz4}} & \frac{-L_2}{I_{zz4}} & 0 & 0 \end{bmatrix} \tag{5.42}$$

and $\mathbf{C}_{TB}$ is defined according to the required control task. It must be emphasized that, based on the sensors installed in the test-bench, all the states χ are measured and available. In this case $\mathbf{C}_{TB} = \mathbf{I} \in \mathbb{R}^{n_s \times n_y}$ with $n_y = n_s$ being n_y and n_s the number of outputs and states, respectively.

In Eqs. (5.41) and (5.42), $den_1 = {l_2}^2(m_2 + m_3 + m_4) + I_{zz1} + I_{zz2} + I_{zz3} + I_{zz4} + {l_6}^2 m_6$, $den_2 = I_{yy2} + 1/4{l_3}^2 m_2 + {l_2}^2(m_2 + m_3 + m_4) + {l_6}^2 m_6$, recalling that m_6 and l_6 are the counter-weight mass and distance to O_0, respectively. Also, the terms c and μ_4, represents joint 4 disbalance and friction terms, which can be estimated experimentally.

For some control designs and real control applications, a discrete time state-space model is needed. Thus, as presented in (FRANKLIN et al., 1998), the model can be obtained directly from the continuous time model (5.40) by applying a zero-order-hold method as follows

$$\begin{aligned} \chi(k+1) &= \bar{\mathbf{A}}_{\mathbf{TB}}\chi(k) + \bar{\mathbf{B}}_{\mathbf{TB}}\boldsymbol{\mu}(k) \\ \gamma(k) &= \bar{\mathbf{C}}_{\mathbf{TB}}\chi(k) \end{aligned} \tag{5.43}$$

where $\bar{\mathbf{C}}_{\mathbf{TB}} = \mathbf{C}_{\mathbf{TB}}$,

$$\bar{\mathbf{B}}_{\mathbf{TB}} = e^{\mathbf{A}_{\mathbf{TB}}T_s} \tag{5.44}$$

being T_s the sampling period, and

$$\bar{\mathbf{B}}_{\mathbf{TB}} = \left(\int_0^T e^{\mathbf{A}_{\mathbf{TB}}\tau} d\tau\right) \mathbf{B}_{\mathbf{TB}} \tag{5.45}$$

5.4 Test bench virtual model

For the purpose of testing and validating the derived model and the control formulation, a virtual model was created. In this case, the non-linear equations, developed in Section 5.2, were adopted to describe the test bench dynamics. In particular, the model was created in Matlab environment with the aid of the *rigidBody* function from the *Robotic System Toolbox* (CORKE, 1996). This function receives as argument the position of each joint, described in terms of the DH convention given in Table 5.1. In addition, the mass and inertia properties of each element are informed, individually, as presented in Table 4.1. As a result, the rigid bodies are assembled into a tree-structured robot model as depicted in Fig. 5.2.

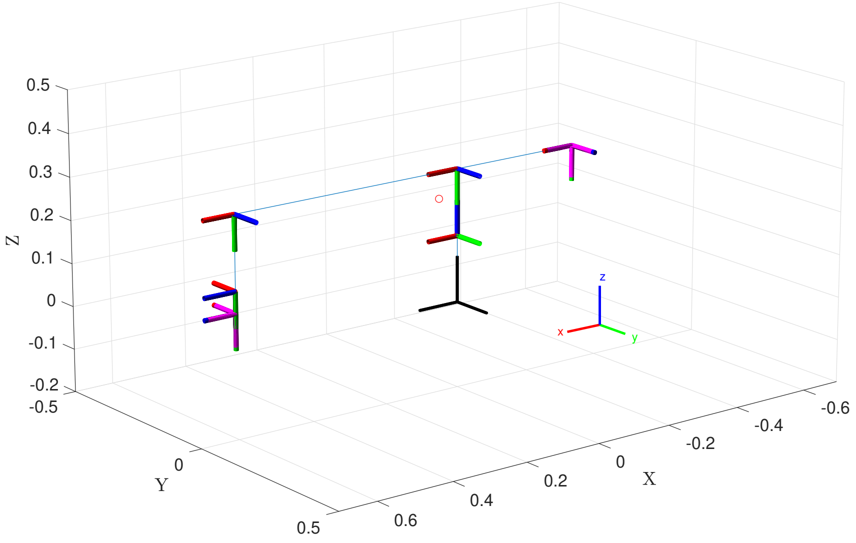

Figure 5.2: Matlab robot model.

The created robot model can be used to estimate the joints accelerations when the end-effector is subject to external forces and moments. Therefore, the simulation is carried out following the structure illustrated in Fig. 5.3. As can be seen, it is composed of 5 main steps:

- **Controller**: From the estimated state vector, it calculates the virtual control commands. The control architecture will be further discussed in the Control Design chapter.
- **Actuator Dynamics**: The desired control efforts from the controller are translated into effective actuator inputs, respecting the motor and tilt mechanism dynamics. This relation can be defined experimentally and will be explored in the System Identification chapter.
- **External Forces and Moments**: Given the thrust force and tilt angle deflection, the external forces and moments acting on the TRBC are determined using the formulation presented in Chapter 3.

- **Joints Dynamics**: In order to determine the joints accelerations, the open-chain manipulator inverse kinematic problem is solved numerically.
- **Integration**: The joint positions and velocities are calculated integrating the joints accelerations numerically. Then, the state vector (5.38) is fed to the controller.

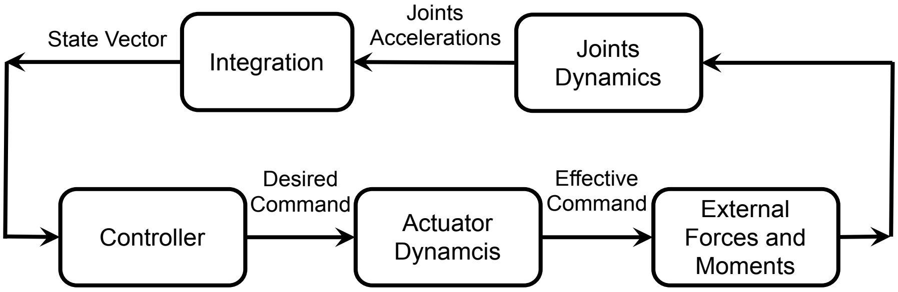

Figure 5.3: Main structure of the simulation model.

It is worth mentioning that, in this case, the joints friction torques were included in the model as proportional to the joints velocity. The friction constants are estimated experimentally as will be presented in the System Identification chapter.

5.5 Chapter Summary

- When attached to the test-bench, the TRBC is susceptible to the influence of the whole apparatus dynamics.
- The complete system can be seen as an open chain manipulator with 4 joints whose end-effector is the TRBC.
- The Denavit-Hatenberg convention can be used to establish the kinematic relations between the joints DOF and the TRBC movement as presented in Eq. (5.2).
- Lagrange formulation can be used to derive the test bench's dynamic model as shown in Eq. (5.30) considering the TRBC motor thrust effect as external forces and moments.

- In order to employ linear control formulations, the model is linearized assuming the TRBC at a hover condition (thrust and gravity forces in balance). In this case, the state vector are chosen as the joints positions and velocities. Moreover, the motors thrust force and tilt deflections are selected as control inputs.

CHAPTER VI

System Identification

Even though the dynamic parameters of the test-bench and TRBC can be obtained from the CAD models and physical principles, some properties can be estimated more accurately through experimental approaches. In this study, system identification procedures is used to determine some mechanical properties of the test-bench as listed bellow:

- TRBC inertia, friction constant of joint 4 and disbalance
- Motor set mapping and transfer function
- Tilt actuation mechanism mapping and transfer function
- Tilt command effectiveness and joint 1 friction
- θ_4 and θ_1 dynamic relation
- Motor command effectiveness and joint 2 friction

The adopted experiments and obtained results are presented subsequently.

6.1 TRBC inertia, friction constant of joint 4 and disbalance

In the interest of identifying the TRBC inertia (I_{zz4}), friction constant of joint 4 and disbalance, an specific experimental procedure was adopted. The idea is to approximate the system free response, for a given initial condition in θ_4 DOF, to a pendulum response expressed as:

$$I_{zz4}\ddot{\varphi} - \mu_4\dot{\varphi} - c\sin\varphi = 0 \tag{6.1}$$

being φ the pendulum angular position, μ_4 and c constants related with the joint 4 friction and disbalance, respectively.

To accomplish this, the following routine is employed:

1. First, the TRBC is brought to a given initial condition θ_{4_0} where it kept in rest, i.e. $\dot{\theta}_{4_0} = 0$;
2. The experiment initiate when the TRBC is released from its initial position;
3. The system response data (angular position and velocity) is recorded, using the IMU installed at the TRBC CG;
4. The steady-state value is removed from data to eliminate bias;
5. Candidate values of I_{zz4}, μ_4 and c in Eq. (6.1) are evaluated for the given initial condition, via numerical integration, and compared to the collected data;
6. The candidate function is selected through a Genetic Algorithm (CHIPPERFIELD et al., 1994) routine whose cost function minimizes the difference between the $j-th$ experimental data θ_{4_i} and $\dot{\theta}_{4_i}$ and the solution of Eq. (6.1) for each of n_{data} time samples,

that is

$$J_{fit_j} = \sum_{i=0}^{n_{data}} (\theta_{4_i} - \varphi_i)^2 + \sum_{i=0}^{n_{data}} \left(\dot{\theta}_{4_i} - \dot{\varphi}_i\right)^2$$

7. Finally, the best candidate function is the one which gives the minimum average of the J_{fit_j}, $j = 1, \dots, n_{exp}$ cost functions. Consequently, the identified parameters takes into account the variability of the initial condition.

It is noteworthy that the experiment is performed while θ_1 and θ_2 DOF are locked and the motors are operating in hoover angular velocity. Moreover, no duty-cycle command is set to the motors and/or tilt actuator during the experiment which means that the TRBC is under a free response.

After running the optimization algorithm in Matlab® environment, the identified dynamic parameters are $I_{zz4} = 0.0196$ $[kg \cdot m^2]$, $\mu_4 = 0.495$ $[kg \cdot m^2/(s \cdot rad)]$ and $c = 0.7347$ $[kg \cdot m^2/(s^2 \cdot rad)]$. Moreover, the TRBC free response and model identification for four different initial conditions is depicted in Fig. 6.1. As can be seen, the proposed model (6.1) represents the TRBC attitude dynamics efficiently for different initial conditions.

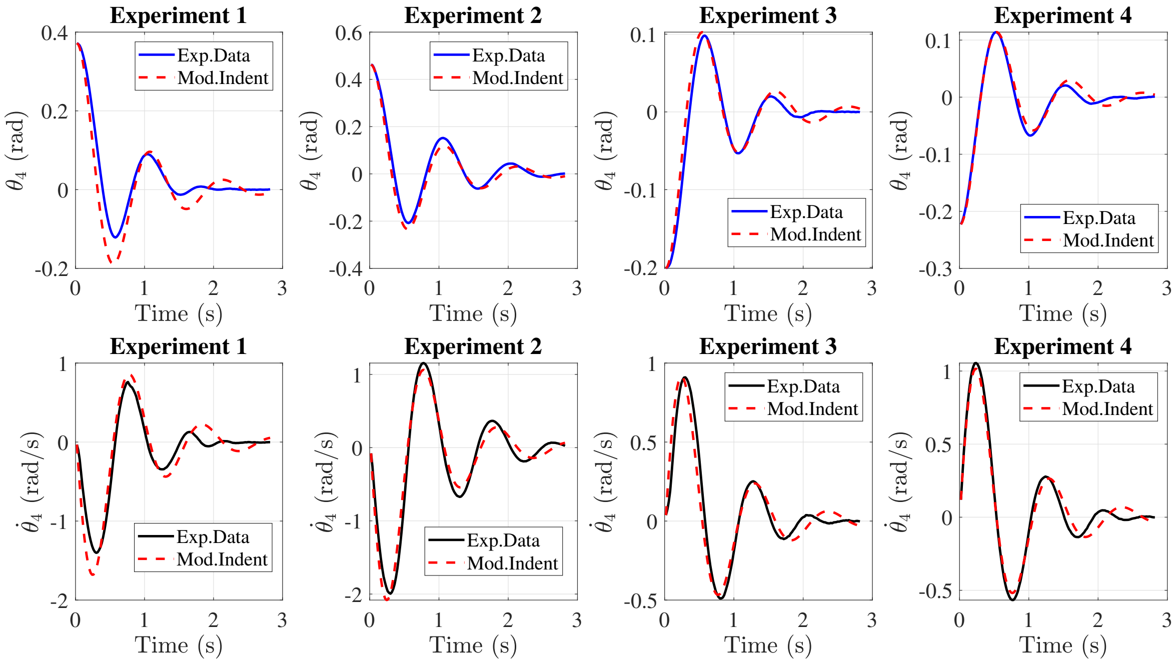

Figure 6.1: TRBC free response identification.

6.2 Motor set mapping and transfer function

As discussed in Section 4.2, the TRBC is equipped with 2 brushless DC motors. Typically, a multi-copter propulsive set is composed by a spinning rotor equipped a propeller responsible for generating the required thrust force. In particular, brushless electric motors have become the standard for multi-copters with a maximum take-off weight greater that 100 grams while brushed ones are still used for small vehicles (CONROY et al., 2014).

The propulsive set actuation can be summarized as illustrated in Fig. 6.2. Firstly, the Electronic Speed Controller (ESC) receives an input signal and is responsible for controlling the motor's commutation. Typically, the ESC input signal is supplied by a vehicle autopilot or microcontroller, most often in the form of a pulse-width modulated (PWM) or I^2C signal. The input value determines the average current the ESC should provide to the motor. Then, the motor uses the electrical power to spin its shaft, which is connected to a propeller, at a desired speed. Since it has an aerodynamic shape, the propeller generates lift as a result of the induced flow over its body. Consequently, it produces a net thrust force that acts on normal direction of propeller disc plane which is proportional to the square of the motor spinning velocity.

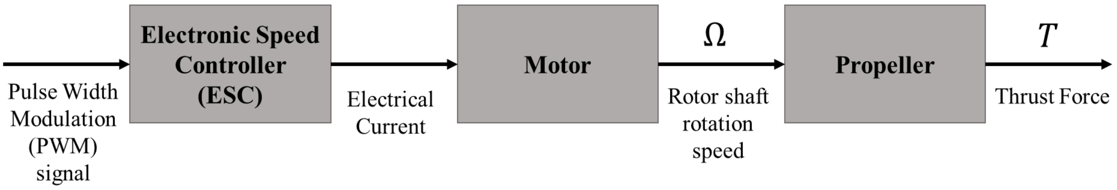

Figure 6.2: Typical brushless motor powertrain. Adapted from: (CONROY et al., 2014)

In the present study, the motor propulsive sets were experimented in order to map the PWM to net thrust force relation. This early procedure is known as static test. Additionally, a second test is proposed to identify the system dynamics in terms of its open-loop transfer function. For this purpose, a proper test rig, depicted in Fig. 6.3, was used for data gathering.

The test bench consists of a bending load cell fixed on a structure, responsible for the thrust force measurements. Additionally, an infrared sensor, fixed on the bed where the rotor with the propeller and ESC are mounted. The motor is attached 10 *mm* distance from the infrared sensor so that it is able to record the propeller rotational speed. An Arduino MEGA micro-controller, connected to a micro-computer, is used to set the PWM signal to the ESC and also receive the signal from the infrared sensor and load cell. All the data is collected and saved via the Arduino interface and post-processed in Matlab® environment.

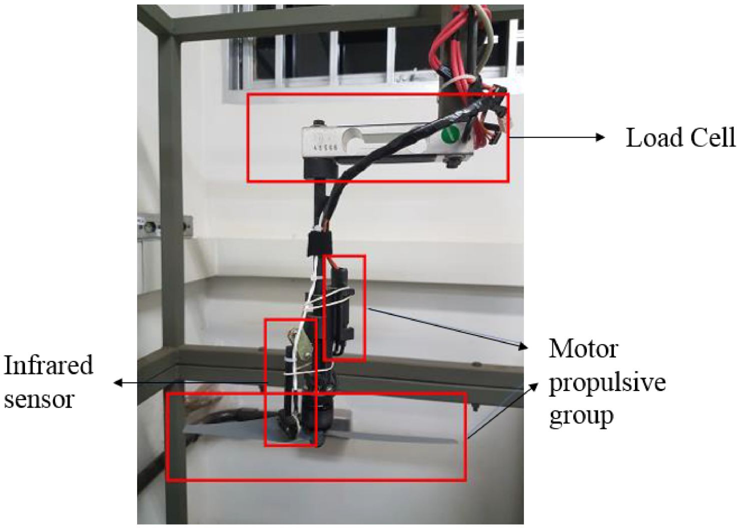

Figure 6.3: Motor propulsive set test bench.

6.2.1 PWM to Thurst Force Relation

This early experiment objective is to establish a mathematical relation between the input PWM signal from the micro-controller and the output thrust force measured by the load cell. To achieve this, a sequence of ascending and descending step signals is applied to the attached motor. Each step signal has amplitude of 50 [ms] and 3 [s] duration with a sample time of 12 [ms]. The PWM is applied to the motor's ESC from 1000 [ms] to 1700 [ms] as illustrated in Fig. 6.4 (b).

It must be pointed out that 1000 [ms] represents the minimum valid PWM for this specific motor set. In this condition the motors are engaged but their shafts remains at rest. Moreover, as evidenced by the experiments, when the PWM signal reaches 1700 [ms] the relationship between the thrust force and propeller angular speed is no longer quadratic due to the aerodynamic effects. Hence, this value is established as the maximum PWM boundary for this study.

Figure 6.4 (a) shows the thrust force output from the load cell for motors 1 and 2, which operate in counterclockwise and in clockwise directions, respectively. From the figure, one can infer that both motors have a similar static response. As a remark, the thrust force output signal was post-processed using a Moving Average Filter (MAF) (SMITH, 2013) with 20 samples window to eliminate the load cell noise.

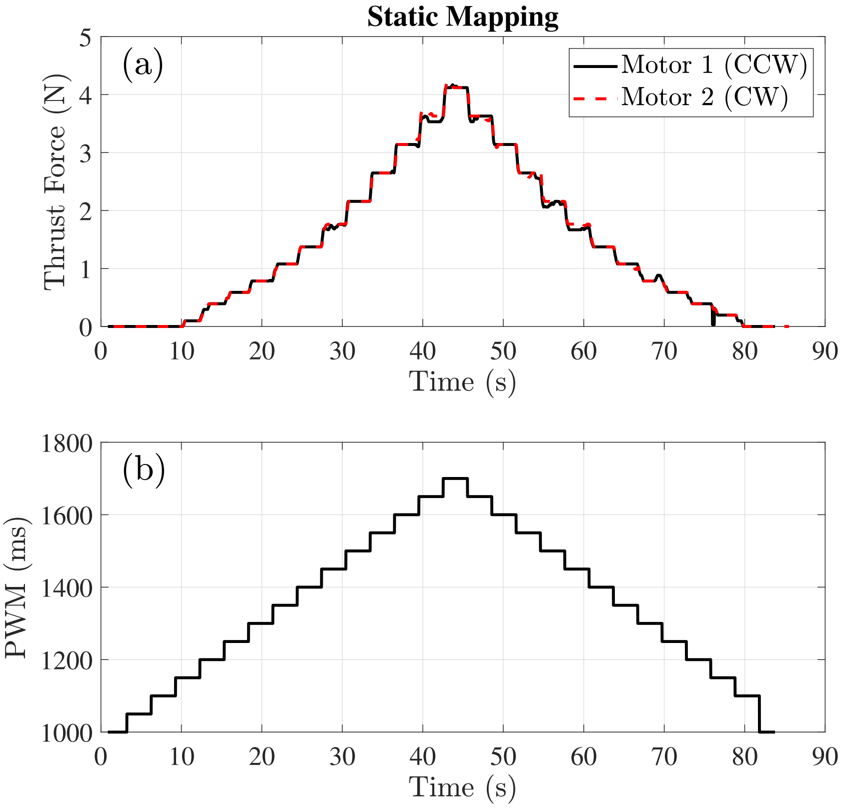

Figure 6.4: PWM input (a) and thrust force output (b) signals for motors 1 and 2.

Once the thrust force and PWM signals were acquired, curve fitting procedure is employed to estimate the PWM to force relation. It is worth mentioning that, for fitting purposes, the analysed PWM range was limited between $\text{PWM}_{min} = 1000\ [ms]$ and $\text{PWM}_{max} = 1700\ [ms]$ which represents 40% to 60% of the motors' operational range. This assumption is valid once the TRBC controller will operate with small perturbations around the trimming condition which is expected to be nearly $1450\ [ms]$ or 45%. By limiting the operational range, it is expected that the fitted models accuracy to be improved. Herein, first and second order polynomial functions were used to adjust the model.

The resulting fitting curves, using collected data from three diferent experiments, are depicted in Fig. 6.5. Moreover, the representing models, as function of the PWM period in [%], are presented below:

$$f_1(PWM) = \begin{cases} 0.0822 \cdot PWM - 2.0675 \\ 0.000459 \cdot PWM^2 + 0.036316 \cdot PWM - 0.944062 \end{cases} \tag{6.2}$$

for Motor 1 and

$$f_2(PWM) = \begin{cases} 0.0877 \cdot PWM - 2.2374 \\ 0.000797 \cdot PWM^2 + 0.00904 \cdot PWM - 0.285380 \end{cases} \tag{6.3}$$

for Motor 2.

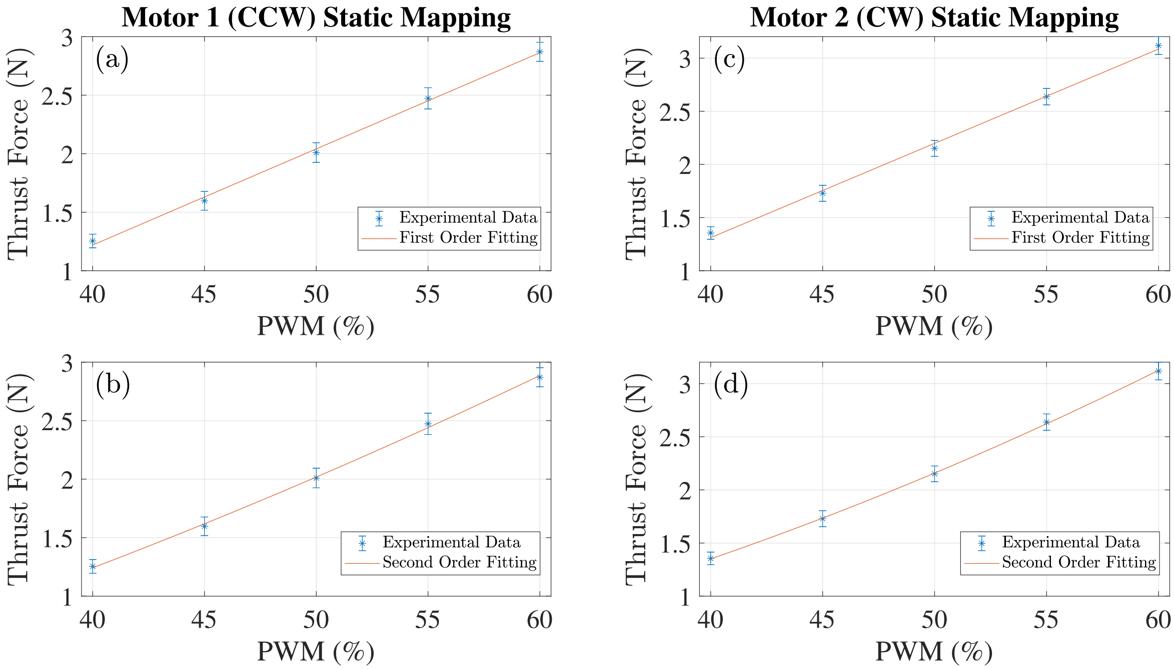

Figure 6.5: Motors 1 and 2 PWM *vs* thrust force linear (a) and (c) and second order fitting (b) and (d).

As a metric of accuracy, the norm of the residuals of the models is calculated so that they can be compared. For instance, for motor 1, $\sigma 1_{1st} = 5.1642$ and $\sigma 1_{2nd} = 5.0271$ for the first and second order fitting, respectively. It represents 2.62% of improvement from model 1 to model 2. Similarly, for motor 2, $\sigma 2_{1st} = 5.0131$ and $\sigma 2_{2nd} = 4.5788$, indicating that the second order model is 8.66% more accurate than the first order. It must be noted that, even though the difference in the norm of residuals are small, the second order model can be used since the required PWM for a given thrust can be easily calculated from the second order equations in (6.2) and (6.3).

From Fig. 6.5 and Eqs. (6.2) and (6.3) one can note that motors 1 and 2 have distinct relationship between thrust and PWM. As can be seen, the dependent and independent terms of the fitting models are different and, it follows that the each motor does not produce the same thrust force for the same PWM signal.

6.2.2 Open-Loop Transfer Function

In addition to the motor PWM to thrust force mapping presented above, the dynamic characterization of the motors is required. In many works, as in Rich (2012), the motor set transfer function is obtained in terms of the output propeller angular speed which can be measured by an optical sensor. However, the adopted approach requires the identification of the propeller parameters and dynamic relation between thrust to angular velocity relationship, which can be a cumbersome task. In this study, the direct PWM to thrust force transfer function estimation is preferred.

In order to achieve this, a second experimental procedure is proposed using the test-bench apparatus as illustrated in Fig. 6.3. This experiment consists of subjecting motors 1 and 2 to a sequence of PWM step inputs around a steady state condition. Particularly, the reference PWM is set as 1500 $[ms]$ with $\Delta\text{PWM} = \pm 50$ $[ms]$ step variations starting from -93.7 $[ms]$ to 106.3 $[ms]$. Figure 6.6 illustrates the motor set PWM input. Then, the thrust force variation Δf is recorded by the load cell for each time step. In this particular case, the sample time adopted for data acquisition is 12 $[ms]$. Later, the model transfer function is estimated in Laplace domain using the Matlab® System Identification Toolbox.

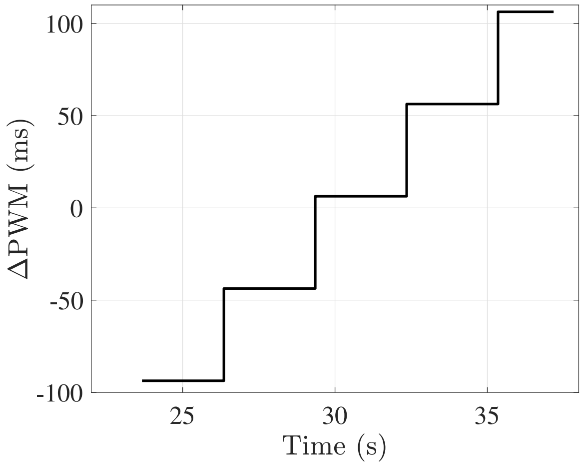

Figure 6.6: PWM step sequence input signal.

The results of motors 1 and 2 open-loop transfer function identification are shown in Fig. 6.7. Furthermore, the adjusted transfer functions can be represented in Laplace domain as

$$\frac{\Delta f_1(s)}{\Delta \mathrm{PWM}(s)} = \frac{0.08022}{s+9.072} \tag{6.4}$$

for motor 1 with an accuracy of 91.99% and

$$\frac{\Delta f_2(s)}{\Delta \mathrm{PWM}(s)} = \frac{0.0757}{s+8.895} \tag{6.5}$$

for motor 2 with an accuracy of 91.18%.

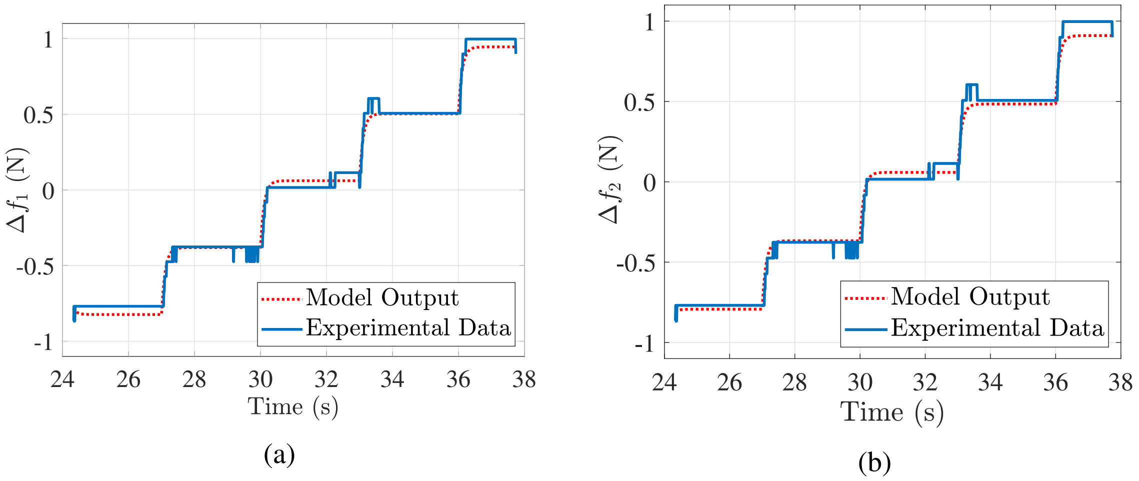

(a)

(b)

Figure 6.7: Experimental and model output force variation for motor 1 (a) and motor 2 (b).

As can be noted, motors 1 and 2 dynamics can be properly represented as a first order transfer function. As a rule of thumb, for this study it is assumed that a fitness accuracy greater than 85% is acceptable to represent the system dynamics. Equations (6.4) and (6.5) exhibit a single stable pole at $s_1 = -9.072$ and $s_2 = -8.895$, respectively. It can be clearly seen that, even though motors 1 and 2 sets are from the same model, their dynamic behavior is not equivalent. This evidence could compromise control efficiency and robustness on real applications.

Despite that, once it is guaranteed that poles s_1 and s_2 are far enough from the multicopter open-loop poles in s-plane, it can be assumed that the motor dynamics will not affect the system response significantly. If that is not the case, the motor dynamics shall be included in the design control model and the thrust force properly monitored during flight. Herein, as will be discussed later, the motor dynamics are neglected for control design purposes given that the thrust force can not be monitored and the motor responses are faster than the TRBC open-loop poles.

As a final remark, it must be emphasized that the identified PWM to thrust force relations (6.2) and (6.3), and open-loop transfer functions (6.4) and (6.5) are valid for the motor set described in Section 4.2 connected to a 12V power supply. Nevertheless, if one of the parameters and/or component is replaced - e.g. propeller, ESC, power supply voltage - the identification procedure must be repeated and a new regression model and transfer functions obtained.

6.3 Tilt actuation mechanism mapping and transfer function

Likewise the motor set, mapping and identification of the designed tilt mechanism are desired. Firstly, an accurate PWM to tilt angular position model is required to drive the motor at a desired angle. From this procedure, the mechanism excursion limits can be defined. Secondly, by identifying the open-loop transfer function one can infer about the influence of the mechanism dynamics in the vehicle response if the TRBC response.

A particular experimental procedure was adopted for the tilt mechanism identification similarly to the servo dynamic testing presented in Gasco (2012). The tilt mechanism, fixed to the TRBC arm and the potentiometer, are connected to a Arduino microcontroller. This later feeds the PWM signal and $5V$ to the servo and the potentiometer ADC signal is feedback. A protractor is attached to the arm with its center coincident with the motor tilt rotation axis. Figure 6.8 illustrates the apparatus assembly. The potentiometer map, static and dynamic tests are described below.

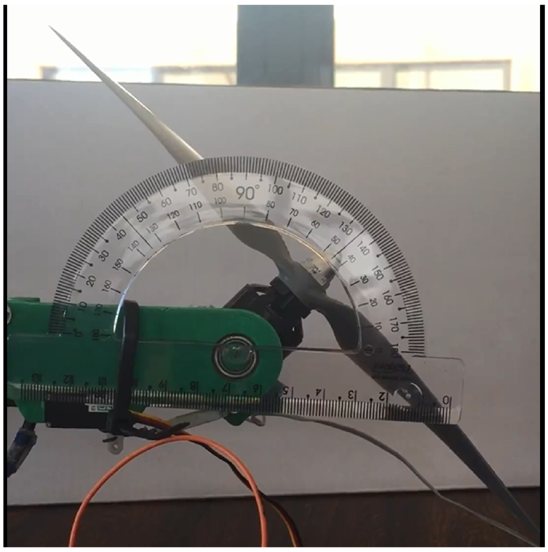

Figure 6.8: Tilt mapping apparatus assembly.

6.3.1 Potentiometer Mapping

To properly find a mathematical representation of the PWM servo input and the motor position (α) relation, the measure of the tilt position is needed. Therefore, first step is to map the potentiometer ADC output signal to its knob angular position. To accomplish this, the servo link is disconnected from the motor bet so that the motor can rotate freely. The potentiometer knob position adjusted between its limits (50° to 140°) with the aid of the protractor. Then, the output ADC signal, which can vary from 0 to 1024 bits, is recorded. Figure 6.9 illustrates the acquired data along with the fitted curve. The resulting linear model is found to be:

$$\alpha_{Pot} = 47.2534 + 0.2586 \cdot ADC \tag{6.6}$$

where ADC and α_{Pot} are the output signal in bits and the measured angle from the protractor in $[deg]$, respectively.

It must be pointed out that the independent term in (6.6) depends on the potentiometer assembly position in the TRBC arm. Therefore, this coefficient may vary from one tilt mechanism to another. A reference position can be adjusted with the aid of the protractor and added to the independent term to overcome this issue.

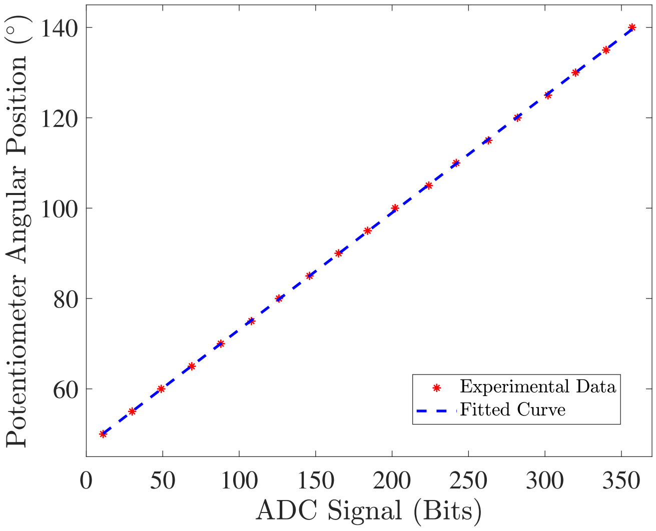

Figure 6.9: Tilt mapping apparatus assembly.

6.3.2 Tilt Mechanism Static Test

To establish a proper relation between the motor tilt angle and the servo PWM input signal, a static test was carried out as presented below

1. The servos are feed a PWM signal of 1.65 [ns], positioning the motors close to a vertical position;
2. PWM signal is varied starting from 1.65 [ns] to 2.35 [ns], which corresponds to 55% and 78.3 % of duty-cycle, respectively. In this case a period of 3.0 [ns] is adopted;
3. For each input value, the feedback ADC value of the potentiometer is recorded;
4. The tilt angle (α) is calculated using the model (6.6);

5. It is found the offset tilt angle whose potentiometer's calculated angle is equivalent to the zero tilt position - i.e. the motor in a vertical position;
6. The offset is removed from the acquired data;
7. Curve fitting procedure, using first and second order polynomial functions, is applied to identify the model that relates PWM input to tilt angle (α);
8. Best model is selected after the test is repeated 3 times for tilt mechanisms 1 and 2.

Figure 6.10 illustrates the tilt mechanisms static mapping data and the obtained fitting models for a set of 3 experiments. The models are found to be:

$$\alpha_1(PWM) = \begin{cases} -13.1416 \cdot PWM + 19.1760 \\ 1.0501 \cdot PWM^2 - 13.1415 \cdot PWM + 18.1260 \end{cases} \tag{6.7}$$

for tilt mechanism 1 and

$$\alpha_2(PWM) = \begin{cases} -12.128 \cdot PWM + 11.8955 \\ 1.8493 \cdot PWM^2 - 13.1415 \cdot PWM + 10.0463 \end{cases} \tag{6.8}$$

for tilt mechanism 2, where PWM is given in [ns].

The norm of residuals is compared for the first and second order models. For tilt mechanism 1, $\sigma 1_{1st} = 361.03$ and $\sigma 1_{2nd} = 347.20$ while for tilt mechanism 2, $\sigma 1_{1st} = 308.63$ and $\sigma 1_{2nd} = 254.73$. These results corresponds to an improvement of 3.83% and 17.46%, respectively, from first to second order polynomial model. One can conclude that the second order model is preferred, specially for tilt mechanism 2. It must be noted that, even though both tilt mechanisms were designed as a push-pull servo, with same components and dimensions, the difference between the PWM-α is related with the set assembly.

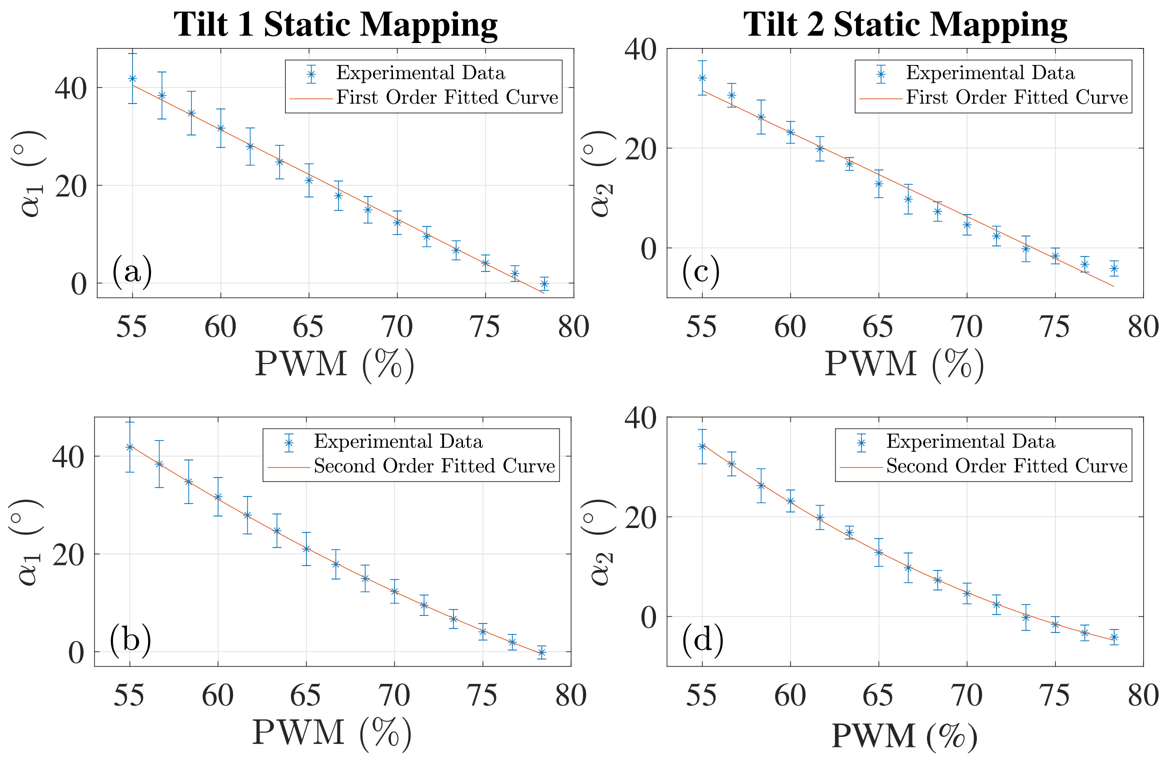

Figure 6.10: Tilt mechanisms 1 and 2 PWM *vs* angular position first (a) and (c) and second order fitting (b) and (d).

6.3.3 *Tilt Mechanism Dynamic Test*

To characterize the open-loop tilt mechanism response, a dynamic test is required. The aim of this test is to identify the transfer function by fitting the model's output to a given sequence of PWM inputs. In this case, the apparatus assembly depicted in Fig. 6.8 is used to execute the experiment for tilts 1 and 2. The test procedure is summarized as follows:

1. The motor starts to run at a nominal PWM of 1140 $[ms]$, that is 14%;
2. Servo PWM command is set to 1650 $[ms]$;
3. A series of step inputs of variable amplitude are feed to the servo as shown in Fig. 6.11;
4. For each test, the input PWM and the potentiometer ADC signal are recorded;

5. ADC signal is converted to angle using (6.6) then the tilt position is calculated from models (6.7) and (6.8);
6. Tilt position signal noise is removed using MAF with 20 samples window;
7. The transfer function is estimated using Matlab® System Identification Toolbox;
8. Test is repeated setting motor PWM to 1350 [*ms*].

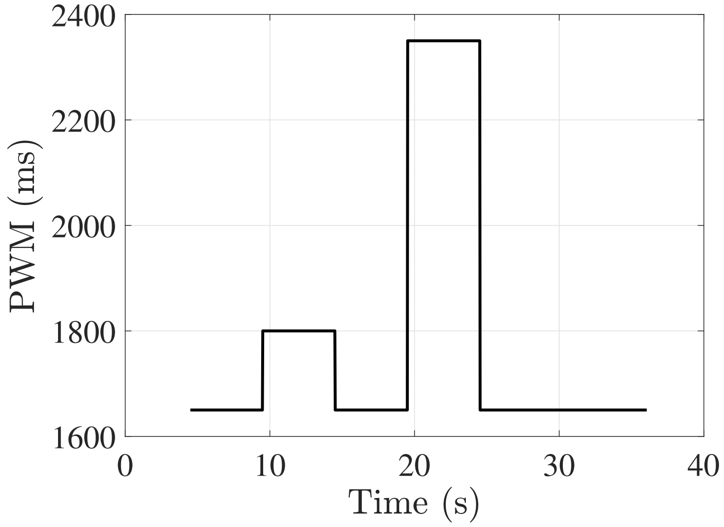

Figure 6.11: Tilt mechanism dynamic test PWM input signal.

As a result, the identified transfer functions for tilt mechanisms 1 and 2 in Laplace domain are:

$$\frac{\Delta\alpha_1(s)}{\Delta \mathrm{PWM}(s)} = \frac{-0.0466}{s^2 + 8.1457s + 28.697} \tag{6.9}$$

$$\frac{\Delta\alpha_2(s)}{\Delta \mathrm{PWM}(s)} = \frac{-0.0621}{s^2 + 8.033 + 28.228} \tag{6.10}$$

with 93.43% and 92.42% fit to estimation data, respectively.

Figure 6.12 illustrates the fitted models (6.9) and (6.10) output and acquired data with the motor operating at 14% and 35%. The results show that it is convenient to make use of a second order transfer function to model the tilt mechanism dynamics. Both models have two underdamped pairs of complex conjugate poles at $s_{1_{1,2}} = -4.02 \pm 3.48i$ and $s_{2_{1,2}} = -4.07 \pm 3.48i$. The two mechanisms responses are very similar, with damping ratios and frequency close to 0.76 and 5.35 $[rad/s]$. Nonetheless, the open-loop gain are not the same, corroborating the fact that the tilts 1 and 2 positions are different for a given PWM input.

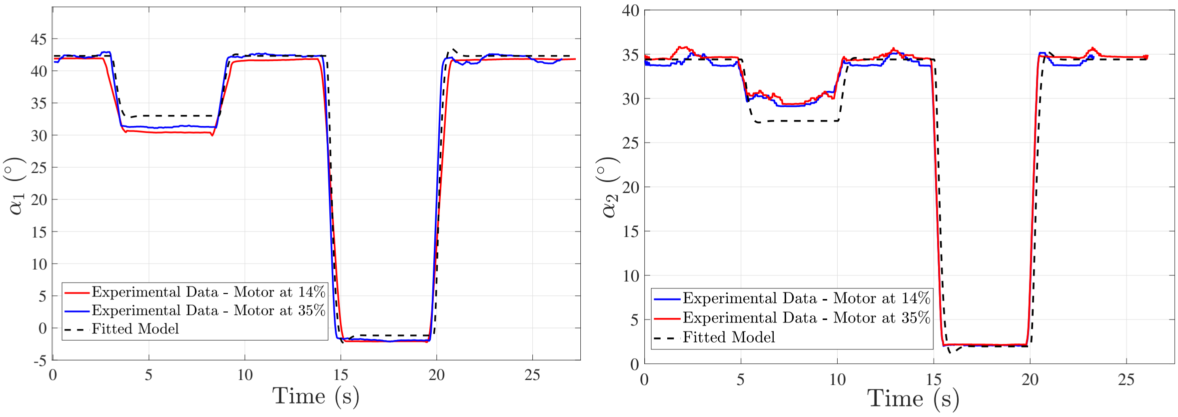

(a) (b)

Figure 6.12: Experimental and model output angle variation for tilt mechanisms 1 (a) and 2 (b).

One may note that in Fig. 6.12, the mechanism open-loop response has minor influence due to the motor steady-state condition. Hence, models (6.9) and (6.10) can be used, independently of the motor operational PWM. However, if the propeller angular speed variation and rate of change of the tilt angles are significant, the gyroscopic effect - described in Eq. (3.12)- may affect the mechanism dynamics. Moreover, from Fig. 6.12 it can be seen that the model does not fit the DC gain for smaller step input (between 5 and 10 $[s]$). This effect can be associated by the assembly play between the servo rod and the motor bed connection.

Unlike the motor dynamic response, shown in Eqs. (6.4) and (6.5), the tilt poles have smaller natural frequency. Henceforth, as will be discussed later, they can exert some influence on the TRBC response and the controller robustness.

6.4 Tilt command effectiveness and joint 1 friction

As previously discussed in Section 5, the test-bench dynamic model fidelity relies on the proper identification of its physical parameters. For instance, in Eqs. (5.41) and (5.42) the terms den_1 and den_2 are directly related to dimension, mass and inertia properties of the system elements. These can be estimated from a CAD model as presented in Table 4.1. However, the estimation accuracy may be limited due to inconsistency between the virtual CAD model and the real apparatus. In addition, the terms μ_1 and μ_2, which represents joints 1 and 2 bearing frictions, are difficult to be calculated from physical principles. As a consequence, a sequence of experimental tests is proposed to identify the test bench physical parameters.

Starting with the TRBC horizontal displacement, expressed in terms of a rotation about joint 1 axis, an specific test procedure is adopted to estimate the bearing joint friction (μ_1) and the tilt command effectiveness ($l_2 f_{1_0}/den_1$). To accomplish this, the following experimental steps were followed:

1. The TRBC is placed at equilibrium position with the motors operating at hover thrust condition f_{1_0};
2. Joints 2 and 4 are locked restricting the TRBC movement only in θ_1 direction;
3. A constant PWM signal is transmitted to the tilt servo positioning the mechanism at a known deflection making the TRBC to accelerate in the deflected direction;
4. The TRBC horizontal velocity ($\dot{\theta}_1$) is recorded;
5. Matlab System Identification toolbox is used to determine the transfer function relation between $\Delta\alpha$ and $\dot{\theta}_1$ in Laplace domain;

6. From the resulting model, bearing joint friction (μ_1) and the tilt command effectiveness ($l_2 f_{1_0}/den_1$) are identified;

7. Experiment is repeated in the opposite direction.

The vehicle response in θ_1 direction due to the step inputs α_1 and α_2 is depicted in Fig. 6.13. In this particular test, the TRBC was subjected to a constant deflection of 10 $[deg]$ (0.1745 $[rad]$) from 0 $[s]$ to 4 $[s]$ as illustrated in Figs. 6.13(a) and 6.13(b). After that, the mechanism was driven to a neutral position (0 $[deg]$). It must be pointed out that, in Figs. 6.13(a) and 6.13(c), the data for $t < 0.33$ $[s]$ were excluded due to the encoder resolution limitation. Herein, the minimum readable angular rate is 0.09 $[rad/s]$ and, consequently, the signal becomes noisy for small velocity variations.

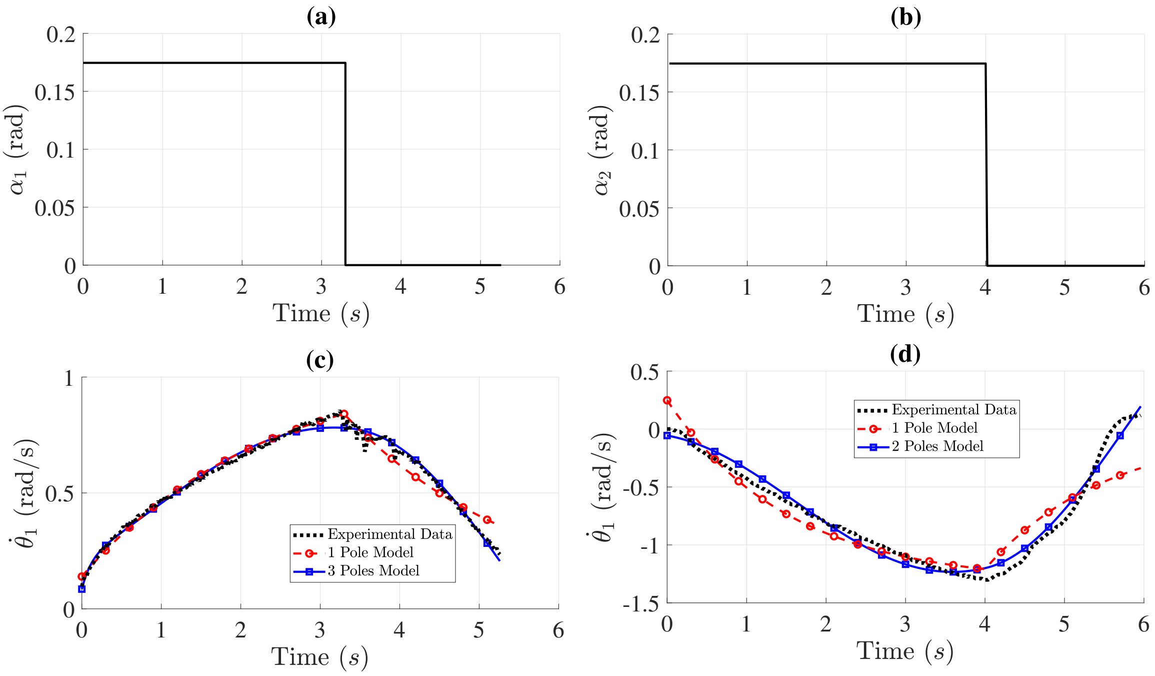

Figure 6.13: TRBC response in θ_1 direction for step input signal in α_1 and α_2.(a) Input signal in α_1. (b) Step input signal in α_2. (c) Vehicle velocity due α_1 deflection. (d) Vehicle velocity due α_2 deflection.

The recorded $\dot{\theta}_1$ is shown in Figs. 6.13(c) and 6.13(d). As can be noted, the vehicle accelerates while the tilt mechanism is deflected. From there on, the velocity is decreased until the system reaches a equilibrium position. This later evidences the presence of dynamic friction in joint 1.

From the collected data, the transfer function models were identified. It is worth mentioning that, by assuming a friction torque as proportional to joint 1 angular velocity, the α to $\dot{\theta}_1$ dynamic can be represented as first order system. In addition, the PWM to α relation, described in Eqs. (6.9) and (6.10), must be accounted for, as long as non-modeled dynamics. Therefore, a higher order transfer function is expected.

In this context, the best transfer function models were analysed. For tilt 1 deflection 1 and 3 poles were employed. Similarly, 1 and 2 poles models were selected for deflection in tilt 2. Figures 6.13(c) and 6.13(d) compares the obtained models. The obtained transfer functions are described by:

$$\frac{\Delta\alpha_1(s)}{\Delta\dot{\theta}_1(s)} = \begin{cases} \frac{3.7782}{s+0.8613} \\ \frac{9.936}{s^3+8.66s^2+0.8724s+3.986} \end{cases} \tag{6.11}$$

for deflection in tilt mechanism 1 and

$$\frac{\Delta\alpha_2(s)}{\Delta\dot{\theta}_1(s)} = \begin{cases} \frac{-4.947}{s+0.6513} \\ \frac{-0.06328}{s^2+0.239s+0.902} \end{cases} \tag{6.12}$$

for tilt mechanism 2, where α is given in $[rad]$.

In order to compare the models accuracy, the fit to estimation data is compared. For tilt 1 deflection, the 1 and 3 poles models have 80.5% and 88.94% fit to estimation data, respectively. For the first, the pole is positioned in the real-imaginary plane in $s1_1 = -0.8613$. Further, for the 3 pole model $s1_{3_1} = -0.862$ and $s1_{3_{2,3}} = -0.0238 \pm 0.68i$. In a similar manner, the 1 and 2 poles models have 60.72% and 84.1% fit to estimation data, respectively, for tilt deflection α_2. In this case the poles are at $s2_1 = -0.6518$ and $s2_{2_{1,2}} = -0.119 \pm 0.942i$. Herein the third order fit to estimation is tolerable based on the usability of the model.

It is worth mentioning that, even though high order models describes the α to $\dot{\theta}_1$ dynamics more precisely, the first order model is preferred. As a consequence, the system parameters are easily identified from Eqs. (6.11) and (6.12). Moreover, the transfer function model can be directly included in Eqs. (5.41) and (5.42) dismissing the estimation of higher order states (e.g. TRBC acceleration) to maintain the system observability. Under those circumstances, the oscillatory modes can be modeled by the tilt mechanism dynamics represented by Eqs. (6.9) and (6.10). These observations are discussed deeply in Chapter 8.

The presented results also evidence that the system response differs from one direction to another. Notably, $s1_1$ and $s2_1$ can be associated with joint 1 friction denoting the vehicle deceleration. Nevertheless, only one value must be adopted for the linear model described in Eq. (5.41). In this case, $\mu_1 = 0.862$ is selected in order to model the effect more conservatively. Moreover, the tilt effectiveness deflection can be identified from the transfer functions numerators. In this instance, $ef_{\alpha 1} = 3.7782$ and $ef_{\alpha 2} = -4.9787$ for tilt mechanisms 1 and 2, respectively.

6.5 θ_4 and θ_1 dynamic relation

For multi-copters in general, the horizontal displacement is directly related with attitude states. More precisely, in the test-bench linear model, this dynamic relation is expressed by means of the term $-l_2 f_{x0}/den_1$ in (5.41). For instance, by assuming a positive motor thrust force variation in motor 1, a positive momentum imbalance is produced in the TRBC CG. Consequently, θ_4 will be positively increased and a negative torque will be produced in θ_1 direction. This torque can be associated with the motors thrust force disbalance.

In order to quantify this phenomena, a second experimental test in θ_1 direction is carried out following the procedures described below:

1. With the motors turned off, the TRBC is driven to a fixed position with the attitude angle different from zero as illustrated in Fig. 6.14;
2. The attitude angle (θ_4) is measured with the aid of the IMU sensor;
3. Motors 1 and 2 PWM are set as the hover thrust force condition f_{x0}. In this step, θ_1 rotation is locked;
4. θ_1 DOF is released and the TRBC is able to move freely in this direction;
5. The TRBC is manually stopped when it reaches a position close to maximum arm rotation. Motors 1 and 2 are turned off;
6. From ENC_1, the TRBC position and velocity are recorded for further analysis;
7. System Identification procedure is employed to estimate the dynamic relation between θ_4 and $\dot{\theta}_1$ in Laplace domain.

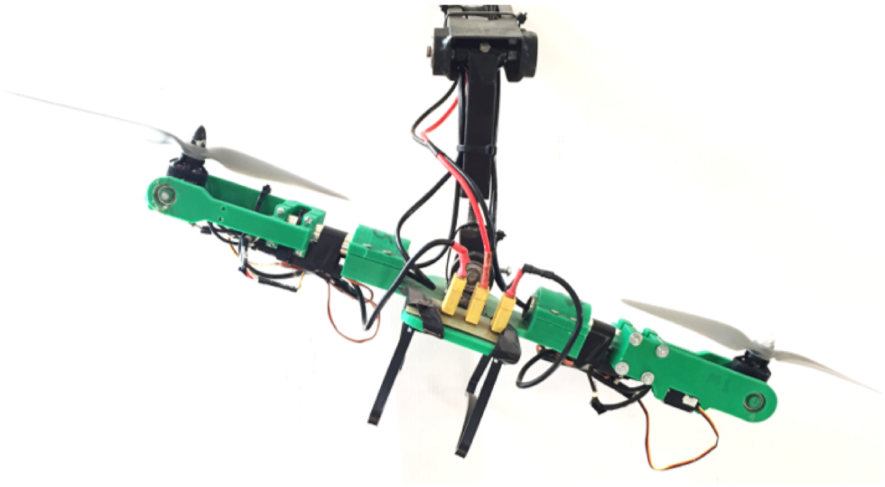

Figure 6.14: Bi-copter positioned at $\theta_4 = -7$ (deg).

From the gathered data one can estimate a transfer function describing the dynamic relation between θ_4 and θ_1. For this particular test, the TRBC is initially positioned at $\theta_1 = -25$ $[deg]$ and $\theta_4 = -7.00$ $[deg]$. Figure 6.15(a) illustrates the vehicle trajectory measured from ENC_1. Additionally, its velocity is shown in Fig. 6.15(b). It must be pointed out that the TRBC is released at $t = 0.08$ $[s]$ and reaches the maximum position at $t = 2.58$ $[s]$. This interval represents the valid experiment duration for system identification. After that the system position is held until the algorithm reaches the number of iterations.

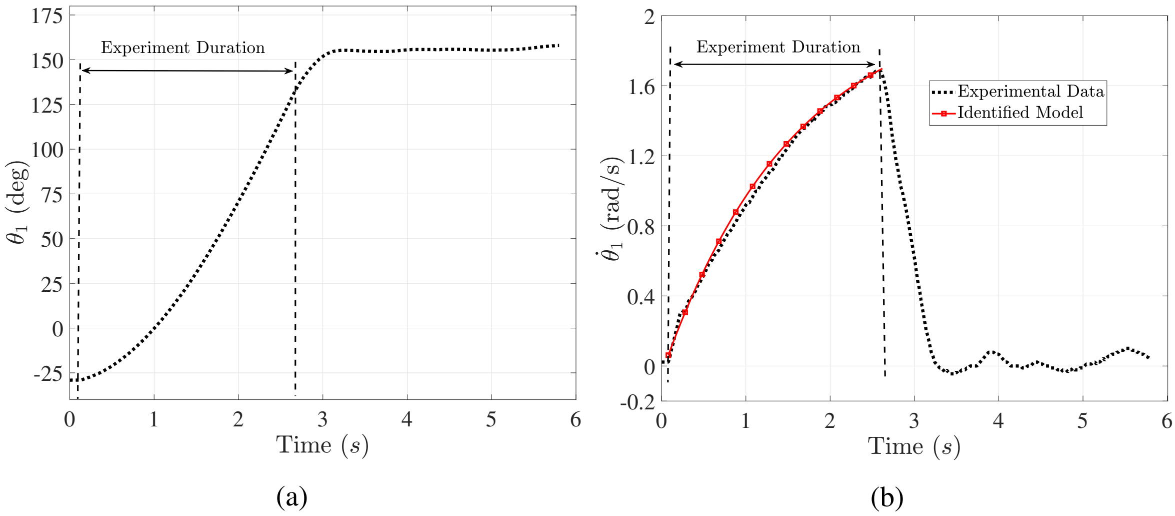

Figure 6.15: θ_4 and θ_1 dynamic relation identification.(a) TRBC position. (b) TRBC velocity.

As can be seen from Fig. 6.15(b), the system response can be characterized as a first order differential equation. Therefore, using Matlab System Identification toolbox, it is possible to fit a model in Laplace domain represented as an one pole transfer function. The identified model response is illustrated in Fig. 6.15(b), whose transfer function can be written as:

$$\frac{\Delta\dot{\theta}_1(s)}{\Delta\theta_4(s)} = \frac{-11.009}{s+0.641} \tag{6.13}$$

where θ_4 and $\dot{\theta}_1$ are given in $[rad]$ and $[rad/s]$, respectively.

The model has presented a fit to estimation data of 93.48%. Even though (6.13) has presented a high accuracy, the results may be susceptible to external interference. For example, the noisy condition of the IMU sensor makes difficult to guarantee that the TRBC is positioned at exactly $\theta_4 = -7.00$ (deg). In this case, the average of the signal was taken to estimate the inclination angle. Despite that, system parameters can be identified in (6.13). First, the θ_4

effectiveness in θ_1 direction, represented by the numerator of (6.13), i.e. $ef_{\theta_4} = l_2 f_{x0}/den_1 = 11.009$. Secondly, the pole $s_{\theta_4} = -0.641$ characterizes the joint 1 friction term μ_1. As can be seen, the obtained value corroborates the identified model in Eq. (6.12).

It is worth mentioning that, due to θ_1 excursion physical limitation, the TRBC velocity not does not reach steady state condition as can be seen in Fig. 6.15(b). Therefore, only part of the transient response is used to estimate the transfer function model.

6.6 Motor command effectiveness and joint 2 friction

As presented in Section 5, the test-bench θ_2 DOF can be assimilated with a multi-copter vertical position. This state is controlled by manipulating the vehicle's net thrust around the equilibrium (hover) condition. In the derived linear system (5.40), the motor effectiveness ($ef_{\theta 2}$), i.e. the acceleration produced in θ_2 direction due to an increment of f_1 and f_2, is expressed by the term l_2/den_2 in (5.42). In the interest of estimating a transfer function model representing the dynamic relation between the motor thrust variation (Δf_1 and Δf_2) and θ_2, the following experimental procedure is proposed:

1. The TRBC is positioned at $\theta_2 = 0$ with θ_1 and θ_4 DOFs locked;
2. Motors 1 and 2 PWMs are set as the hover thrust force condition f_{x0};
3. PWM signal is increased in motors 1 and 2 to achieve a desired thrust force variation;
4. As a constant thrust force perturbation is produced, the TRBC is accelerated until reaches the maximum vertical position of $\theta_{2max} = 38.7\ [deg]$;
5. From ENC_2, the TRBC position and velocity are recorded for further analysis;
6. The Laplace domain transfer function for Δf and $\dot{\theta}_1$ is obtained using System Identification procedure.

The vehicle's position and velocity temporal evolution are depicted in Fig. 6.16. In this case, the thrust force variation was set as $\Delta f_1 = \Delta f_2 = 0.2$ $[N]$. As can be noted, the vehicle velocity and position are increased until it reaches θ_{2max} at, approximately, 2.82 $[s]$. Analogously to the system response in θ_1 direction, the vehicle velocity response in θ_2 direction can be approximated as a first order differential equation. As a result, an one pole Laplace domain transfer function is elected to describe the system dynamics. Under those circumstances, by using the Matlab System Identification toolbox, the identified transfer function is given by:

$$\frac{\Delta\dot{\theta}_2(s)}{\Delta f(s)} = \frac{0.8918}{s+0.2219} \tag{6.14}$$

where $\dot{\theta}_2$ and f are given in $[rad/s]$ and $[N]$, respectively.

Figure 6.16(b) compares the (6.14) temporal evolution with the experimental data for $\Delta f = 0.2$ $[N]$. Given the fact that only the transient response was used for the model identification, (6.14) has presented a fit to estimation data of 90.24%. In (6.14), the numerator is associated with the motor effectiveness, consequently $ef_{\theta 2} = 0.8918$. Moreover, joint 2 friction term can be extracted as $\mu_2 = 0.2219$.

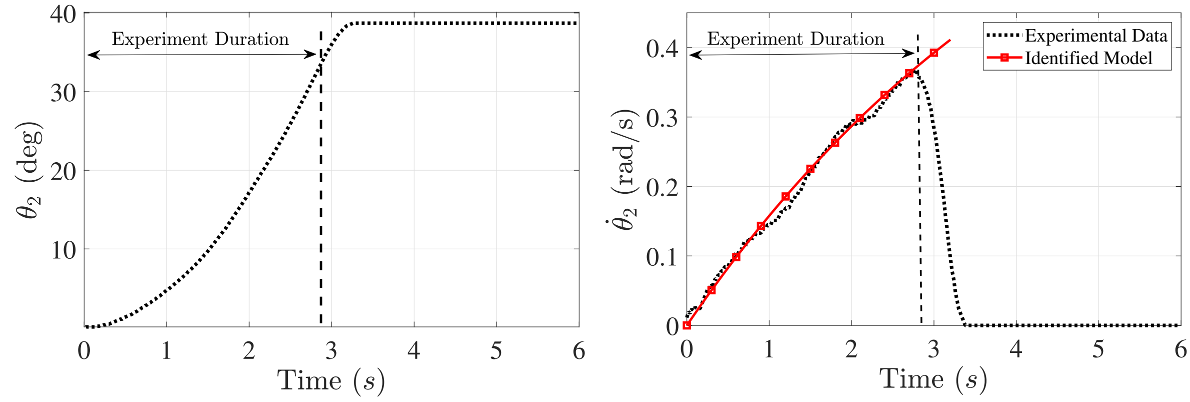

(a) (b)

Figure 6.16: Motor effectiveness in θ_2 direction effectiveness.(a) TRBC position. (b) TRBC velocity.

6.7 Model Parameters

The identification experiments carried out in this chapter has shown that the test-bench physical properties estimated from a virtual model are susceptible to certain degree of uncertainty. In order to illustrate that, a comparison between the identified model parameters and those calculated from the CAD model are presented in Table 6.1.

Table 6.1: Test-Bench Model Parameters.

Parameter	**Description**	**Calculated**	**Identified**
$\frac{l_2 f_{x0}}{den_1}$	θ_4 to θ_1 dynamic relation	13.3862	11.009
$\frac{l_2 f_{y0}}{den_2}$	θ_4 to θ_2 dynamic relation	0.0	0.0
$\frac{\mu_4}{I_{zz4}}$	joint 4 friction term	0.0	37.0321
$\frac{c}{I_{zz4}}$	joint 4 to TRBC CG distance	2.4492	2.6471
$\frac{l_2 f_{1_0}}{den_1}$	tilt 1 effectiveness	2.5543	3.7782
$\frac{l_2 f_{2_0}}{den_1}$	tilt 2 effectiveness	2.5543	4.9787
$\frac{l_2}{den_2}$	motor thrust force effectiveness in θ_2 direction	0.7626	0.8918
$\frac{L_1}{I_{zz4}}$	motor 1 torque effectiveness w.r.t θ_4	17.3077	12.0321
$\frac{L_2}{I_{zz4}}$	motor 2 torque effectiveness w.r.t θ_4	17.3077	12.0321
μ_1	joint 1 friction term	0.0	0.862
μ_2	joint 2 friction term	0.0	0.2219

As can be noted, the major discrepancy is associated with the fact that the friction terms can only be estimated with proper identification procedure. Additionally, it is noteworthy that the calculated tilt effectiveness are symmetric for tilt 1 and 2. Nevertheless, the identification has shown that there is a dissimilarity between the mechanism dynamics and, principally, their effectiveness. As a consequence, the TRBC horizontal response will not be the same from one direction to another. This behavior is attributed to the apparatus assembly which can have some degree of misalignment. Since model parameters uncertainty has a significant influence over control stability, this subject will be later discussed focusing on control applications.

6.8 Chapter Summary

- Even tough the TRBC test-bench dimension, mass and inertia properties can be used to estimate its dynamic model, system identification procedures can be employed to increase the coefficients accuracy.

- The actuators - motors and tilt mechanisms - responses have to be identified properly so that their influence over the system dynamics can be evaluated.

- Independent experimental approaches were adopted to estimate the system response in θ_4, θ_1 and θ_2 directions. The results have shown that:

    1. The TRBC response in θ_4 direction can be approximated by a pendulum. Motors 1 and 2 thrust disbalance contributes to the net torque in joint 4. The distance between the joint position and the vehicle CG must be accounted.
    2. In θ_1 direction, the vehicle displacement is a consequence of two main effects: the tilt deflection and the decomposition of the net thrust force in θ_1 direction due to the attitude variation (θ_4). For both, the response can be approximated by a first order transfer function. However, the tilt dynamics must be accounted for the first.
    3. For the vertical displacement, θ_2 to thrust relation is represented by a first order transfer function.

- As shown in Table 6.1, the calculated parameters differs from the identified coefficients evidencing that the model contains uncertainties. Moreover, the friction terms could only be modeled through system identification procedures.

- Equations (6.11) and (6.12) indicate that the system response in θ_1 is different from one direction to the other. This evidence has a significant influence over the system response, specially if model based control applications is considered.

CHAPTER VII

Modern Control

Designing a multi-copter MAV can be a challenging task since it requires knowledge in different engineering areas. One of the main steps during the project development is the design of a closed-loop controller since these vehicles have an open-loop unstable dynamics. In fact, position and attitude control of MAVs has been widely investigated in the literature by means of several control techniques either for stabilization or trajectory tracking problems (BOUABDALLAH et al., 2004; LEE et al., 2009; SMEUR et al., 2018).

Notwithstanding, for some applications, the multi-copter may perform some specific tasks that could restrict its operational domain. For instance, for indoor inspections, surveillance, and risky cargo transportation. In such cases the attitude, velocity and actuation commands must be constrained to ensure mission safety. Furthermore, the inclusion of the tilt mechanism in a MAV design shall take into account the device mechanical limitations and also the dynamical interference, from the control perspective, in the vehicle response.

Starting from the TRBC dynamics derived in Chapters 5 and 6, this chapter goal is to design a proper controller to: guarantee system stability, track a desired reference trajectory. In order to accomplish this, an optimal control design approach is proposed. In particular, a

Linear Quadratic Regulator (LQR) based control architecture, which includes integral error control is particularized for the TRBC problem. This early approach aims to gather preliminary experimental results to further understand the system behavior. Moreover, it can be used to validate the test-bench dynamic model derived in Sections 5 and 6.

7.1 Principle of optimality

LQR and MPC controllers are centered in the choice of optimal inputs via a cost function minimization problem. Since both rely on optimal control theory, the principle of optimality will be briefly discussed by control application perspective.

Optimal control problems arise in designing a controller which minimizes a performance index (LAVRETSKY; WISE, 2013). In general, optimal controllers are based on state-space time-domain models. Therefore, one of the main design challenges is to translate frequency domain performance and stability requirements from classical control to the desired control task since the control gain tuning is directly related to these elements. So forth, its theoretical key point is to develop a method to tune the design parameters to achieve the desired performance and stability criteria.

How optimal control regulator problems are posed and their relation with the performance index minimization problem can be better understood by studying the Hamilton–Jacobi –Bellman (HJB) partial differential equation. For further details concerning the HJB equations one may refer to Kwakernaak & Sivan (1972) and Athans & Falb (2006). Taking into account the HJB principle, a synthesis of optimality is introduced.

Consider a dynamic system, LTI represented as

$$\begin{aligned} \dot{\mathbf{x}} &= \mathbf{A}_c\mathbf{x} + \mathbf{B}_c\mathbf{u} \\ \mathbf{y} &= \mathbf{C_c}\mathbf{x} + \mathbf{D_c}\mathbf{u} \end{aligned} \tag{7.1}$$

where $\mathbf{A}_c \in \mathbb{R}^{n_s \times n_s}$, $\mathbf{B}_c \in \mathbb{R}^{n_s \times n_u}$, $\mathbf{C}_c \in \mathbb{R}^{n_y \times n_s}$ and $\mathbf{D}_c \in \mathbb{R}^{n_y \times n_u}$ being n_s, n_u and n_y the number of states, input commands and output variables, respectively. Moreover, Eq. (7.1) can be written in discrete time domain by applying the ZOH method analogously to (5.43) as

$$\begin{aligned} \mathbf{x}(k+1) &= \bar{\mathbf{A}}\mathbf{x}(k) + \bar{\mathbf{B}}\mathbf{u}(k) \\ \mathbf{y}(k) &= \bar{\mathbf{C}}\mathbf{x}(k) + \bar{\mathbf{D}}\mathbf{u}(k) \end{aligned} \tag{7.2}$$

the notion of optimality is defined through a integral cost performance index

$$J = \int_{t_0}^{t_f} L(\mathbf{x}(\tau), \mathbf{u}(\tau)) d\tau + S(\mathbf{x}(t_f)) \tag{7.3}$$

evaluated along the system trajectories $\mathbf{x}$ due to applied control input $\mathbf{u}$. The instant cost $L(\mathbf{x}(\tau), \mathbf{u}(\tau)))$ and the terminal cost $S(\mathbf{x}(t_f))$ are defined as scalar non-negative functions of their arguments.

Therefore, the control task is to find an optimal control policy $\mathbf{u}^\star$ to minimize the cost index J over the time interval $[t_0, t_f]$. One can show that, by dividing the integral into time intervals and, then, for each of them, choose an optimal control the overall cost so that J can be minimized. This argument leads to the Principle of Optimality (BELLMAN, 2003).

Principle of Optimality. *An optimal policy has the property that whatever the initial state and initial decision are, the remaining decisions must constitute an optimal policy with regard to the state resulting from the first decision*

In other words, based on this principle, for a given an initial state, there is enough condition to find a sequence of an optimal control solution $\mathbf{u}^\star$, that minimizes (7.3) over the time interval $[t_0, t_f]$.

if an optimal (minimum) cost J can be found and $\mathbf{u}^\star$ calculated, then the latter constitutes the optimal policy for the dynamic system w.r.t the cost index (7.3).

7.2 Linear Quadratic Regulator

In terms of optimal control techniques, the Linear Quadratic Regulator (LQR) is one of the most popular design methods. This approach can bring several advantages as: good performance, robustness and control effort minimization (LAVRETSKY; WISE, 2013). In summary, the LQR control law is based on an LTI state-space system and provides an optimal control law that satisfies a performance index condition.

7.2.1 Quadratic performance index

The choice of the performance index depends upon the nature of the control problem. By considering discrete LTI state-space system (7.2), it is appropriate to adopt a quadratic performance index as

$$J = \sum_{k=0}^{N_\infty - 1} \left[\mathbf{x}^T(k)\mathbf{Q}_k\mathbf{x}(k) + \mathbf{u}^T(k)\mathbf{R}_k\mathbf{u}(k)) \right] \tag{7.4}$$

being $\mathbf{Q}_k \succ 0$ and $\mathbf{R}_k \succ 0$ the state and control weighting matrices and N_∞ the number of iterations.

One may note that Eq. (7.4) assumes a performance index for an infinite time minimization problem as $(N_\infty - 1) \to \infty$. As a consequence, the terminal condition $S(\mathbf{x}(t_f))$ is zero if the closed loop system is asymptotically stable.

Generally speaking, there are three main reasons for the choice of a quadratic performance index. They are:

- the quadratic function is always non-negative on its domain;
- the energy associated to the system response and the input demand becomes more ap-

parent;

- there are well known solutions for this type of function in the literature such as the Riccati equations.

Therefore, assuming the cost function (7.4), one can write the LQR Hamiltonian as

$$H = \mathbf{x}^T(k)\mathbf{Q}_k\mathbf{x}(k) + \mathbf{u}^T(k)\mathbf{R}_k\mathbf{u}(k)) + \frac{\partial J^\star}{\partial \mathbf{x}}(\mathbf{A}\mathbf{x}(k) + \mathbf{B}\mathbf{u}(k)) \tag{7.5}$$

By assuming smoothness of all functions, it follows that minimizing H w.r.t. the control $\mathbf{u}$ one must say that every component of the Hamiltonian's gradient ∇H_u must vanish at the point of optimum, i.e. $\nabla H_u = 0$. Hence, taking the gradient of H w.r.t $\mathbf{u}$ produces

$$\frac{\partial H}{\partial \mathbf{u}} = 2\mathbf{R}_k\mathbf{u}(k) + \mathbf{B}^T\nabla_x J^\star = 0 \tag{7.6}$$

where the optimal control is

$$\mathbf{u}^\star(k) = -\frac{1}{2}\mathbf{R}_k^{-1}\mathbf{B}^T\nabla_x J^\star \tag{7.7}$$

Further, one can show that the optimal cost is a quadratic time-varying function of the system state (KWAKERNAAK; SIVAN, 1972). Thus,

$$J^\star = \mathbf{x}(k)^T\mathbf{P}\mathbf{x}(k) \tag{7.8}$$

where $\mathbf{P} \succ 0$. Therefore,

$$\frac{\partial J^\star}{\partial t} = \mathbf{x}(k)^T \dot{\mathbf{P}} \mathbf{x}(k) \tag{7.9}$$

$$\nabla_x J^\star = 2\mathbf{P}\mathbf{x}(k) \tag{7.10}$$

Substituting (7.7) in (7.5), taking the time derivative and, then, substituting (7.9) and (7.10), one get

$$\mathbf{x}(k)^T \left[-\dot{\mathbf{P}} - \mathbf{P}\mathbf{A} + \mathbf{A}^T\mathbf{P} - \mathbf{Q}_k - \mathbf{P}\mathbf{B}\mathbf{R}_k^{-1}\mathbf{B}^T\mathbf{P}\right] \mathbf{x} = 0 \tag{7.11}$$

with the boundary condition $\mathbf{P}(N_\infty - 1) = Q_{(N_\infty - 1)}$. Therefore, the following final value problem must be true

$$\dot{\mathbf{P}} = -\mathbf{P}\mathbf{A} - \mathbf{A}^T\mathbf{P} + \mathbf{Q}_k + \mathbf{P}\mathbf{B}\mathbf{R}_k^{-1}\mathbf{B}^T\mathbf{P} \tag{7.12}$$

The time-varying matrix ordinary equation (7.12) is known as Riccati equation. Further, substituting (7.9) and (7.10) into (7.7), an optimal control policy can be written as

$$\mathbf{u}_{lqr}(k) = \mathbf{R}_k^{-1}\mathbf{B}^T\mathbf{P}\mathbf{x} = -\mathbf{K}\mathbf{x} \tag{7.13}$$

where $\mathbf{K} \in \mathbb{R}^{(n_u) \times n_s}$ is a constant matrix gain containing all the LQR optimal feedback gains.

It worth mentioning that the weighting matrices $\mathbf{Q}_k$ and $\mathbf{R}_k$ are chosen so that the eigenvalues of a generic $\mathbf{M}$ matrix are positive and the quadratic form $\mathbf{x}^T\mathbf{M}\mathbf{x}$ are also positive for every value of $\mathbf{x}$; hence, the performance index J is always positive.

Moreover, since the solution choice of an optimum control law is posed as a minimization problem, the choice of relative magnitudes of $\mathbf{Q}_k$ and $\mathbf{R}_k$ matrices becomes a trade-off relation. For instance, a larger control-weighting matrix $\mathbf{R}_k$ will make it necessary for $\mathbf{u}(k)$ to be smaller to ensure that $\sqrt{\mathbf{R}_k}\mathbf{u}(k)$ is close to zero. Thus, the matrix $\mathbf{R}_k$ penalizes the controls efforts. On other hand, in order to drive the states $\mathbf{x}(k)$ to zero quickly, a larger magnitude of $\mathbf{Q}_k$ may be selected. As a consequence, the choices of $\mathbf{Q}_k$ and $\mathbf{R}_k$, weights the effects of state on control variables magnitudes, affecting the position of the closed-loop poles and, consequently, the dynamical behavior of the system.

Finally, assuming the feedback control law stated in Eq. (7.13), the closed loop state space system can be written as

$$\mathbf{x}(k+1) = (\mathbf{A}-\mathbf{B}\mathbf{K})\mathbf{x}(k) = \bar{\mathbf{A}}\mathbf{x}(k) \tag{7.14}$$

where $\bar{\mathbf{A}}$ is the closed-loop matrix with the eigenvalues inside a unitary circle. In particular, state feedback is assumed for the posed problem. If this condition is not satisfied, a state estimator can be employed.

It is worth mentioning that the control law (7.14) represents a regulation control problem. For that reason, the LQR control law results in a type 0 control system (LAVRETSKY; WISE, 2013). In this case, the control task is to bring all the system states to equilibrium given an initial perturbed condition. Additionally, the performance index function is minimized giving optimal properties to the calculated input $\mathbf{u}^\star$. Consequently, $\mathbf{x}(k) \to 0$ as $k \to \infty$, which implies that $\mathbf{u}(k) \to 0$ as $k \to \infty$.

7.2.2 Attitude Regulation Experiments

Aiming to validate the technique presented in this section, the LQR controller was implemented and experimented in the TRBC test-bench. The control task consists of regulating the vehicle attitude (θ_4 and $\dot{\theta}_4$), when subjected to an angular initial condition. In this case, θ_2 and θ_1 DOF are maintained fixed. Additionally, only motors 1 and 2 thrust force are used as control variables. It implies that the tilt mechanisms are positioned vertically, i.e. $\alpha_1 = \alpha_2 = 0$.

In order to design the controller, the attitude model is extracted from Eqs. (5.40). Then, the model is written in discrete time domain applying the ZOH with $T_s = 0.02$ $[s]$. The choice of the sample time was based on the performance of the micro-controller which is related to the time required run the operation routine in a sample.

The control gain matrix is calculated solving Eq. (7.12). In this case, the choice of the weighting matrices was based on two criteria. First, to select $\mathbf{Q}_k$ and $\mathbf{R}_k$ which gives feasible solution to the Riccati equation. Second, to select proper gains that give adequate responses in simulations and experiments. Therefore, for this particular experiment, the first tuning choice was to select $\mathbf{Q}_k = diag([1\ 1])$ and $\mathbf{R}_k = diag([1\ 1])$ and vary the parameters manually until a proper response is achieved. Then, adopting the gain matrices $\mathbf{Q}_k = diag([1.6\ 0.3])$ and $\mathbf{R}_k = diag([0.2\ 0.2])$ resulting in

$$\mathbf{K} = \begin{bmatrix} 0.5418 & 0.6548 \\ -0.5418 & -0.6548 \end{bmatrix} \tag{7.15}$$

It must be pointed out that, in this case, it is desired that the angular velocity gains are smaller than the position since its signal has higher noise level. Furthermore, the closed loop rise time is directly related with the input weights in $\mathbf{R}_k$

Consequently, the system poles, in Z-domain, are relocated from $s_{1,2} = 0.967 \pm 0.115i$ to $s_1 = 0.938$ and $s_2 = 0.688$. Therefore, the system becomes overdamped and a non-oscillatory response is expected. Figure 7.1 compares the TRBC response with LQR and no controller when the vehicle is brought to an angular position of $\theta_4 = 7$ $[deg]$. As can be seen, the TRBC response with the LQR controller has presented lower oscillations in θ_4 specially when $t < 2$ $[s]$. It may be noted that, in both scenarios, the system is brought to a stability condition of approximately $\theta_4 = -5$ $[deg]$ where $\dot{\theta}_4$ is nearly 0 $[deg/s]$. This condition indicates that either the IMU is inclined with respect to the TRBC structure or there is a disbalance between the two motor arms. In any case, one can assume that -5 $[deg]$ is relatively small to jeopardize the system performance. Moreover, it should be stressed the LQR robustness under the presence of sensor noise and model uncertainties. Under those circumstances, the controller was able to drive the system to stability with minimal control effort as depicted in Fig. 7.2.

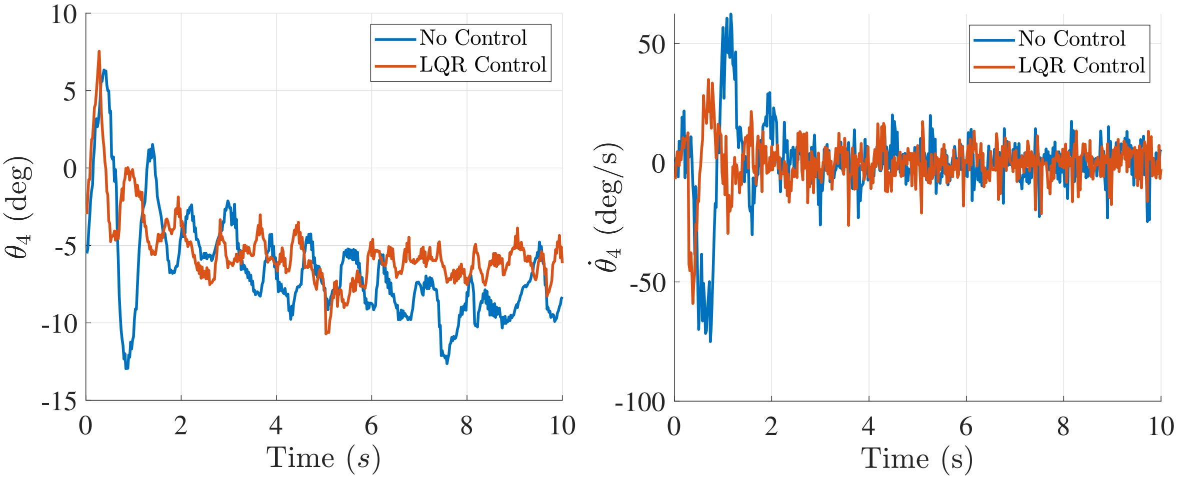

Figure 7.1: Attitude regulation using LQR controller.

7.3 Linear Quadratic Tracking Controller

As previously discussed, since (7.14) is classified as a type 0 closed loop system, it may present some particularities concerning its dynamic response. Primarily, if the controller is fed with an input tracking command, the system may be driven to an equilibrium condition with non-zero steady state error. Therefore, in order to achieve good tracking performance, an

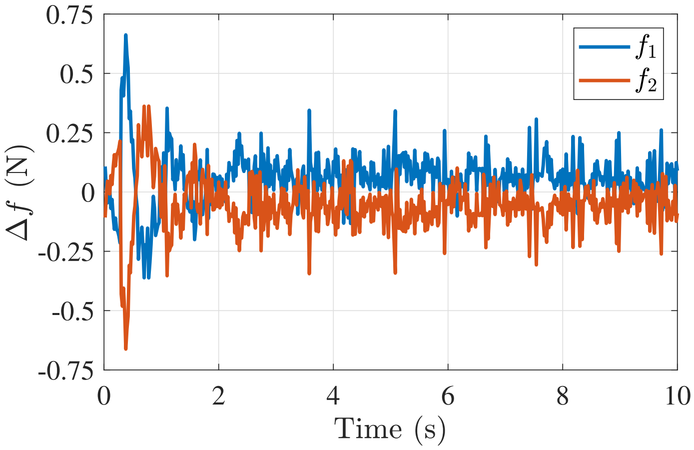

Figure 7.2: Motors 1 and 2 thrust force variation.

integral error control action must be added in the control loop. Following this approach, it is possible to augment the system type number according to the reference signal mathematical model. This strategy is commonly referred in the literature as the *Internal Model Principle* (FRANCIS; WONHAM, 1976).

7.3.1 Servomechanism Design Model

Augmenting controller with integral action can be translated in including a model of the class of signals to be tracked in the system dynamics. In this sense, Davidson & Goldenberg (1975) proposes a systematic process for building an augmented state space model known as the *Servomechanism Design Model*.

Servomechanism Design Model: *Necessary and sufficient conditions can obtained for the existence of a solution to the robust servomechanism problem, so that asymptotic tracking, in the presence of either measurable or unmeasurable disturbances, occurs for all plant parameter variations. Any robust controller must consist of two separate devices: (i) a servo-compensator, which is quite distinct from an observer and which corresponds to a generalization of the integral controller in classical control theory, (ii) a stabilizing compensator, whose sole purpose is to stabilize the augmented system obtained when the servo-compensator is con-*

nected to the plant. The servocompensator consists of n_x*, where* n_x *is the number of outputs to be regulated, unstable compensators with identical dynamics, corresponding to the class of disturbance-reference-inputs, connected via feedback, to the error outputs of the plant. This servo-compensator structure is an essential feature of any robust controller.*

Based on the definition, the controller design steps can be presented. Let a state-space model be considered as presented in Eqs. (7.1). Then, a subset of the output vector **y** is selected as the desired variables ($\mathbf{y}_c \in \mathbb{R}^{n_c}$) to track a reference input vector $\mathbf{r} \in \mathbb{R}^{n_r}$, with $n_c \geq n_r$, which can be expressed as a set differential equations. As a result, the tracking error signal can be defined as

$$\mathbf{e} = \mathbf{y}_c - \mathbf{r} \tag{7.16}$$

In (7.16) **e** is defined in order to apply negative feedback of the error and their derivatives. One may note that, tracking $\mathbf{y}_c$ is the same as applying a regulator in **e**. Henceforth, the control objective is to make $\mathbf{e} \to 0$ or $\mathbf{y}_c \to \mathbf{r}$ as $t \to \infty$. Moreover, each reference input r can be expressed as a p^{th} order differential equation as follows:

$$\overset{(p)}{r} = \sum_{i=1}^{p} a_i \overset{(p-i)}{r} \tag{7.17}$$

Given that the servomechanism design model is created by defining a new state space model containing the error dynamics and the first time derivatives of the original model (7.1). Therefore, an augmented state space model can be defined as (LAVRETSKY; WISE, 2013):

$$\dot{\mathbf{z}} = \begin{bmatrix} \dot{\mathbf{e}} \\ \ddot{\mathbf{e}} \\ \vdots \\ \overset{(p)}{e} \\ \overset{(p+1)}{x} \end{bmatrix} = \underbrace{\begin{bmatrix} \mathbf{O} & \mathbf{I} & \mathbf{O} & \dots & \mathbf{O} & \mathbf{O} \\ \mathbf{O} & \mathbf{O} & \mathbf{I} & \dots & \mathbf{O} & \mathbf{O} \\ & & \ddots & & & \\ a_p\mathbf{I} & a_{p-1}\mathbf{I} & \dots & a_2\mathbf{I} & a_1\mathbf{I} & \mathbf{C}_c \\ \mathbf{O} & \dots & \dots & \dots & \mathbf{O} & \mathbf{A}_c \end{bmatrix}}_{\tilde{\mathbf{A}}} \begin{bmatrix} \mathbf{e} \\ \dot{\mathbf{e}} \\ \vdots \\ \overset{(p-1)}{e} \\ \overset{(p)}{x} \end{bmatrix} + \underbrace{\begin{bmatrix} \mathbf{O} \\ \mathbf{O} \\ \vdots \\ \mathbf{D}_c \\ \mathbf{B}_c \end{bmatrix}}_{\tilde{\mathbf{B}}} \underbrace{\begin{bmatrix} \mathbf{O} \\ \mathbf{O} \\ \vdots \\ \mathbf{O} \\ \dot{\mathbf{u}} \end{bmatrix}}_{\tilde{\mathbf{u}}} \tag{7.18}$$

being $\mathbf{O}$ and $\mathbf{I}$ zero and identity matrices, respectively, with proper dimensions. In addition, $\mathbf{z} \in \mathbb{R}^{(n_s+p\cdot n_r)}$ and $\tilde{\mathbf{u}} \in \mathbb{R}^{(n_u+p\cdot n_r)}$ represent the augmented state and input vectors.

Now, by assuming a feedback control law as in (7.7), the optimal control input $\tilde{\mathbf{u}}$ can be expressed as

$$\tilde{\mathbf{u}} = -\mathbf{K}_c\mathbf{z} = -\begin{bmatrix}\mathbf{K}_p \; \mathbf{K}_{p-1} \; \dots \; \mathbf{K}_1 \; \mathbf{K}_x\end{bmatrix}\mathbf{z} \tag{7.19}$$

In (7.19), the feedback gain $\mathbf{K}_c$ is calculated solving the Riccati equation (7.12). The resulting matrix can be partitioned following the definition of vector $\mathbf{z}$. As a result, $\mathbf{K}_p \dots \mathbf{K}_1$ are associated with the integral error control, responsible for tracking a desired reference signal $\mathbf{r}$ with zero steady state error. Additionally, $\mathbf{K}_x$ is the system's regulation matrix, which guarantees that all the states are driven to stability when $t \to \infty$. The servomechanism model block diagram is illustrated in Fig.7.3 .

It must be emphasized that, even tough the presented control formulation was derived in continuous time domain, the discrete time domain gain matrix $\tilde{\mathbf{K}}_c$ can be obtained applying the ZOH in (7.18) and solving the discrete Riccati equation problem.

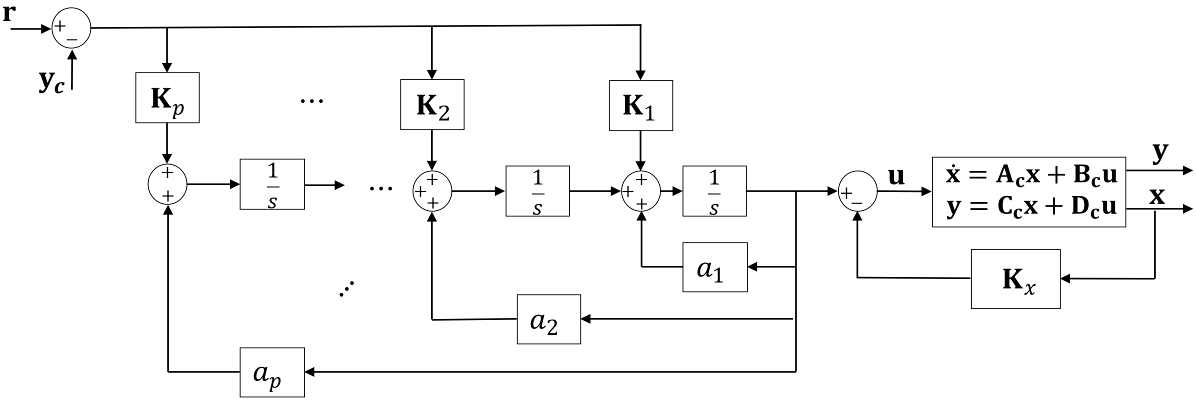

Figure 7.3: Servomechanism model block diagram.

7.3.2 Particularizing the LQT problem to TRBC control

The servomechanism design model formulation, presented previously, can be particularized to the TRBC to track desired positions on θ_1 and θ_2 directions. For the controller design, the TRBC linear state-space model, described in Eq. (5.40), can be used. Therefore, one can assume that $\mathbf{x} = \chi$, $\mathbf{u} = \upsilon$, $\mathbf{A}_c = \mathbf{A_{TB}}$ and $\mathbf{B}_c = \mathbf{B_{TB}}$ in (7.1).

In particular, for the test bench control task, one can assume that a constant (step) reference position is desired for θ_1 and θ_2 DOF, i.e. $\mathbf{y}_c = [\theta_1\ \theta_2]^T$ and $\mathbf{r} = [\theta_{1ref}\ \theta_{2ref}]^T$. Therefore,

$$\mathbf{C}_c = \begin{bmatrix} 1 & 0 & 0 & 0 & 0 & 0 \\ 0 & 1 & 0 & 0 & 0 & 0 \end{bmatrix} \tag{7.20}$$

In addition, the reference tracking signal can be described as a first order derivative function with $p = 1$ and $a_1 = 0$ in (7.17) yielding $\dot{\mathbf{r}} = 0$. As a result, matrix $\mathbf{K}_c = [\mathbf{K}_1\ \mathbf{K}_x]$ in (7.19) is obtained solving the Riccati equation problem. Figure 7.4 illustrates the TRBC tracking controller control loop using the servomechanism design procedure. The control performance can be evaluated through simulations and/or experiments as discussed subsequently.

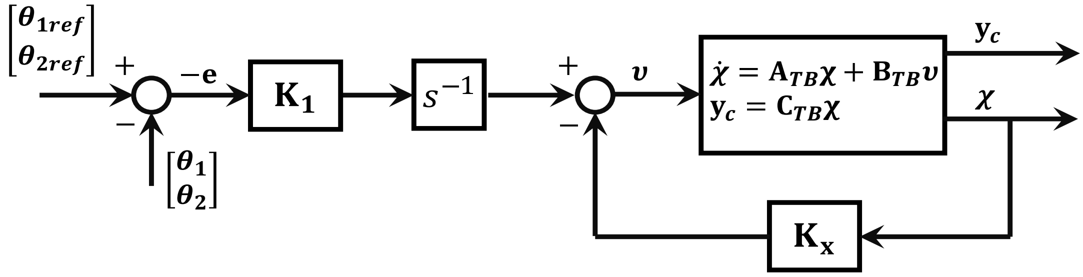

Figure 7.4: Test-bench tracking controller.

7.3.3 LQT Controller Experiments

At this point, the LQT control technique will be employed with three main objectives. First, to validate the LQT control technique presented in this section. Second, to compare the experimental and simulation results. Finally, to examine the TRBC performance when endowed or not with a tilt mechanism.

For all the study cases, the control task consists of tracking a step input in θ_1 and θ_2 directions as illustrated in Fig. 7.5. As a result, $\mathbf{r} = [0\ 18.7]^T$ $[deg]$ for $0 \leq t \leq 10$ $[s]$ and $\mathbf{r} = [10\ 18.7]^T$ $[deg]$ for $t > 10$ $[s]$.

It is worth mentioning that the controllers were designed using model (5.40) considering the calculated parameters described in Table 6.1. Then, the model is written in discrete domain assuming a sampling time of $T_s = 0.02$ $[s]$. In order to calculate the gain matrices solving the Riccati equation, the weighting matrices were chosen as $\mathbf{Q}_k = diag([0.1\ 0.8\ 0.3\ 0.08\ 0.5\ 0.1\ 0.3\ 0.2])$ and $\mathbf{R}_k = diag([1\ 1])$ for fixed rotor configuration or $\mathbf{R}_k = diag([1\ 1\ 0.2\ 0.2])$ for tilt rotor configuration. The idea is to assume similar design parameters and control architecture to compare the system response. Moreover, the values of the weighting matrices were manually selected departing from $\mathbf{Q}_k = \mathbf{1}_{n_s \times n_s}$ and $\mathbf{R}_k = \mathbf{1}_{n_u \times n_u}$ until a proper performance is achieved in simulations and experimentally.

- **TRBC Tracking Controller with Fixed Rotors**

For this initial experiment, the TRBC tracking command response is examined considering fixed rotor configuration, i.e. $\alpha_1 = \alpha_2 = 0$. In this case, the resulting gain matrices

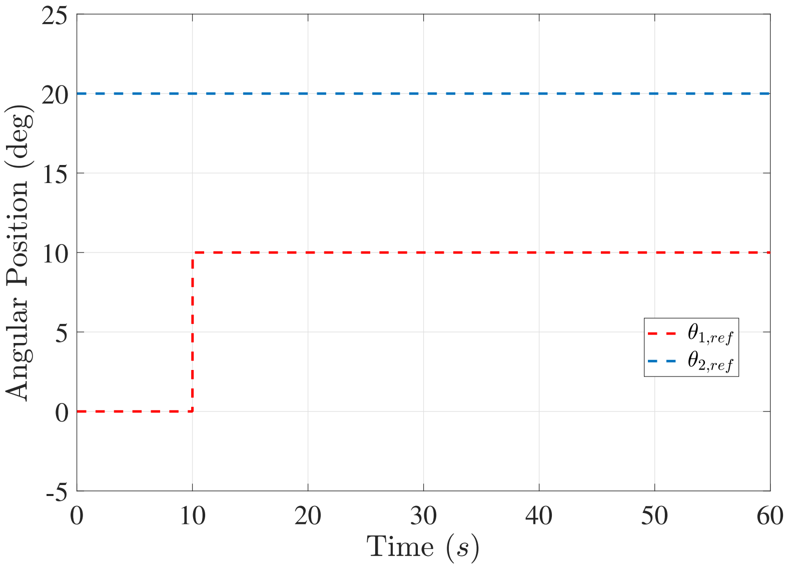

Figure 7.5: LQT controller reference positions.

are:

$$\mathbf{K}_x = \begin{bmatrix} -0.77036 & 1.3142 & 0.55768 & -1.1145 & 1.3635 & 0.27847 \\ 0.77036 & 1.3142 & -0.55768 & 1.1145 & 1.3635 & -0.27847 \end{bmatrix}$$

$$\mathbf{K}_1 = \begin{bmatrix} -0.20801 & 0.61929 \\ 0.20801 & 0.61929 \end{bmatrix}$$

Figure 7.6 compares the simulated states temporal evolution with the experimental measurements. As can be seen in Fig. 7.6(a) and 7.6(c), in both scenarios, the system was able to reach the desired reference positions. Even though the real and virtual systems have similar dynamic behavior, some discrepancies can be pointed out.

For instance, in θ_2 direction, which represents the vehicle altitude, the system presents an underdamped and overdamped responses, for the virtual and real experiments, respectively,

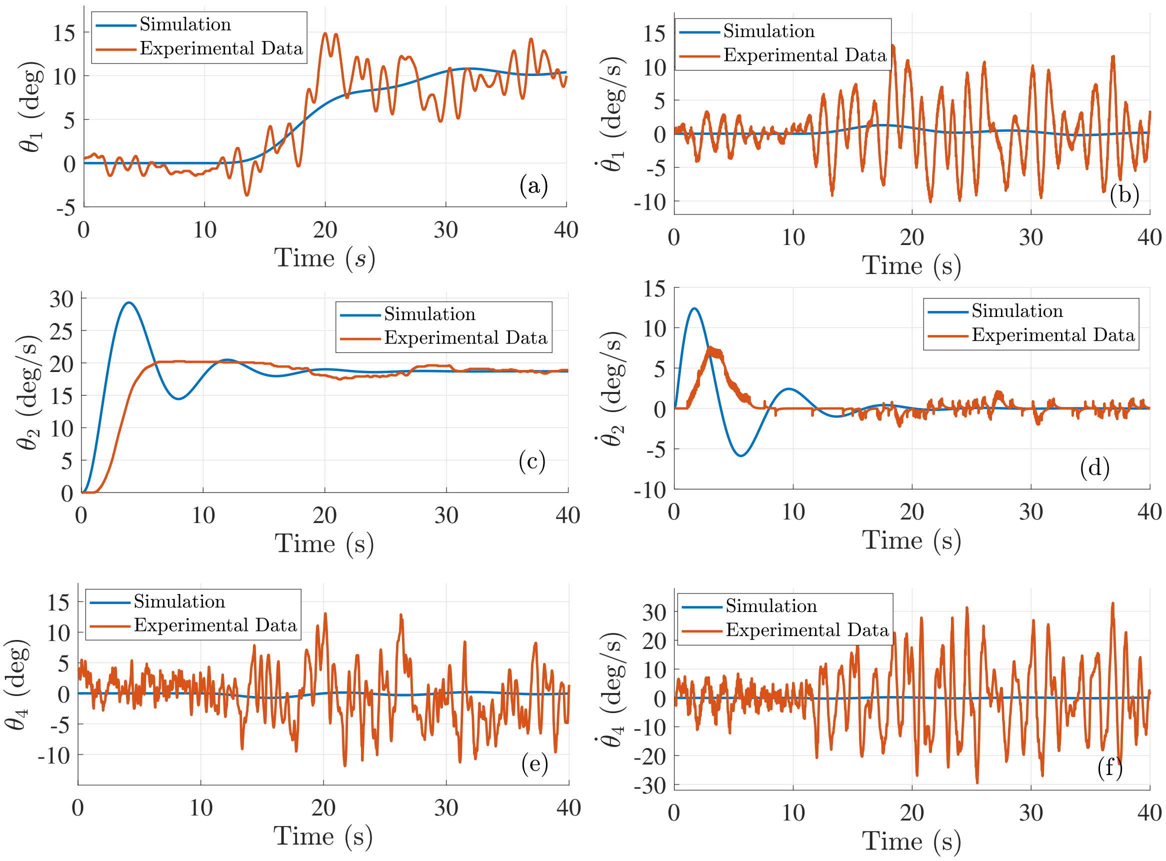

Figure 7.6: TRBC states response using LQT controller with fixed rotors.

as observed in Fig. 7.6(c). Additionally, the simulation has shown a faster transient response in simulation environment. On the other hand, for θ_1, one can note that the system reactions are similar in terms of time to reach steady state condition. The disparities between experiment and simulation TRBC reaction can be attributed to the modelling process to obtain the nonlinear virtual model which considers inertia and mass properties from CAD model.

In Figs. 7.6(a) and 7.6(b) it is observed that the experimental results have shown large oscillations during the control task. In this case, one can conclude that the response in θ_1 direction is highly affected by θ_4 and $\dot{\theta}_4$ as illustrated in Figs. 7.6(e) and 7.6(f). This event elucidates two effects. First, that the IMU signal quality, in terms of external disturbances, affects the system control. Secondly, for fixed rotor configuration, the TRBC relies on the attitude variation to move laterally. Consequently, the system becomes more susceptible to disturbances in θ_4 and $\dot{\theta}_4$.

The required motor thrust to accomplish the control task is depicted in Fig. 7.7. As can be seen, in both scenarios, f_1 and f_2 are increased to reach the desired altitude. However, the experimental inputs have shown lower amplitudes. Moreover, the calculated inputs were also affected by the attitude signal. It must be pointed out that, in Fig. 7.7(b), experimental f_2 is not driven to the trimming thrust force of 1.7 $[N]$. This indicates a possible disbalance between the TRBC arms. Additionally, simulated f_1 and f_2 are not driven to the trimming thrust indicating that the counter-weight is not in-balance with the TRBC.

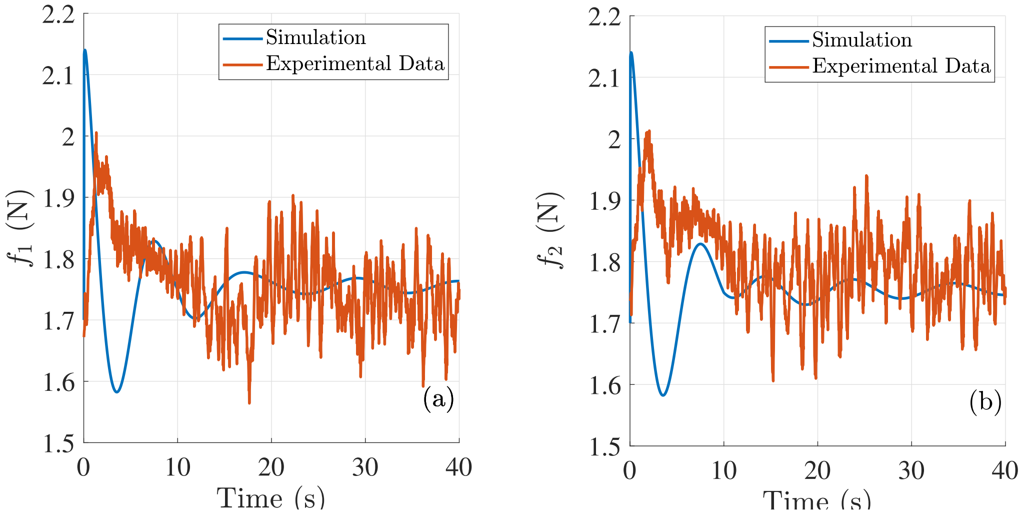

Figure 7.7: TRBC calculated inputs using LQT controller with fixed rotors.

- **TRBC Tracking Controller with Tilting Rotors**

The second experiment scenario is to accomplish the control task including the motor tilt deflection as a control command. For this approach, the calculated gain matrices are:

$$
\mathbf{K}_x = \begin{bmatrix} -0.026276 & 1.3142 & 0.023282 & -0.024783 & 1.3635 & 0.21965 \\ 0.026276 & 1.3142 & -0.023282 & 0.024783 & 1.3635 & -0.21965 \\ 1.2187 & 3e-14 & -0.3329 & 0.83701 & 1e-14 & -0.028572 \\ -1.2187 & -3e-14 & 0.3329 & -0.83701 & -1e-14 & 0.028572 \end{bmatrix}
$$

$$
\mathbf{K}_1 = \begin{bmatrix} -0.0088728 & 0.61929 \\ 0.0088728 & 0.61929 \\ 0.47791 & 1e-14 \\ -0.47791 & -1e-14 \end{bmatrix}
$$

By comparing the resulting matrices for fixed and tilt rotor cases, one can observe some discrepancies in the LQR problem solution. Even though the weighting matrices $\mathbf{Q}_k$ and $\mathbf{R}_k$ are similar for both scenarios, the elements of $\mathbf{K}_1$ and $\mathbf{K}_x$ are not the same. For instance, the elements of $\mathbf{K}_x$ and $\mathbf{K}_1$ corresponding to θ_1, $\dot{\theta}_1$ and e_{θ_1} associated with the thrust force are significantly reduced. In contrast, for the tilt case, it can be clearly noted that the gains related to θ_1, $\dot{\theta}_1$ and e_θ associated with the tilt angles are more prominent. Moreover, θ_2, $\dot{\theta}_2$, θ_4, $\dot{\theta}_4$ and e_{θ_2} gains correlated with the motor thrust are maintained from the fixed to the tilt rotor case. This analysis indicates the control decoupling between the θ_1, θ_4 and θ_2 directions. Under the presented circumstances, when endowed with the tilt mechanism, the lateral control relies mainly on the tilt deflections while the attitude and altitude states are related with the motor thrust variation.

The previous discussion becomes more evident by studying simulation and experimental results. Figure 7.8 shows the TRBC dynamic response using LQT controller with tilting rotors. As can be seen in Fig. 7.8(b) and (d), the altitude response is similar for fixed and tilt rotor configurations, in virtual and experimental environment. Confronting Figs. 7.8(b) and

7.6(b), it is observed that θ_2 presents an overshoot for the tilt case. However, for the tilt case, the system seems to be under the influence of an external disturbance at $t = 7$ $[s]$, which can be an aerodynamic effect or a system malfunction. It can be noted in the motor thrust variation, presented in Fig. 7.11, that the controller acts to compensate this effect increasing f_1 and f_2.

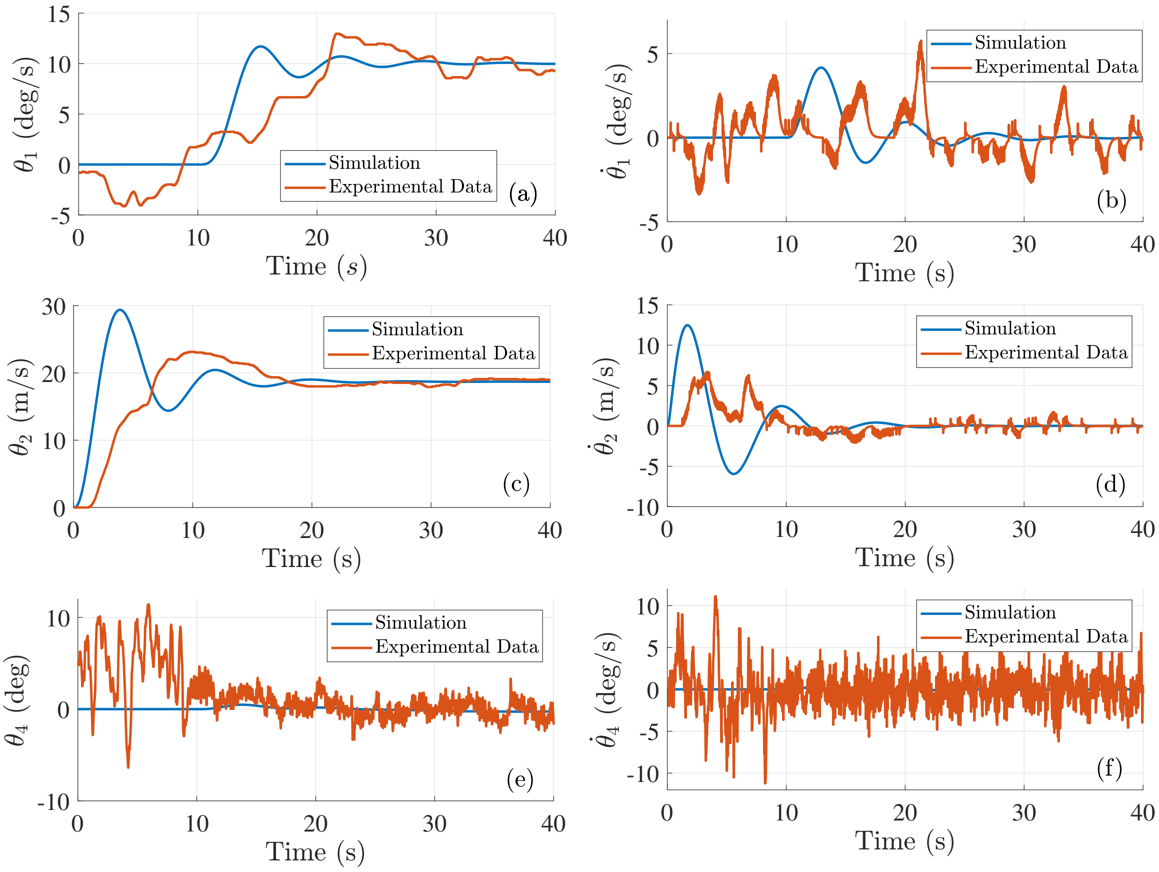

Figure 7.8: TRBC states response using LQT controller with tilting rotors.

Despite the similarity between the altitude responses, the TRBC lateral reaction is highly influenced by the addition of the tilt commands. From Figs. 7.8(a) and 7.8(b), one can infer that the system is less affected by the attitude states (θ_4 and $\dot{\theta}_4$). Consequently, the controller is able to track the reference signal more accurately. As can be seen in Fig. 7.9 the tracking error for the tilt case is smaller if compared with the TRBC with fixed rotors. This leads to an accumulated error, written in terms of Root-Mean-Square (Rms) values, of

3.3792 $[deg]$ and 4.7252 $[deg]$, respectively, indicating an improvement of 28.49%. By contrast, the vertical tracking performance is less affected by the tilt DOF. Figure 7.10 shows that vertical error thought the TRBC operation indicating that the tilt and no tilt cases have similar performance as the accumulated RMS values were 5.2884 $[deg]$ and 5.6378 $[deg]$, respectively. In this case, the tilt controller was able to reduce the tracking error by 6.2%.

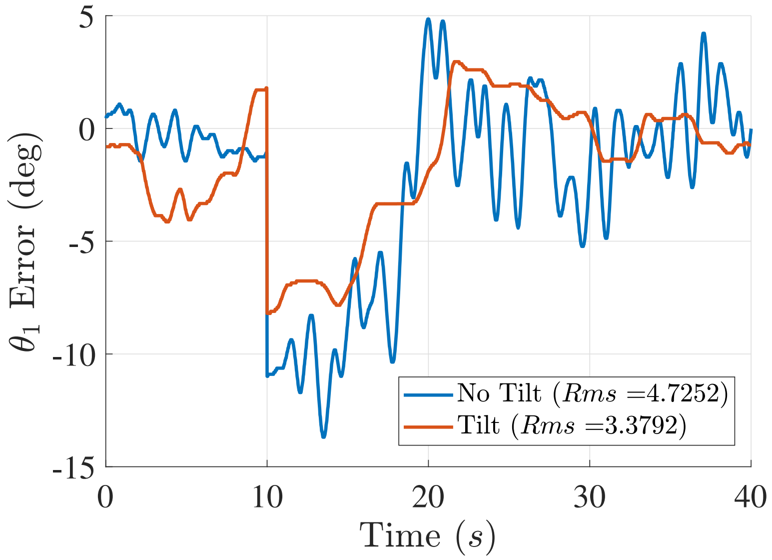

Figure 7.9: Lateral position tracking error comparison for tilt and no tilt cases.

It is noteworthy that the θ_4 and $\dot{\theta}_4$ in Figs. 7.8(e) and 7.8(f) have presented lower amplitudes if compared to Figs. 7.6(e) and 7.6(f). This improvement can be explained by the aforementioned control decoupling. By allowing the motors to tilt, since the lateral control relies on the tilt deflection, the TRBC does not require changes in attitude to track θ_{1des}. Therefore, the IMU signal noise will have lower influence in the system behavior. The motor thrust variation in Fig. 7.11 supports the enhancement on attitude regulation once f_1 and f_2 have lower amplitudes in steady state condition.

Subsequently, the tilt deflection command is examined. Figure 7.12 illustrates the variation of α_1 and α_2 during the mission. It can be noted that the tilt command is highly required during the experiment initialization when $\theta_{1ref} = 0$ $[deg]$. In this case, the TRBC does not de-

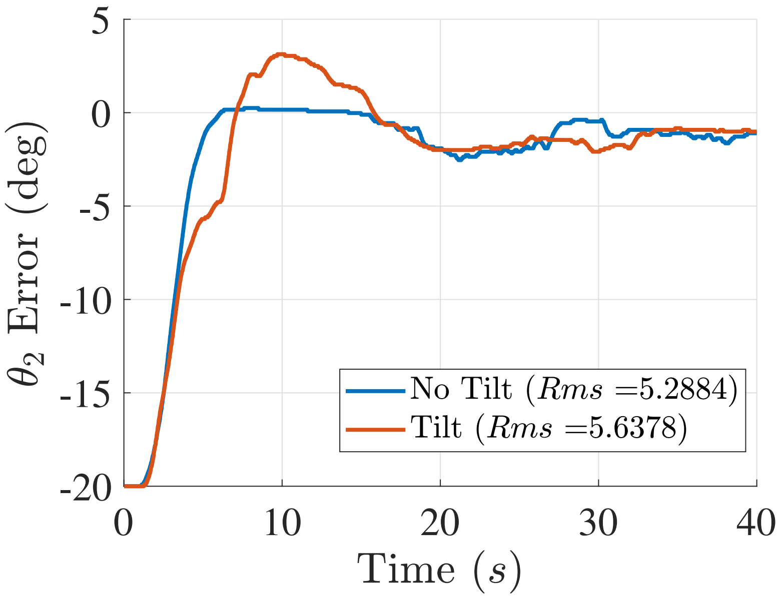

Figure 7.10: Vertical position tracking error comparison for tilt and no tilt cases.

parts from a resting condition differently from the simulation initial condition. After $t = 10$ $[s]$, the controller drives the system to the desired position by manipulating the tilt deflection. It should be pointed out that the system demands lower tilt deflections in the simulation environment. At this point, the difference can be explained by the tilt effectiveness $(l_2 f_{1_0}/den_1)$ modeling. For the virtual model, this parameter is estimated from the CAD mechanical properties. However, as presented in Section 6.4, the identified model has presented discrepancies.

7.4 Chapter Summary

- The LQR controller can be employed for attitude regulation. Experimental results have shown that the regulator is able to improve the TRBC response in θ_4 direction in terms of oscillations with relatively low control effort. The IMU noisy data has a significant effect over the control behavior in this direction.
- For position tracking applications, a LQR based approach can be employed augmenting the controller with integral action forming a Servomechanism Design Model. This con-

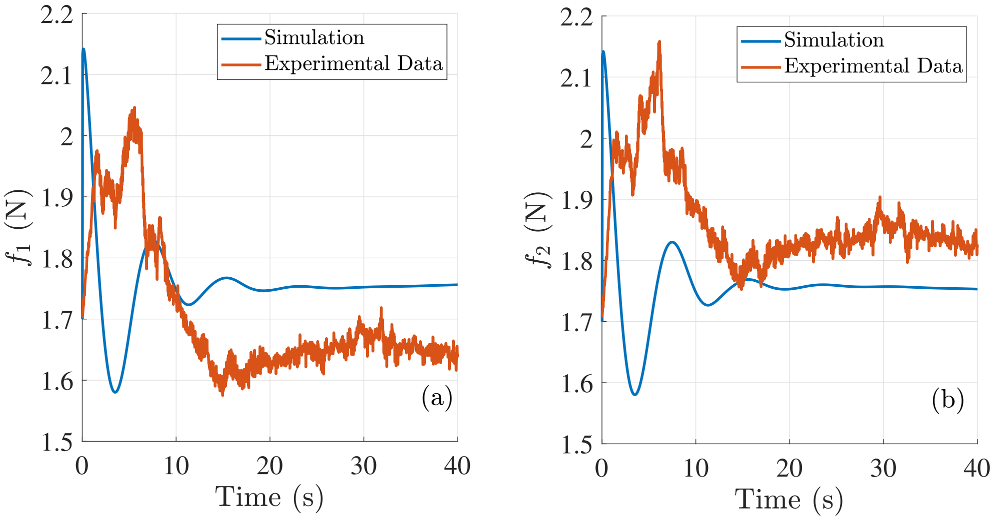

Figure 7.11: TRBC calculated motor thrust using LQT controller with tilting rotors.

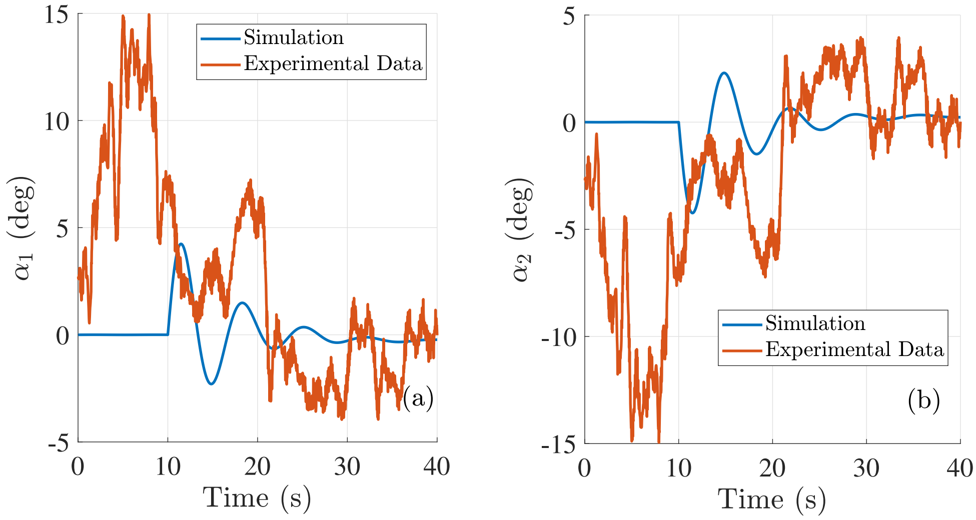

Figure 7.12: TRBC calculated tilt deflections using LQT controller.

trol architecture can be used to track a desired reference position in θ_1 and θ_2 directions.

- From the experiment results and simulations it could be inferred that:
  1. There is a discrepancy between the virtual model and the real system which can be attributed to model uncertainties. Under those circumstances it is recommended to better estimate mass and inertia parameters of the elements and/or use the identified models for better accuracy.

2. Even though the LQT controller was tuned with a linear model, considering calculated parameters and neglecting the actuators dynamics, it was robust enough to achieve an stable response.
3. When the tilt-rotor degree of freedom was included in the model as a control input, the TRBC has presented a better performance if compared to the fixed rotor experiment. It reduced the oscillations in θ_4 direction and, consequently, in θ_1. The system response in θ_2 was less affected.

- The tilt experiment indicates that this extra DOF improves the TRBC lateral response indicating that attitude and position control can be decoupled.

CHAPTER VIII

Tilt-rotor Multi-copter Dynamic Decoupling Problem

As presented in Section 7.3, for multi-copter trajectory tracking missions, the controller may consist of two main loops: one designed for system stabilization and the other to track a desired reference signal. In such cases, all the system's states are regulated simultaneously by the inner feedback controller . Despite that, one of the benefits of enabling the multi-copter tilt DOF is to increase the system's controllability by adding more control degrees of freedom. This characteristic can be explored in order to improve the system response. In this context, a better control allocation can be observed in the test bench TRBC linear state-space model described in (5.40). As can be noted in $\mathbf{B_{TB}}$, the tilt deflection effectiveness is directly related with $\dot{\theta}_1$ while the motor thrust affects $\dot{\theta}_2$ and $\dot{\theta}_4$. This evidence can be observed in Section 7.3 where the experiments have shown that, by enabling lateral tilt deflections in the bi-copter, the system controllability becomes more prominent in θ_1 direction.

The above mentioned control perspective can be explored in order to achieve a better control performance. In other words, for tilt-rotor multi-copters, attitude and position control can be decoupled in a manner that lateral motion is associated with the tilt deflection while vertical an attitude control is achieved by manipulating the motors thrust force. Translating this approach to the TRBC test bench scenario, a control formulation for the TRBC position tracking is proposed. In general terms, the idea is to design a proper controller employed to track desired position references, while holding constant attitude and enforcing actuator constraints. Specifically, an LQR controller is designated to regulate the TRBC attitude (θ_4 DOF) by manipulating the motors thrust force (f_1 and f_2). This inner loop regulator is designed following the LQR methodology presented in Section 7.2. In addition, an outer loop uses a LQT controller, as in Section 7.3, to track the vertical position by manipulating motor thrust commands. Lastly, an MPC is employed to track in-plane (θ_1 DOF) reference position by controlling the tilt angles (α_1 and α_2) while enforcing deflection constraints. From this perspective, this chapter presents an appropriate control formulation to accomplish this specific task.

8.1 TRBC Decoupled Model

In order to make the MPC controller design more comprehensible, the model (5.40) is rearranged, obtaining

$$\begin{bmatrix} \dot{\theta}_4 \\ \ddot{\theta}_4 \\ \dot{\theta}_1 \\ \ddot{\theta}_1 \\ \dot{\theta}_2 \\ \ddot{\theta}_2 \end{bmatrix} = \begin{bmatrix} 0 & 1 & 0 & 0 & & \\ \frac{-c}{I_{zz4}} & \frac{-\mu_4}{I_{zz4}} & 0 & 0 & 0 & 0 \\ 0 & 0 & 0 & 1 & 0 & 0 \\ \frac{-l_2 f_{x0}}{den_1} & 0 & 0 & \frac{-\mu_1}{den_1} & 0 & 0 \\ 0 & 0 & 0 & 0 & 0 & 1 \\ 0 & 0 & 0 & 0 & 0 & \frac{-\mu_2}{den_2} \end{bmatrix} \begin{bmatrix} \theta_4 \\ \dot{\theta}_4 \\ \theta_1 \\ \dot{\theta}_1 \\ \theta_2 \\ \dot{\theta}_2 \end{bmatrix} + \begin{bmatrix} 0 & 0 & 0 & 0 \\ \frac{L_1}{I_{zz4}} & \frac{-L_2}{I_{zz4}} & 0 & 0 \\ 0 & 0 & 0 & 0 \\ 0 & 0 & \frac{l_2 f_{1_0}}{den_1} & \frac{-l_2 f_{2_0}}{den_1} \\ 0 & 0 & 0 & 0 \\ \frac{l_2}{den_2} & \frac{l_2}{den_2} & 0 & 0 \end{bmatrix} \begin{bmatrix} f_1 \\ f_2 \\ \alpha_1 \\ \alpha_2 \end{bmatrix} \tag{8.1}$$

Since θ_1 and θ_2 dynamics are decoupled in Eq. (8.1), θ_2 and $\dot{\theta}_2$ related terms can be removed from the model resulting in

$$\underbrace{\begin{bmatrix} \dot{\theta}_4 \\ \ddot{\theta}_4 \\ \dot{\theta}_1 \\ \ddot{\theta}_1 \end{bmatrix}}_{\dot{\chi}} = \underbrace{\begin{bmatrix} 0 & 1 & 0 & 0 \\ \frac{-c}{I_{zz4}} & \frac{-\mu_4}{I_{zz4}} & 0 & 0 \\ 0 & 0 & 0 & 1 \\ \frac{-l_2 f_{x0}}{den_1} & 0 & 0 & \frac{-\mu_1}{den_1} \end{bmatrix}}_{\mathbf{A}_{TB}} \underbrace{\begin{bmatrix} \theta_4 \\ \dot{\theta}_4 \\ \theta_1 \\ \dot{\theta}_1 \end{bmatrix}}_{\chi} + \underbrace{\begin{bmatrix} 0 & 0 & 0 & 0 \\ \frac{L_1}{I_{zz4}} & \frac{-L_2}{I_{zz4}} & 0 & 0 \\ 0 & 0 & 0 & 0 \\ 0 & 0 & \frac{l_2 {f_1}_0}{den_1} & \frac{-l_2 {f_2}_0}{den_1} \end{bmatrix}}_{\mathbf{B}_{TB}} \underbrace{\begin{bmatrix} f_1 \\ f_2 \\ \alpha_1 \\ \alpha_2 \end{bmatrix}}_{\boldsymbol{\upsilon}} \tag{8.2}$$

which can be written in discrete time domain, by applying the ZOH method, as

$$\chi(k+1) = \bar{\mathbf{A}}_{TB}\chi(k) + \bar{\mathbf{B}}_{TB}\boldsymbol{\upsilon}(k) \tag{8.3}$$

or

$$\begin{bmatrix} \chi_1(k+1) \\ \chi_2(k+1) \end{bmatrix} = \begin{bmatrix} \bar{\mathbf{A}}_{11} & \bar{\mathbf{A}}_{12} \\ \bar{\mathbf{A}}_{21} & \bar{\mathbf{A}}_{22} \end{bmatrix} \begin{bmatrix} \chi_1(k) \\ \chi_2(k) \end{bmatrix} + \begin{bmatrix} \bar{\mathbf{B}}_{11} \\ \bar{\mathbf{B}}_{21} \end{bmatrix} \boldsymbol{\upsilon}_1(k) + \begin{bmatrix} \bar{\mathbf{B}}_{12} \\ \bar{\mathbf{B}}_{22} \end{bmatrix} \boldsymbol{\upsilon}_2(k) \tag{8.4}$$

being $\chi_1 = [\theta_4\ \dot{\theta}_4]^T$, $\chi_2 = [\theta_1\ \dot{\theta}_1]^T$, $\boldsymbol{\upsilon}_1 = [f_1\ f_2]^T$ and $\boldsymbol{\upsilon}_2 = [\alpha_1\ \alpha_2]^T$.

In (8.4) the attitude dynamics can represented by the subsystem

$$\chi_1(k+1) = \bar{\mathbf{A}}_{11}\chi_1(k) + \bar{\mathbf{B}}_{11}\boldsymbol{\upsilon}_1(k) \tag{8.5}$$

As aforementioned, for the regulation of χ_1, it is proposed an optimum control policy described as

$$\upsilon_1(k) = -\bar{\mathbf{K}}\chi_1(k) \tag{8.6}$$

where $\bar{\mathbf{K}}$ is the inner controller gain matrix. At this point, the inner closed loop dynamics is given by

$$\chi_1(k+1) = \underbrace{(\bar{\mathbf{A}}_{11} - \bar{\mathbf{B}}_{11}\bar{\mathbf{K}})}_{\bar{\mathbf{A}}_{cl}}\chi_1(k) \tag{8.7}$$

It must be pointed out that $\bar{\mathbf{K}}$ can be calculated following the LQR procedure presented in Section 7.2. In this case, the inner loop stability is guaranteed if the eigenvalues of $\bar{\mathbf{A}}_{cl}$ are contained in the unitary circle. For the TRBC test bench, specifically, the attitude open loop dynamic is stable as can be seen in Section 6.1. Nevertheless, a regulator controller is suggested in order to achieve a better system response (see the discussion in Subsection 7.2.2).

Now, in order to track the reference in θ_1 direction, the MPC input vector is defined as

$$\mathbf{u}_{mpc}(k) = \begin{bmatrix} \alpha_1(k) \\ \alpha_2(k) \end{bmatrix} \tag{8.8}$$

By substituting (8.6) in (8.4), one can obtain

$$\begin{bmatrix} \chi_1(k+1) \\ \chi_2(k+1) \end{bmatrix} = \begin{bmatrix} \bar{\mathbf{A}}_{11} & \bar{\mathbf{A}}_{12} \\ \bar{\mathbf{A}}_{21} & \bar{\mathbf{A}}_{22} \end{bmatrix} \begin{bmatrix} \chi_1(k) \\ \chi_2(k) \end{bmatrix} + \begin{bmatrix} \bar{\mathbf{B}}_{11} \\ \bar{\mathbf{B}}_{21} \end{bmatrix} \Big(-\bar{\mathbf{K}}\chi_1(k) \Big) + \begin{bmatrix} \bar{\mathbf{B}}_{12} \\ \bar{\mathbf{B}}_{22} \end{bmatrix} \begin{bmatrix} \alpha_1(k) \\ \alpha_2(k) \end{bmatrix} \tag{8.9}$$

which can be rearranged on the following state space model:

$$\begin{bmatrix} \chi_1(k+1) \\ \chi_2(k+1) \end{bmatrix} = \begin{bmatrix} \bar{\mathbf{A}}_{11} - \bar{\mathbf{B}}_{11}\bar{\mathbf{K}} & \bar{\mathbf{A}}_{12} \\ \bar{\mathbf{A}}_{21} - \bar{\mathbf{B}}_{21}\bar{\mathbf{K}} & \bar{\mathbf{A}}_{22} \end{bmatrix} \begin{bmatrix} \chi_1(k) \\ \chi_2(k) \end{bmatrix} + \begin{bmatrix} \bar{\mathbf{B}}_{12} \\ \bar{\mathbf{B}}_{22} \end{bmatrix} \begin{bmatrix} \alpha_1(k) \\ \alpha_2(k) \end{bmatrix} \tag{8.10}$$

In order to track the desired position in θ_1 direction, it is assumed that the input reference vector is given by

$$\mathbf{r}_{mpc} = \begin{bmatrix} \theta_{1ref} \\ \dot{\theta}_{1ref} \end{bmatrix} \tag{8.11}$$

One may note that, differently from the LQT controller, the reference vector (8.11) contains $\dot{\theta}_1$. In this case, including the velocity state as reference signal is substantial to have a smoother trajectory tracking. Thereby, the MPC output vector is

$$\gamma(k) = \begin{bmatrix} 0 & 0 & 1 & 0 \\ 0 & 0 & 0 & 1 \end{bmatrix} \begin{bmatrix} \chi_1(k) \\ \chi_2(k) \end{bmatrix} \tag{8.12}$$

8.1.1 Including the Tilt Mechanism Dynamics

In effect, from the estimated tilt mechanism models in (6.9) and (6.10), it is expected that their dynamics carry influence over the lateral response. Therefore, in order to have a reliable model for the MPC design, (8.10) must comprise the dynamic association between the desired command (α_{cm}) and the effective tilt deflection (α_{ef}). This relation can be written in state-space format as:

$$\underbrace{\begin{bmatrix} \dot{\alpha}_{ef1} \\ \ddot{\alpha}_{ef1} \\ \dot{\alpha}_{ef2} \\ \ddot{\alpha}_{ef2} \end{bmatrix}}_{\dot{\chi}_\alpha} = \underbrace{\begin{bmatrix} 0 & 1 & 0 & 0 \\ -28.695 & -8.145 & 0 & 0 \\ 0 & 0 & 0 & 1 \\ 0 & 0 & -28.228 & -8.033 \end{bmatrix}}_{\mathbf{A}_\alpha} \underbrace{\begin{bmatrix} \alpha_{ef1} \\ \dot{\alpha}_{ef1} \\ \alpha_{ef2} \\ \dot{\alpha}_{ef2} \end{bmatrix}}_{\chi_\alpha} + \underbrace{\begin{bmatrix} 0 & 0 \\ 28.695 & 0 \\ 0 & 0 \\ 0 & 28.228 \end{bmatrix}}_{\mathbf{B}_\alpha} \underbrace{\begin{bmatrix} \alpha_{cm1} \\ \alpha_{cm2} \end{bmatrix}}_{\upsilon_\alpha} \tag{8.13}$$

The above model can be incorporated in (8.2) in order to obtain an augmented continuous time state-space model. Thereafter, by assuming that $\alpha_{cm1} = \alpha_1$ and $\alpha_{cm2} = \alpha_2$, ZOH method is employed to obtain the following discrete time state-space model:

$$\underbrace{\begin{bmatrix} \chi_1(k+1) \\ \chi_2(k+1) \\ \chi_\alpha(k+1) \end{bmatrix}}_{\chi_{mpc}(k+1)} = \underbrace{\begin{bmatrix} \bar{\mathbf{A}}_{11} - \bar{\mathbf{B}}_{11}\bar{\mathbf{K}} & \bar{\mathbf{A}}_{12} & \mathbf{O} \\ \bar{\mathbf{A}}_{21} - \bar{\mathbf{B}}_{21}\bar{\mathbf{K}} & \bar{\mathbf{A}}_{22} & \mathbf{O} \\ \mathbf{O} & \mathbf{O} & \bar{\mathbf{A}}_\alpha \end{bmatrix}}_{\mathbf{A}_{mpc}} \underbrace{\begin{bmatrix} \chi_1(k) \\ \chi_2(k) \\ \chi_\alpha(k) \end{bmatrix}}_{\chi_{mpc}(k)} + \underbrace{\begin{bmatrix} \bar{\mathbf{B}}_{12} & \bar{\mathbf{B}}_{11}\mathbf{1}_{2\times 1} & \mathbf{O} \\ \bar{\mathbf{B}}_{22} & \bar{\mathbf{B}}_{21}\mathbf{1}_{2\times 1} & \mathbf{O} \\ \mathbf{O} & \mathbf{O} & \bar{\mathbf{B}}_\alpha \end{bmatrix}}_{\mathbf{B}_{mpc}} \underbrace{\begin{bmatrix} \alpha_1(k) \\ \alpha_2(k) \end{bmatrix}}_{\mathbf{u}_{mpc}(k)} \tag{8.14}$$

and

$$\gamma_{mpc}(k) = \underbrace{\begin{bmatrix} 0 & 0 & 1 & 0 & 0 & 0 & 0 & 0 \\ 0 & 0 & 0 & 1 & 0 & 0 & 0 & 0 \end{bmatrix}}_{\mathbf{C}_{mpc}} \chi_{mpc}(k) \tag{8.15}$$

As will be discussed later, the Model Based Predictive Controllers performance relies on the correct prediction of the states in the horizon. Therefore, a simple, but accurate enough model is recommended. In this sense, model (8.14) is employed for control design purposes.

The influence of including or not the tilt dynamics in the predictive model will be discussed in the next sections. Additionally, differently from the LQR controller, the identified properties from Table 6.1 will be assumed for better dynamic representation.

8.2 State Observer

As can be noted, for the present study, the test bench mechanical assembly does not have a proper device to measure the tilt deflection angles. Therefore, the full state vector $\chi_{mpc}(k)$ in model (8.14) can not be measured at each time sample. Consequently, α_{ef1}, α_{ef2}, $\dot{\alpha}_{ef1}$ and $\dot{\alpha}_{ef2}$ are not available and state feedback can not be assumed for the MPC design. In order to overcome this, a Luenberger state observer can be designed to estimate χ_{mpc} from the system output $\mathbf{y}_{mpc}$ (BURNS, 2001).

Considering the system described by the complete dynamics, written in discrete domain, as:

$$\chi_{obs}(k+1) = \bar{\mathbf{A}}_{obs}\chi_{obs}(k) + \bar{\mathbf{B}}_{obs}\upsilon_{obs}(k) \tag{8.16}$$

being $\chi_{obs} = [\theta_4\ \dot{\theta}_4\ \theta_1\ \dot{\theta}_1\ \theta_2\ \dot{\theta}_2\ \alpha_{ef1}\ \alpha_{ef2}\ \dot{\alpha}_{ef1}\ \dot{\alpha}_{ef2}]^T$ and $\upsilon = [f_1\ f_2\ \alpha_1\ \alpha_2]^T$ and the output state vector given by $\gamma_{obs}(k) = \mathbf{C}_{obs}\chi_{obs}$ with

$$\mathbf{C}_{obs} = \begin{bmatrix} 1 & 0 & 0 & 0 & 0 & 0 & 0 & 0 & 0 & 0 \\ 0 & 1 & 0 & 0 & 0 & 0 & 0 & 0 & 0 & 0 \\ 0 & 0 & 1 & 0 & 0 & 0 & 0 & 0 & 0 & 0 \\ 0 & 0 & 0 & 1 & 0 & 0 & 0 & 0 & 0 & 0 \\ 0 & 0 & 0 & 0 & 1 & 0 & 0 & 0 & 0 & 0 \\ 0 & 0 & 0 & 0 & 0 & 1 & 0 & 0 & 0 & 0 \end{bmatrix} \tag{8.17}$$

Assume that an estimate of the state vector χ_e is given by

$$\chi_e(k) = \bar{\mathbf{A}}_{obs}\chi_e(k-1) + \bar{\mathbf{B}}_{obs}\upsilon_{obs}(k-1) + \mathbf{L}_{obs}(\gamma_{obs}(k-1) - \mathbf{C}_{obs}\chi_e(k-1)) \tag{8.18}$$

where $\mathbf{L}_{obs} \in \mathbb{R}^{(n_e \times n_m)}$ is the observer gain matrix with $n_e = 10$ the number of variables to estimate and $n_m = 6$ the number of measured states.

The prediction error $\mathbf{e}_e$ can be calculated by subtracting (8.18) from (8.16) obtaining

$$\mathbf{e}_e(k) = (\bar{\mathbf{A}}_{obs} - \mathbf{L}_{obs}\mathbf{C}_{obs})\mathbf{e}_e(k-1) \tag{8.19}$$

Thus, from equation (8.19), the dynamic behavior of the error vector depends upon the eigenvalues of $(\bar{\mathbf{A}}_{obs} - \mathbf{L}_{obs}\mathbf{C}_{obs})$. As in many measurements system, these eigenvalues should allow the observer transient response to be faster than the system itself unless a filtering effect is required.

As can be noted, the problem of observer design is essentially the same as the regulator pole placement problem. Therefore, similar techniques may be used as the Direct Comparison method, Observable Canonical Form Method, the Ackerman formula and/or the Linear Quadratic Estimator solution (BURNS, 2001). In this work, the last procedure is preferred. Hence, $\mathbf{L}_{obs}$ can be estimated by finding the observer gain matrix that minimizes the steady-state error covariance (FRIEDLAND, 2012)

$$\mathbf{P}_{obs} = \lim_{t\to\infty} E\{(\chi_{obs}(k) - \chi_e(k))(\chi_{obs}(k) - \chi_e(k))^T\} \tag{8.20}$$

The solution of Eq. (8.20) satisfies

$$\dot{\mathbf{P}}_{obs} = \bar{\mathbf{A}}_{obs}\mathbf{P}_{obs} + \mathbf{P}_{obs}\bar{\mathbf{A}}_{obs} - \mathbf{P}_{obs}\mathbf{C}_{obs}\mathbf{R}_{obs}^{-1}\mathbf{C}_{obs}\mathbf{P}_{obs} + \mathbf{F}\mathbf{Q}_{obs}\mathbf{F}^T \tag{8.21}$$

and

$$\mathbf{P}_{obs}(0) = E\{(\chi_{obs}(0) - \chi_e(0))(\chi_{obs}(0) - \chi_e(0))^T\} \tag{8.22}$$

being $\mathbf{Q}_{obs} \succ 0$ and $\mathbf{R}_{obs} \succ 0$ the estimated and measured states weighting matrices with proper dimensions.

Therefore, given the weighting matrices $\mathbf{Q}_{obs}$ and $\mathbf{R}_{obs}$, one can use Eq. (8.21) to determine the observer gain matrix that $\mathbf{P}_{obs}$ is as small as possible. This leads to

$$\mathbf{L}_{obs} = \mathbf{P}_{obs}\mathbf{C}_{obs}\mathbf{R}_{obs}^{-1} \tag{8.23}$$

Theoretically, the solution (8.23) is only feasible if the system is observable. In other words, if matrix $\mathbf{N} = [\mathbf{C}_{obs}^T : \bar{\mathbf{A}}_{obs}^T : \cdots : (\bar{\mathbf{A}}_{obs})^{n_e-1}\ \mathbf{C}_{obs}^T]$ is of rank n_e. It occurs that, for the study case model (8.16), the observability condition is not satisfied since the rank of $\mathbf{N}$ is 8. The non-observable states are associated to the lack of sensors to measure the tilt angles. However, since these states are stable, the detectability condition is satisfied. Henceforth, assuming that the pair $(\bar{\mathbf{A}}_{obs}^T, \mathbf{C}_{obs}^T)$ is stabilizable, it is possible to define matrices $\mathbf{Q}_{obs}$ and $\mathbf{R}_{obs}$ so that $(\mathbf{Q}_{obs}, \bar{\mathbf{A}}_{obs}^T)$ has no unobservable modes on the unit circle (BITTANTI; BOLZERN, 1985). Under those circumstances, it is possible to determine $\mathbf{L}_{obs}$ by (8.23) if matrices $\mathbf{Q}_{obs}$ and $\mathbf{R}_{obs}$ are properly tuned.

8.3 Altitude Controller

As previously mentioned, the LQT control methodology presented in Section 7.3 will be employed to track a desired angular position in θ_2 direction. For this, let the altitude dynamics be represented in discrete time state space format as:

$$\chi_3(k+1) = \bar{\mathbf{A}}_3\chi_3(k) + \bar{\mathbf{B}}_3\upsilon_3(k) \tag{8.24}$$

where $\chi_3 = [\theta_2\ \dot{\theta}_2]^T$ and $\upsilon_3 = [f_1\ f_2]^T$. Additionally $\bar{\mathbf{A}}_3 \in \mathbb{R}^{2\times2}$ and $\bar{\mathbf{B}}_3 \in \mathbb{R}^{2\times2}$ are extracted from the TRBC model (8.1).

Then, by assuming that the system has full state feedback and a constant reference position ($\mathbf{r}_{alt} = [\theta_{2ref}]$) the altitude error can be written as

$$\mathbf{e}_{alt} = \underbrace{[1\ 0]}_{\mathbf{C_{calt}}}\chi_3 - \mathbf{r}_{alt} \tag{8.25}$$

Therefore, following the servomechanism design procedure, the gain matrix $\mathbf{K}_{alt} = [\mathbf{K}_{1alt}\ \mathbf{K}_{xalt}]$ can be calculated by means of the Riccati equation problem. As a result, the required input for altitude tracking is given by:

$$\upsilon_3 = -\mathbf{K}_{xalt}\chi_3 + \mathbf{K}_{1alt}\int \mathbf{e}_{alt} \tag{8.26}$$

8.4 Model Predictive Control

As can be appraised in the literature, the LQR controller can show good performance and robustness for multi-copter stabilization tasks (BOUABDALLAH et al., 2004). Also, it can be shown that the closed-loop system (7.14) is stable and has reasonable stability margins (LAVRETSKY; WISE, 2013). The LQR robustness performance is corroborated by Sections 7.2 and 7.3 results. Withal, in the presence of constraints, such stability guarantees may not hold. In order to overcome this dilemma and enforce state and control constraints, a Model Predictive Controller (MPC) can be employed. Herein, the MPC is included in the control loop with the purpose of tracking a desired reference signal **r** while enforcing actuation constraints.

According to Rossiter (2005) the design of a proper MPC has some center principles. To begin with, the control law depends on a predicted behavior given by an *internal model*. Therefore, a proper model must be selected to generate system predictions such that the output can be computed over a *prediction horizon*. In this case, it is suggested to pick up the simplest model with relatively accurate predictions.

Prediction Horizon: *The prediction horizon determines how far ahead from the actual sampling time a model can predict future states based on the system's measured outputs and a given system input.*

By using the internal model dynamics, the predicted inputs are selected through the *Principle of Optimality* by minimizing some measure of predicted performance. The later can be mathematically translated in a cost function which can be tuned to attend the performance requirements. The resulting approach is often called the receding horizon strategy as defined in Maciejowski (2002).

Receding Horizon: *In MPC the prediction horizon length remains constant over time, but slides along by one sampling interval at each time step. In this context, for a given sampling instant, the control actions are updated using new information from far horizon. As a consequence, the prediction horizon should include all system's significant dynamics. Otherwise significant events may be unobserved and the controller performance may be compromised.*

In conformity with the given definitions, the control design formulation will be presented in the following sections.

8.4.1 *Predictive Control Formulation*

Herein, a linearized, discrete-time, time-invariant, state-space model of the plant in the form of Eq. (8.14) will be assumed. Therefore, measuring the present time state vector $\chi_{mpc}(k)$ and knowing the applied control sequence $\Delta\hat{\boldsymbol{\upsilon}}_{mpc}(k+i-1|k)$ one can determine the future output predictions $\hat{\gamma}_{mpc}(k+1|k)$ up to N_x steps in the future. In such case, N_x is commonly named as the "Prediction Horizon". Additionally, the control increments can be denoted as $\Delta\hat{\boldsymbol{\upsilon}}_{mpc}(k+i-1|k) = \hat{\boldsymbol{\upsilon}}_{mpc}(k+i-1|k) - \hat{\boldsymbol{\upsilon}}_{mpc}(k+i-2|k)$. The symbol " ^ " designates predicted elements indicating that the optimal control sequence at time k can still change.

As previously discussed, the predicted inputs can be selected by an optimization algorithm. Herein, the idea is to transform the input prediction optimization in a quadratic programming problem (ROSSITER, 2005). This procedure is aimed at determining the sequence of future control increments $\Delta\hat{\boldsymbol{\upsilon}}_{mpc}(k+i-1|k), i = 1,\ldots,N_u$, that minimize the following cost function

$$\begin{aligned} J_{mpc} = & \sum_{k=1}^{N_x} \left(\left[\hat{\gamma}_{mpc}(k+i|k) - \mathbf{r}_{mpc} \right]^T \right] \mathbf{Q}_{mpc} \left(\hat{\gamma}_{mpc}(k+i|k) - \mathbf{r}_{mpc} \right]^T \left] \right) \\ & + \sum_{k=1}^{N_u} \left([\Delta\hat{\boldsymbol{\upsilon}}_{mpc}(k+i-1|k)]^T \, \mathbf{R}_{mpc} \, [\Delta\hat{\boldsymbol{\upsilon}}_{mpc}(k+i-1|k)]^T \right) \end{aligned} \tag{8.27}$$

where $Q_{mpc} \succ 0 \in \mathbb{R}^{(n_x \times n_x)}$ and $R_{mpc} \succ 0 \in \mathbb{R}^{(n_u \times n_u)}$ are weighting matrices. The value of N_u, also known as the "Control Horizon", is typically smaller than N_x so that the optimization assumes that $\Delta\hat{\boldsymbol{\upsilon}}_{mpc}(k+i-1|k) = 0$ for $N_u < i \leq N_x$. In addition, the receding horizon strategy is employed to estimate the control inputs. Consequently, only the first element of the optimized control sequence ($\boldsymbol{\upsilon}^{\star}_{mpc}(k)$) is applied to the model. Then, the optimization is repeated in the next sampling instant, assuming new measurements.

It must be noted that the cost function (8.27) penalizes the predicted control outputs $\hat{\gamma}_{mpc}(k+i|k)$ from a reference trajectory $\mathbf{r}_{mpc}$ in terms of $\mathbf{Q}_{mpc}$. In that sense, the tracking error minimization can be tuned by adjusting the values of $\mathbf{Q}_{mpc}$. Whereas, $\mathbf{R}_{mpc}$ penalizes the changes in the input vector. Increasing the values of $\mathbf{R}_{mpc}$ results in lower input increments, smaller control commands and, consequently, slower system response. Meanwhile, with smaller $\mathbf{R}_{mpc}$ terms, the speed of the closed-loop response can be increased. In this case, the system is more susceptible to larger control effort and a greater sensitivity to measured noise.

As can be seen, the MPC optimization solution is affected by the choice of the design variables such as: the prediction horizons N_x and N_u, the weighting matrices $\mathbf{Q}_{mpc}$ and $\mathbf{R}_{mpc}$, the reference trajectory $\mathbf{r}_{mpc}$ and sample time T_s. All these parameters directly influence the behavior of the closed-loop combination of the plant and predictive controller. For this reason, they are generally selected in a trade-off analysis.

For instance, the weights, in particular, are associated with the energetic objectives of the control system. They are in effect tuning parameters which are adjusted to give satisfactory performance similarly to the LQR matrices $\mathbf{Q}_k$ and $\mathbf{R}_k$. Moreover, the prediction horizons are related with the system transient behavior. With larger horizons, the system is able "see" further the system dynamics, improving the optimization procedure, in terms of cost function minimization, and the tracking performance. On the other hand, larger horizons culminates in high-dimensional prediction model matrices and the optimization solution becomes computational costly. Under those circumstances, the system may not be able to run the optimization algorithm within the sample time T_s resulting in control delays. If the sample time is increased to overcome sampling time mismatch, control performance is affected in manner that the system can be driven to instability. A further discussion about the influence of the MPC design parameters can be found in Maciejowski (2002).

In (8.27) the relation between $\hat{\gamma}_{mpc}$ and $\hat{\upsilon}_{mpc}$ can be expressed in terms of a prediction equation based on a incremental state-space model. A methodology employed to obtain the prediction model for state space representation is presented in Appendix A. Herein, for the TRBC MPC implementation, the problem can be particularized applying the described procedure adopting the model presented in Eq. (8.14). Assuming that the prediction model of the output vector, in terms of the input increments, is represented by Eq. (A.20), the cost function can be written as:

$$J_{mpc}(k) = \left(\hat{\mathbf{Y}} - \mathbf{r}\right)^T \mathbf{Q}_N \left(\hat{\mathbf{Y}} - \mathbf{r}\right) + \Delta\hat{\mathbf{U}}^T \mathbf{R}_N \Delta\hat{\mathbf{U}} \tag{8.28}$$

where

$$\mathbf{r} = \begin{bmatrix} \mathbf{r}_{mpc}(k+1) \\ \mathbf{r}_{mpc}(k+2) \\ \vdots \\ \mathbf{r}_{mpc}(k+N_x) \end{bmatrix} , \qquad \mathbf{Q}_N = \begin{bmatrix} \mathbf{Q}_{mpc} & \mathbf{0}_{n_s \times n_s} & \cdots & \mathbf{0}_{n_s \times n_s} \\ \mathbf{0}_{n_s \times n_s} & \mathbf{Q}_{mpc} & \cdots & \mathbf{0}_{n_s \times n_s} \\ \vdots & \vdots & \ddots & \vdots \\ \mathbf{0}_{n_s \times n_s} & \mathbf{0}_{n_s \times n_s} & \cdots & \mathbf{Q}_{mpc} \end{bmatrix}$$

$$\text{and} \qquad \mathbf{R}_N = \begin{bmatrix} \mathbf{R}_{mpc} & \mathbf{0}_{n_u \times n_u} & \cdots & \mathbf{0}_{n_u \times n_u} \\ \mathbf{0}_{n_u \times n_u} & \mathbf{R}_{mpc} & \cdots & \mathbf{0}_{n_u \times n_u} \\ \vdots & \vdots & \ddots & \vdots \\ \mathbf{0}_{n_u \times n_u} & \mathbf{0}_{n_u \times n_u} & \cdots & \mathbf{R}_{mpc} \end{bmatrix}$$

Now, replacing (A.20) in (8.28) yields

$$J_{mpc}(k) = \left(\mathbf{f} + \mathbf{G}\Delta\hat{\mathbf{U}} - \mathbf{r}\right)^T \mathbf{Q}_N \left(\mathbf{f} + \mathbf{G}\Delta\hat{\mathbf{U}} - \mathbf{r}\right) + \Delta\hat{\mathbf{U}}^T \mathbf{R}_N \Delta\hat{\mathbf{U}} \tag{8.29}$$

which can be rewritten as

$$J_{mpc}(k) = \Delta\hat{\mathbf{U}}^T \left(\mathbf{G}^T\mathbf{Q}_N\mathbf{G}+\mathbf{R}_N\right)\Delta\hat{\mathbf{U}} + 2\left(\mathbf{f}-\mathbf{r}\right)^T\mathbf{Q}_N\mathbf{G}\Delta\hat{\mathbf{U}} + 2\left(\mathbf{f}-\mathbf{r}\right)^T\mathbf{Q}_N\left(\mathbf{f}-\mathbf{r}\right) \tag{8.30}$$

$$J_{mpc}(k) = \frac{1}{2}\Delta\hat{\mathbf{U}}^T\mathbf{H}_{qp}\Delta\hat{\mathbf{U}} + \mathbf{f}_{qp}\Delta\hat{\mathbf{U}} + cte \tag{8.31}$$

being

$$\mathbf{H}_{qp} = 2(\mathbf{G}^T\mathbf{Q}_N\mathbf{G}+\mathbf{R}_N) \ , \ \mathbf{f}_{qp} = 2\mathbf{Q}_N\mathbf{G}(\mathbf{f}-\mathbf{r}) \ \text{ and } \ cte = (\mathbf{f}-\mathbf{r})^T\mathbf{Q}_N(\mathbf{f}-\mathbf{r})$$

As can be noted in (8.31), the cost function at each sample time ($J_{mpc}(k)$) is written in terms of the decision variables ($\Delta\hat{\boldsymbol{\upsilon}}$) solely. Therefore, the control increments can be obtained through the minimization of (8.31) subjected to a set of linear constraints.

In particular, for the TRBC control problem, it is recommended to include constraints in the MPC optimization accounting for the tilt excursion limitation. Therefore, if restrictions of the type $\boldsymbol{\upsilon}_{min} \leq \hat{\boldsymbol{\upsilon}}(k-1+i|k) \leq \boldsymbol{\upsilon}_{max}$, $i \in \{1,\ldots,N_u\}$ and $\Delta\boldsymbol{\upsilon}_{min} \leq \Delta\hat{\boldsymbol{\upsilon}}(k-1+i|k) \leq \Delta\boldsymbol{\upsilon}_{max}$, $i \in \{1,\ldots,N_u\}$ are to be satisfied by the manipulated control variables, the cost function minimization is subjected to a set of linear constraints represented as

$$\mathbf{A}_{qp}\Delta\hat{\mathbf{U}} \leq \mathbf{b}_{qp} \tag{8.32}$$

The procedure to write the restrictions in terms of the predicted decision variables is described in Appendix B. Matrices $\mathbf{A}_{qp}$ and $\mathbf{b}_{qp}$ can be directly determined from the model parameters, instant time state, input vectors ($\boldsymbol{\chi}_{mpc}(k)$ and $\mathbf{u}_{mpc}(k-1)$) and lower and upper control limitations ($\Delta\boldsymbol{\upsilon}_{min}$, $\Delta\boldsymbol{\upsilon}_{max}$, $\boldsymbol{\upsilon}_{min}$ and $\boldsymbol{\upsilon}_{max}$).

Minimizing (8.30) subjected to (8.32) is a Quadratic Programming problem, i.e. quadratic cost with linear constraints, for which efficient numerical algorithms are available (MACIEJOWSKI, 2002). The optimization procedure, whose output is an optimal control increment sequence ($\Delta\hat{\boldsymbol{\upsilon}}^{\star}_{mpc}(k+i|k),\ i=0,\ 1,\ 2,\ldots,\ N_u-1$), is repeated at each time step. In this case, only the first vector of $\Delta\hat{\boldsymbol{\upsilon}}^{\star}_{mpc}$ is used to compute the control action, that is,

$$\boldsymbol{\upsilon}_{mpc}(k) = \hat{\boldsymbol{\upsilon}}^{\star}_{mpc}(k|k) = \Delta\hat{\boldsymbol{\upsilon}}^{\star}_{mpc}(k|k) + \boldsymbol{\upsilon}_{mpc}(k-1) \tag{8.33}$$

At time instant $k+1$, the optimization is repeated following the receding horizon strategy.

In summary, the elements of the control formulation adopted for TRBC position tracking considering decoupled dynamics are presented as a block diagram scheme in Fig. 8.1. The figure illustrates the proposed control architecture comprising the lateral, altitude and attitude controllers as previously described.

It must be pointed out that, by assuming the dynamic decoupling formulation, attitude and altitude control effort are summed up in order to provide the required thrust force for each rotor. Apart from that, the MPC handles the lateral displacement associated with the tilt angle deflection. Consequently, the cost function (8.30) and the constraints (8.32) are not directly affected by f_1 and f_2, but by α_1 and α_2. Nevertheless, a particular attention must be given to the inner loop attitude controller. Providing that θ_4 and θ_1 dynamics are coupled, the input constraints and prediction model requires attitude information to update the prediction model. As a result, J_{mpc} minimization is connected with the LQR control performance. Under those circumstances, one can say that the MPC is watching the inner loop control behavior and the MPC solution may be affected by unbalanced f_1 and f_2 variations.

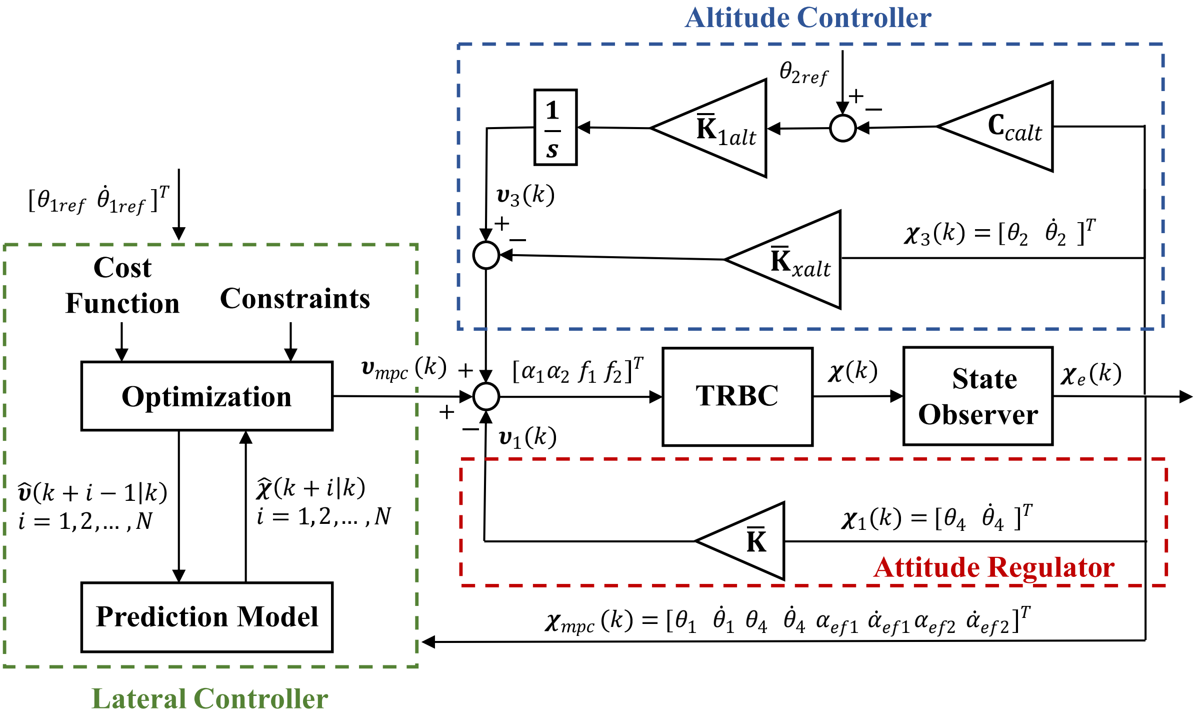

Figure 8.1: Test-bench dynamic decoupling controller.

A solution which includes the vertical controller in the MPC is presented in Marques et al. (2020). In this case, the MPC output also contains the required symmetric thrust force variation for altitude tracking. For the present work, the choice of designing an MPC only for the lateral motion is supported by three assumptions. First, since the dynamics are decoupled, the altitude variation has no effect in lateral control and, therefore, it does not affect the estimation of the decision variables through J_{mpc} minimization. Secondly, for the TRBC experiment, since the tilt angles control efforts are more restricted than the motor thrust force, the MPC can be beneficial in handling the deflection constraints but may not be necessary for thrust force limitation. Lastly, by reducing the number of state variables, the computational burden to solve the optimization problem is decreased allowing larger number of prediction horizons and improving transient response.

For this particular problem, another feasible approach is to design an LQR controller to regulate all the states simultaneously. Then, one can consider a terminal constraint where the LQR has stability guarantees while the MPC enforces constraints. For this approach, the methodologies presented in Rossiter (2005) and Almeida & Leissling (2009) are recommended.

8.5 MPC Experimental Results

In this section, the dynamic decoupling methodology, presented in this chapter, will be experimented in the test bench TRBC. The goal is to validate the proposed formulation investigating, primarily, the MPC behavior. In order to achieve this, two tests are proposed. First, an horizontal displacement in θ_1 direction maneuver maintaining θ_2 DOF locked. Secondly, it is considered position references in θ_1 and θ_2 directions. The differences between both scenarios will be discussed subsequently.

8.5.1 Horizontal Displacement Experiment

For this first scenario, a constant position reference of 30 $[deg]$ is applied in θ_1 direction while the altitude was maintained in $\theta_2 = 0$. Additionally, $\dot{\theta}_{1ref} = 0$. In order to investigate the effect of the tilt-rotor on the system response, the actuator dynamics, represented by the identified transfer functions (6.9) and (6.10), were neglected in the MPC design. Therefore, the decoupled model described in Eq.(8.4) is employed adopting the identified parameters described in Table 6.1.

First, the LQR attitude controller gains were calculated with same weights as in 7.2.2 where $\mathbf{Q}_k = diag([1.6\ 0.3])$ and $\mathbf{R}_k = diag([0.2\ 0.2])$ which leads to (7.15). Then, the MPC was designed with $\mathbf{Q}_{mpc} = \mathrm{diag}([5\ \ 0.01])$, $\mathbf{R}_{mpc} = \mathrm{diag}([1\ \ 1])$, $N_x = 12$, $N_u = 6$ and $T_s = 0.02$ $[s]$. In addition, for practical purposes, the tilt excursion is constrained respecting the mechanism limitation, i.e.

$$\mathbf{u}_{max} = \begin{bmatrix} 0.3491 \\ 0.3491 \end{bmatrix} \qquad \text{and} \qquad \mathbf{u}_{min} = \begin{bmatrix} 0 \\ 0 \end{bmatrix} \tag{8.34}$$

in $[rad]$ which means that $0 \leq \alpha \leq 20$ $[deg]$.

It is worth mentioning that, as previously discussed, the optimum MPC solution is obtained recursively by means of quadratic programming solution for each time sample. For numerical simulations the Multi Parametric Toolbox is employed in Matlab environment (FERREAU et al., 2014). Meanwhile, for experimental implementation, the qpOASES C++ library is preferred. This last can be programmed on-board as part of the embedded software presented in Section 4.4.

For this particular experiment, the main goal is to evaluate the TRBC response when the MPC is employed without considering the tilt dynamics. Under these circumstances, the linear model simulations (cases 1, 2 and 3) are compared with experimental results (case 4) are considering four study cases as listed below:

- *Case 1* - the nominal linear model in Eq. (8.1) is used to estimate the state vector $\chi(k)$.
- *Case 2* - a third order identified model described in Eq. (6.11) is used to substitute the first order θ_1 equation in (8.1). In this case, the tilt dynamics are included indirectly in the simulation model through α to θ_1 relation.
- *Case 3* - a second order tilt dynamic model from Eqs. (6.9) and (6.10) is used to calculate the effective tilt angle in advance of numerically estimating the system state vector.
- *Case 4* - experimental implementation of the MPC neglecting the tilt dynamics in control design.

A comparison between the above mentioned scenarios is presented in Fig. 8.2 and 8.3. From the presented results, it can be inferred that the system was only able to reach the desired reference position in Case 1. Regarding the tilt commands in Fig. 8.3, it is observed that, for Case 1, α_1 and α_2 are driven to an equilibrium condition different from zero. On the other hand in Cases 2,3 and 4 the TRBC presented an oscillatory response in θ_1 and $\dot{\theta}_1$. Even though the system has presented a non-convergent behavior, by looking at Fig. 8.3 it can be noted that the MPC was able to enforce the command constraints between $\mathbf{u}_{max}$ and $\mathbf{u}_{min}$.

As a consequence of the θ_1 and θ_4 decoupling strategy, the system does not present any displacement in θ_4 direction in Cases 1,2 and 3. Despite that, for Case 4, the TRBC has presented oscillations in θ_4 which can be attributed to the noisy condition of the IMU reading. As a result, the motors were demanded for attitude regulation.

It is worth mentioning that the tilt mechanism dynamic behavior clearly have an influence in control stability. Moreover, from Fig. 8.2, it can be concluded that the experiment result nearly matches Case 2 model. Therefore, it indicates that θ_1 dynamics cannot be simply modeled as a first order differential equation neglecting the effective tilt angle position. As a result, due to the model mismatch, the MPC is not able to drive the states to a steady state condition, independently of the tuning parameters.

The above mentioned considerations suggests that the tilt dynamics may be considered in the MPC internal model in order to include all significant dynamics in the receding horizon. This could be done by assuming either the a third order θ_1 identified model or including the second order tilt dynamic model in the predictions. Nevertheless, for this particular problem, both approaches encounters some practical limitations. For the first one, if $\ddot{\theta}_1$ was to be included in the model, this state could not be directly measured. Consequently, the system observability is affected in a manner that a state observer cannot be designed. In the second case, χ_α can be included in the model as states, as previously discussed in Section 8.1. For this approach, if one assume that the identified model is reliable, a state observer can be designed assuming high values in $\mathbf{Q}_{obs}$ α related weights. Additionally, by including the tilt effectiveness as model state variables, the dissimilarity between α_1 and α_2 dynamics can be included in the model. For the previously mentioned reasons, the second strategy is adopted in this study.

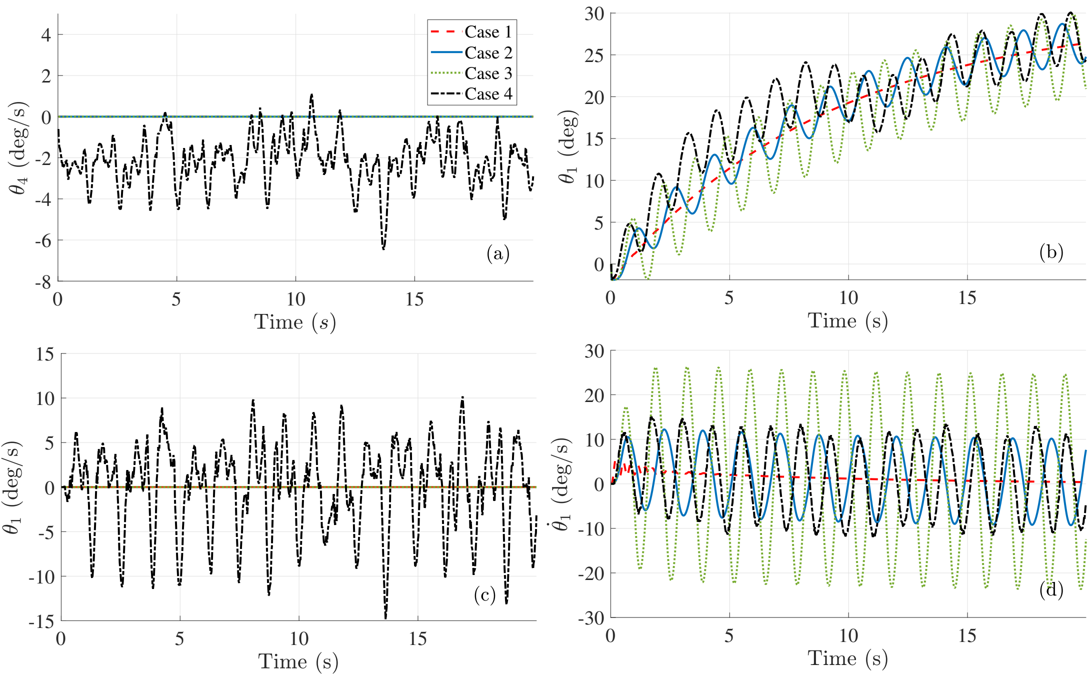

mo

Figure 8.2: TRBC lateral response comparison for $\theta_{1ref} = 30\ (deg)$.

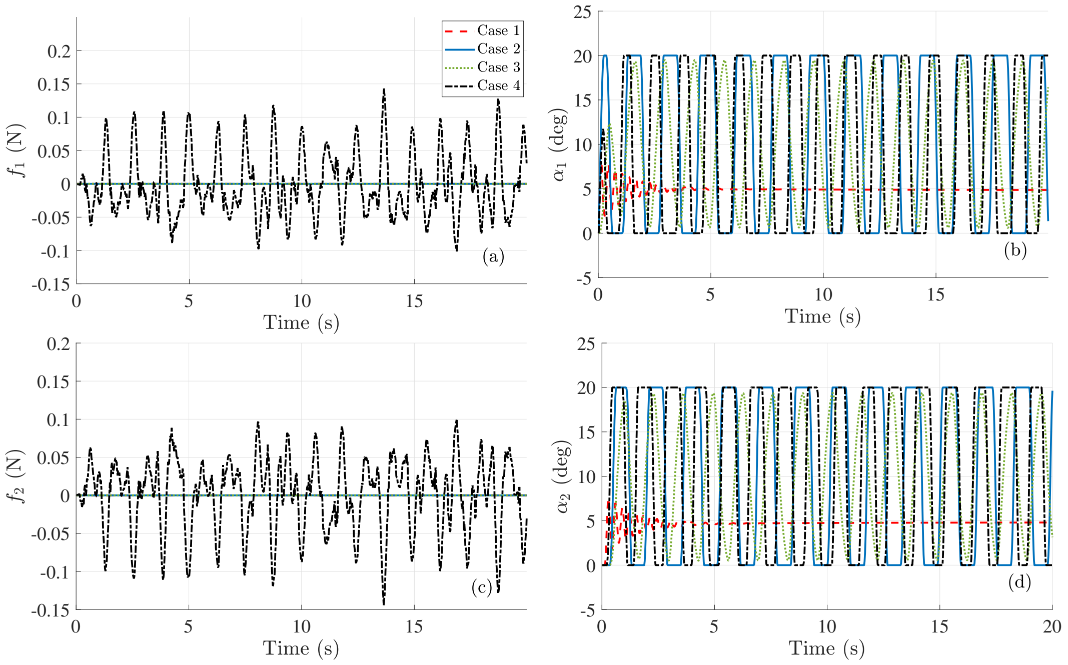

Figure 8.3: TRBC control inputs comparison for $\theta_{1ref} = 30\ (deg)$.

8.5.2 TRBC Full Control

From the lateral control experimental analysis, one can conclude that the TRBC dynamics definitely poses some obstacles toward the MPC experimental implementation concerning position tracking control. For instance, designing the MPC neglecting the actuator response results in model mismatch culminating in wrong state predictions. As a result, the system may present unexpected behavior due to the "unseen" dynamics.

In this sense, this section leans on the formulation presented in Sections 8.1 to 8.4 for the experimental evaluation of TRBC decoupled model control using MPC. The control task consists of tracking the same reference position from Section 7.3. More precisely, it is considered a constant reference signal of $\theta_{2ref} = 20\ [deg]$ for $t > 0\ [s]$ and $\theta_{1ref} = 10\ [deg]$ for $t > 10\ [s]$, as presented in Fig. 7.5. Aiming to use a representative model in the design process, the lateral LTI model described in Eq. (8.14), which includes the tilt dynamics, is considered. Moreover, the experimentally estimated properties from Table 6.1 are adopted while a sample time of $T_s = 0.02\ [s]$ is assumed to obtain the altitude, attitude and lateral models.

In summary, the TRBC controller is designed taking four steps. First, the inner loop attitude regulator is tuned with the same parameters as in Section 7.2 obtaining Eq. (7.15). The second step is carried out by tuning the altitude controller. Differently from the strategy presented in Marques et al. (2020) herein, θ_2 is controlled by an external loop. Taking advantage of the LQT experiment results, $\mathbf{K}_{alt}$ is calculated solving Riccati equation using model (8.24) with $\mathbf{Q}_{kalt} = diag([1\ 1.2\ 0.1])$ and $\mathbf{R}_{kalt} = diag([0.7\ 0.7])$. Therefore,

$$\mathbf{K}_{xalt} = \begin{bmatrix} 1.7888 & 1.3201 \\ 1.7888 & 1.3201 \end{bmatrix} \quad \text{and} \quad \mathbf{K}_{1alt} = \begin{bmatrix} 0.82525 \\ 0.82525 \end{bmatrix}$$

The third step consists of calculating the state observer gain matrix as presented in Section 8.2. The optimally designed observer gain is determined adopting $\mathbf{Q}_{obs} = diag([0.01\ 0.01$

20 10 20 10 10^3 10^3 10^3 10^3]) and $\mathbf{R}_{obs} = diag([5\ 10\ 1\ 1\ 1\ 1])$ which leads to $\mathbf{L}_{obs}$.

Following the design procedure, the last step is to obtain the MPC prediction matrices. They are estimated from the system discrete state space model (8.14) and assuming that $\mathbf{Q}_{mpc} = diag([3\ 0.4])$ and $\mathbf{R}_{mpc} = diag([0.2\ 0.2])$. Additionally, the restrictions from (8.34) were maintained while prediction horizons were set as $N_x = 18$ and $N_u = 6$.

At this point, it must be pointed out that the choice of the prediction horizon becomes a trade-off between computational processing and system performance. One may consider that, for control stability purposes, the *qpOASES* processing time, i.e. the time spent to calculate the optimum input sequence in the micro-controller, must be fitted in the sample interval T_s in order to avoid system delays. Notwithstanding, considering the BeagleBone computational limitations, if N_x and N_u are significantly increased, the prediction matrices will assume large dimensions, increasing the computational burden to solve the quadratic programming optimization. A possible solution for this matter is to increase T_s. However, if that is the case, the sample frequency may not be sufficient to represent the system behavior. Therefore, in this study, the prediction horizons were taken based on the maximum values of N_x and N_u which guarantees that $T_e < T_s$. Being T_e the time elapsed at each TRBC control routine iteration including the control solution, sensor reading, actuator command designation and data processing. It is worth mentioning that the prediction matrices, control gains and the system parameters (sample time, reference input, number of iterations) are generated in Matlab environment ans saved in *.txt* files. Then, the files can be loaded by the embedded code every time the experiment algorithm is executed.

The experimental results for the TRBC control task considering the decoupled dynamics and the lateral movement controlled by the MPC are depicted in Figs. 8.4, 8.5 and 8.6. As a figure of merit of the proposed control formulation, the obtained results are compared with those from the LQT experiment with tilt rotors presented in Section 7.3. As can be seen in Fig.8.4, the TRBC was able to track the desired reference signal satisfactorily. Additionally, the controller was properly able to handle α_1 and α_2 in order to respect the imposed constraints as shown in Fig. 8.6. From the figure, it can be observed that the tilt deflections respects the lower and upper boundary reaching the maximum and minimum values at $t = [0.36\ 14.1]$ $[s]$ and $t = [0.6\ 14.04]$ $[s]$, respectively.

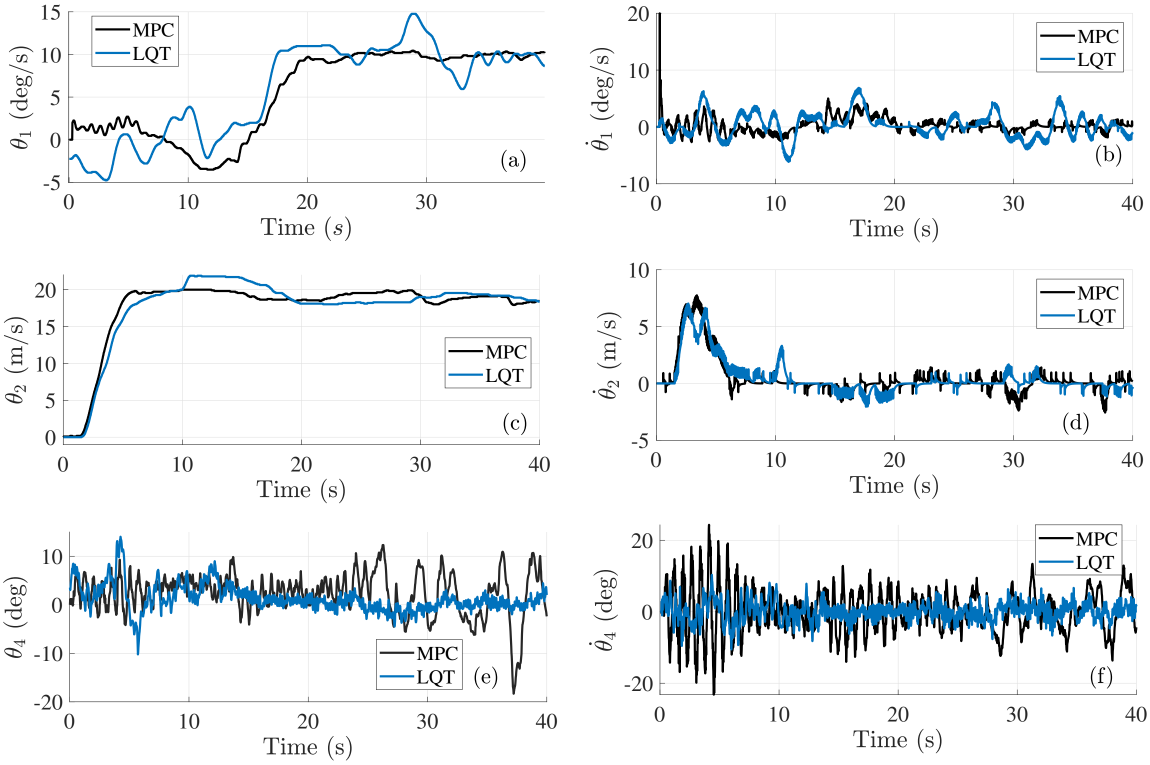

Figure 8.4: TRBC response using LQT controller and the decoupled strategy.

Now, comparing the data from the two experiments, some similarities and discrepancies can be pointed out. To begin with, the vehicle response in θ_2 direction are very similar in both cases. The system is able to reach the desired reference position with a overdamped system characteristic.

For the attitude response, the system has presented lower oscillations for the LQT. This behavior can be associated with the fact that, for the LQT case, the controller is designed with the complete model with coupled dynamics. As a result, the control gain matrix terms associated with θ_4 and θ_1 are calculated in order to attenuate the effect of attitude in horizontal

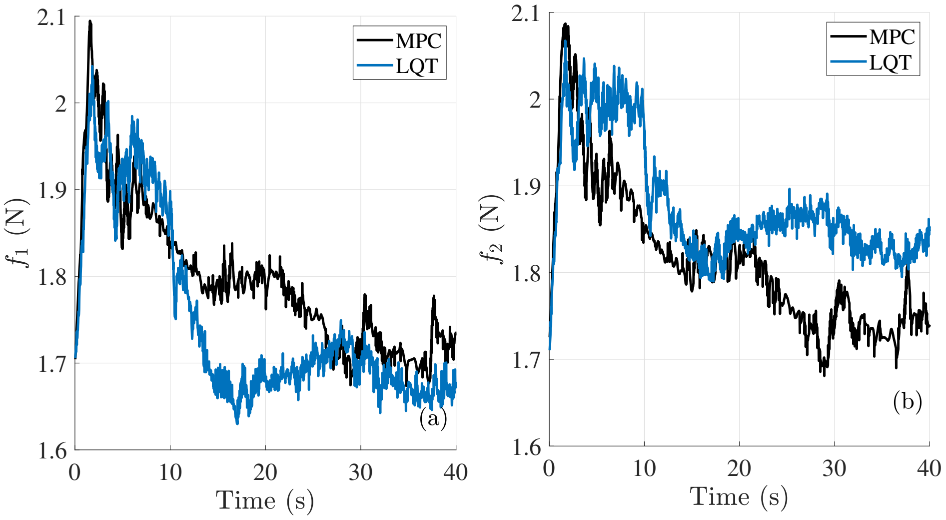

Figure 8.5: TRBC calculated motor thrust using LQT controller and the decoupled strategy.

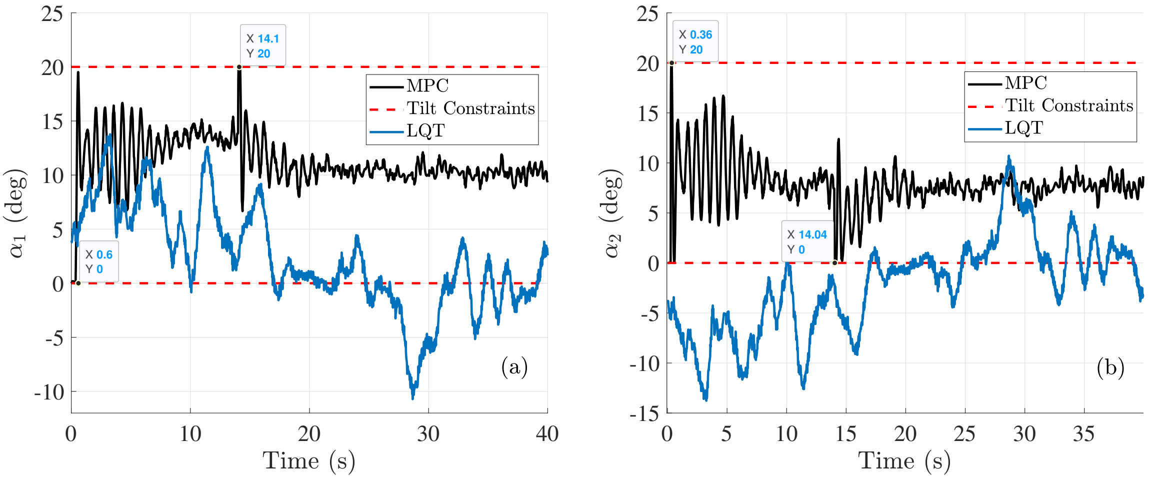

Figure 8.6: TRBC calculated tilt deflections using LQT controller and the decoupled strategy.

displacement. Moreover, the vehicle is able to use the motor thrust to shift its horizontal position and regulate θ_4. As a consequence, the LQT response performance is linked to the control coupling between θ_4 and θ_1 which can be verified by the motors response in $0 \leq t \leq 10$ $[s]$ in Fig. 8.5.

Despite that, the TRBC with MPC horizontal controller exhibited a better response compared to the LQT. As can be seen in Fig. 8.4 (a) and (b), the MPC presented a smoother trajectory, with lower oscillations in θ_1 and lower tracking error. In summary, the improvement can be attributed to a series of elements: the MPC better model representation, the state observer filtering properties, the ability of the controller to forecast the dynamics with future state predictions and the control decoupling between attitude and horizontal displacement. For instance, one advantage of the proposed formulation is that $\dot{\theta}_1$ is included in the cost function as a desired tracking state. As a result, the controller is able to act in response to the horizontal velocity when tracking θ_1. In addition, since the MPC has no authority over θ_4 regulation, the IMU noise effect over lateral control performance is reduced.

Among the discrepancies between the two experiments, the most prominent is the tilt deflection inputs calculated by the controller. As can be seen in Fig. 8.6, for the LQT experiment, the controller calculated tilt deflections beyond the servomechanism limitations. Additionally, the LQT has shown to be more conservative in α amplitudes. In this case, the controller has authority to manipulate the thrust force and tilt deflection to track θ_1 so that a balance between these two commands are achieved by the controller. The MPC, in contrast, was able to handle the commanded signal within the tilt constraints allowing the mechanism to operate on its limits during the transient phase. It must be noted that, differently from the LQT, for the MPC test, α_1 and α_2 were not driven to zero in steady state. This can be explained by the fact that the cost function (8.28) is written in terms of control increments and not the total input. Therefore, the system can be driven to any equilibrium condition where $\mathbf{y} \to 0$ and $\Delta\mathbf{u} \to 0$.

The last MPC experiment metric evaluated concerns the embedded software performance. As previously discussed, the *qpOASES* running time depends on the size of the quadratic programming matrices which increases with the number of prediction horizon. Hence, the time elapsed (T_e) for each control iteration was monitored as is depicted in Fig. 8.7. As can be noticed, the average control algorithm running time was $T_e = 6.224$ $[ms]$, that is 68.8% lower than the sample time (T_s). The only exception, where $T_e > T_s$, is the first iteration when the *qpOASES* initiate the quadratic programming problem. In conclusion, one can assume that

N_x and N_u are properly selected providing good tracking performance and avoiding system delays.

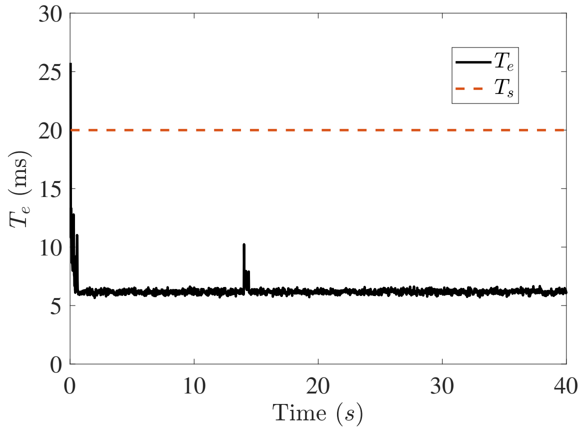

Figure 8.7: Time elapsed for each control iteration.

8.6 Chapter Summary

- By enabling the tilt-deflection DOF, it is possible to decouple the control hierarchy of the lateral motion. For instance, attitude and vertical position can be controlled by the motor thrust variation while the tilt deflection can be used to track lateral position. The major benefit of this approach is the possibility of tracking desired positions while holding constant attitude.

- Considering the test-bench scenario, where the goal is to drive the TRBC to a desired position while enforcing tilt deflection constraints, the MPC formulation is assumed as a good candidate for the lateral control design. In addition, attitude can be regulated by a LQR inner controller while the altitude position is tracked by an external LQT policy.

- Experimental results have shown that, differently from the LQR controller, the MPC highly depends on the prediction model fidelity. It was observed that the system does not present an stable response if

  1. The tilt mechanism dynamics are not included in the model as state variables;

2. The experimentally identified model parameters are not considered;
3. Tilts 1 and 2 dynamics are considered as the same, i.e. if $ef_{\alpha 1} = ef_{\alpha 2}$.

- After obtaining a representative model, the MPC based architecture has shown a better lateral response when compared to the LQT formulation. In special, the controller was able to request more deflection from the tilt actuators enforcing the constraints limitations. Moreover, the TRBC oscillations in θ_1 direction was also reduced

CHAPTER IX

Final Remarks

This section provides the final conclusions, discussions and general remarks about the presented study. It also gives a perspective of future improvements and research branches which can be derived from the proposed methodology.

9.1 General Remarks

This work addressed the study of tilt-rotor multi-copters by dynamic and control perspectives. The approach was motivated by the mechanism problematic in terms of the trade off between mechanical complexity and control performance. In order to illustrate this context, two control strategies were implemented for a position tracking task. One based on Modern Control techniques, where all the states and control inputs are under the responsibility of a single MIMO controller. In the second, the controller is decoupled in attitude, altitude and lateral motion. Then, a MPC based control strategy is employed for lateral control considering only the tilt angle as input command. In this case, the controller is designed in order to track a desired reference signal but also to enforce input constraints based on the tilt deflection limitations.

The experimental validation of the control law architecture demanded the development of a proper apparatus. Under those circumstances, it was proposed the design an construction of a tilt-rotor bi-copter test bench for control test systematization. The project involved the CAD design, construction, integration and software implementation of all subsystems in order to make the prototype operational. Additionally, the dynamic modelling and system identification were part of the post construction analysis. The prototype assembly has not only required control related competencies but also increased the study challenge.

For instance, in Chapter 6 was presented the identification of all the test bench degrees of freedom. From the results, it can be seen that the system has some particularities. All the identification procedures have demonstrated discrepancies between the model properties calculated from the virtual model and the identified parameters. To begin with, the joint friction, which are difficult to estimate from physical principles, has a major influence over the system behavior. Moreover, the system has a different responses for θ_1 positive and negative directions. In addition, the distance between joint 4 and the TRBC CG induces the vehicle to respond as a pendulum in θ_4 direction.

Through the study, it was also presented the actuators dynamics identification which have an impact over control performance. The identification experiments have shown that motors and tilt mechanisms have distinct dynamic models and that the tilt effectiveness is different for θ_1 directions. The actuation system response characteristics makes the test bench response susceptible to the interference of the tilt mechanism dynamics based on their open-loop poles proximity. As a result, these dissimilarities can be accounted for the control design as model uncertainties which are related to the controller robustness.

The proposed control formulations were tested by means of simulations and experimental tests. In the first case, the non-linear test-bench equations of motion were numerically implemented in Matlab environment. The second uses the test bench apparatus. As a first approach, the LQT controller performance was compared considering both scenarios. The analysis evidenced the discrepancies between calculated and identified model parameters. Despite that, the controller was robust enough to drive the system to stability. In a second plan, the TRBC controllabity was evaluated by comparing the system response with fixed and tilt-rotor configurations. The results have shown that when the tilt DOF are enabled, the TRBC presented smaller oscillations in attitude (θ_4). As a consequence, the system exhibited better tracking performance in lateral (θ_1) direction. This can be explained by the fact that the vehicle does not require to change attitude in order to move laterally.

Aiming to explore the lateral controllability improvement by adding the tilt-rotor degree of freedom, a novel control policy was proposed. The strategy is to use the tilt-deflection to track lateral reference position while vertical and attitude control is achieved by varying the motor thrust force. Under those circumstances, the MPC has shown to be appropriate for lateral motion considering control performance and the capability to enforce constraints over tilt deflections. When implemented in the test bench, the formulation has presented appealing results in terms of control performance and constraint handling. However, the system has only had an stable response when the tilt dynamic model was included in the MPC prediction model. As a consequence, the dependence of a reliable model, added to the number of design variables inherent to the MPC control design, impose some hardships throughout the control tuning process.

9.2 Future Perspectives

The development of this study can be seen as a basis for multi-copter control studies. In special, the development of a proper apparatus for test systematization in safe conditions is a prominent asset for the recently created AFL and control classes. For instance, other control techniques can be designed, implemented and tested with relative readiness. From classical control theory to AI based formulations. Moreover, other tilt-rotor configurations and motor configurations - e.g. lateral tilt deflection, coaxial motors, tri-copters, etc - can be experimented. Additionally, the test bench DOF can be increased by replacing joint 4 by an spherical joint.

Nevertheless, the prototype has some operational limitations. From experiment observations, some major adversities could be pointed out. As an example, the IMU signal quality imposed some obstacles and compromised control performance. Even though this is a common issue on multi-copters, the sensor could be replaced by a rotary encoder in order to reduce signal noise. Moreover, there are some mechanical flaws as misalignment, cracks and vibration (specially in the motor bed) which affects the system. The motors could also be replaced by more reliable devices. From the model perspective, more system identification experiments can be carried out in order to better estimate system parameters and have a more accurate dynamic model. In conclusion, all the above mentioned peculiarities can be improved for future researches.

Appendix A

Prediction Model

Herein, a methodology to solve the predictive control problem is presented based on Maciejowski (2002). In this case, it is assumed a LTI state space model, written in discrete time domain as

$$\mathbf{x}(k+1) = \mathbf{A}\mathbf{x}(k) + \mathbf{B}\mathbf{u}(k) \tag{A.1}$$

$$\mathbf{y}(k) = \mathbf{C}\mathbf{x}(k) \tag{A.2}$$

where $\mathbf{x}$ is a n_s-dimensional state vector, $\mathbf{u}$ is a n_y-dimensional input vector and $\mathbf{y}$ is a n_s-dimensional vector of outputs which are to be controlled.

- **Obtaining the state and output prediction model**

The idea is to compute the predicted values of the controlled variables ($\hat{\mathbf{y}}(k+i|k)$), from the estimates of the current state ($\hat{\mathbf{x}}(k|k)$), the assumed inputs, or equivalently, the latest inputs ($\mathbf{u}(k-i)$) and the future input changes ($\Delta\hat{\mathbf{y}}(k+i|k)$). In order to accomplish this, it is assumed that all the state variables are available. Therefore, the model future state vector can be predicted by iterating (A.1). For the first iteration at sample k, writing the system state $\mathbf{x}$ in terms of predicted variables, one obtain

$$\hat{\mathbf{x}}(k+1|k) = \mathbf{A}\mathbf{x}(k) + \mathbf{B}\hat{\mathbf{u}}(k|k) \tag{A.3}$$

For two future steps

$$\hat{\mathbf{x}}(k+2|k) = \mathbf{A}\hat{\mathbf{x}}(k+1|k) + \mathbf{B}\hat{\mathbf{u}}(k+1|k) \tag{A.4}$$

Substituting (A.3) in (A.4) results in

$$\hat{\mathbf{x}}(k+2|k) = \mathbf{A}^2\mathbf{x}(k) + \mathbf{A}\mathbf{B}\hat{\mathbf{u}}(k|k) + \mathbf{B}\hat{\mathbf{u}}(k|k) \tag{A.5}$$

Analogously, for *i* future samples:

$$\hat{\mathbf{x}}(k+i|k) = \mathbf{A}^i\mathbf{x}(k) + \mathbf{A}^{i-1}\mathbf{B}\hat{\mathbf{u}}(k|k) + \mathbf{A}^{i-2}\mathbf{B}\hat{\mathbf{u}}(k+1|k) + \cdots + \mathbf{B}\hat{\mathbf{u}}(k+i-1|k) \tag{A.6}$$

Arranging the predictions for N_x steps ahead in matrix format

$$\begin{bmatrix} \hat{\mathbf{x}}(k+1|k) \\ \hat{\mathbf{x}}(k+2|k) \\ \vdots \\ \hat{\mathbf{x}}(k+N_x|k) \end{bmatrix} = \begin{bmatrix} \mathbf{A} \\ \mathbf{A}^2 \\ \vdots \\ \mathbf{A}^{N_x} \end{bmatrix} \mathbf{x}(k) + \begin{bmatrix} \mathbf{B} & 0_{n_s\times n_u} & \dots & 0_{n_s\times n_u} \\ \mathbf{A}\mathbf{B} & \mathbf{B} & \dots & 0_{n_s\times n_u} \\ \vdots & \vdots & \ddots & \vdots \\ \mathbf{A}^{N_x-1}\mathbf{B} & \mathbf{A}^{N_x-2}\mathbf{B} & \dots & \mathbf{B} \end{bmatrix} \begin{bmatrix} \hat{\mathbf{u}}(k|k) \\ \hat{\mathbf{u}}(k+1|k) \\ \vdots \\ \hat{\mathbf{u}}(k+N_x-1|k) \end{bmatrix} \tag{A.7}$$

being $\mathbf{0}_{n_x\times n_u} \in \mathbb{R}^{(n_x\times n_u)}$ a vector of zeros.

In summary, by using Eq. (A.7) it is possible to define the future states N_x steps for a given initial states at sample k and a sequence of control inputs $\hat{\mathbf{u}}(k|k)$. Moreover, Eq. (A.7) can be succinctly represented as

$$\hat{\mathbf{X}} = \mathbf{P}_x \mathbf{x}(k) + \mathbf{H}_x \hat{\mathbf{U}} \tag{A.8}$$

A similar procedure can be adopted to describe the future prediction of the control outputs $\hat{\mathbf{y}}$. In this sense, (A.2) is written in terms of the predicted variables as

$$\hat{\mathbf{y}}(k+1|k) = \mathbf{C}\hat{\mathbf{x}}(k+1|k) \tag{A.9}$$

Now, substituting (A.4) in (A.9) the output predictions can be written in terms of the the states at sample k and the input command sequence $\hat{\mathbf{u}}(k|k)$ as

$$\hat{\mathbf{y}}(k+1|k) = \mathbf{CAx}(k) + \mathbf{CB}\hat{\mathbf{u}}(k|k) \tag{A.10}$$

Following the same procedure for two and i steps ahead one can obtain

$$\hat{\mathbf{y}}(k+2|k) = \mathbf{CA}^2\mathbf{x}(k) + \mathbf{CAB}\hat{\mathbf{u}}(k|k) + \mathbf{CB}\hat{\mathbf{u}}(k+1|k) \tag{A.11}$$

$$\hat{\mathbf{y}}(k+i|k) = \mathbf{CA}^i\mathbf{x}(k) + \mathbf{CA}^{i-1}\mathbf{B}\hat{\mathbf{u}}(k|k) + \mathbf{CA}^{i-2}\mathbf{B}\hat{\mathbf{u}}(k+1|k) + \cdots + \mathbf{CB}\hat{\mathbf{u}}(k+i-1|k) \tag{A.12}$$

Writing the predictions for N_x steps ahead in the matrix format

$$\begin{bmatrix} \hat{\mathbf{y}}(k+1|k) \\ \hat{\mathbf{y}}(k+2|k) \\ \vdots \\ \hat{\mathbf{y}}(k+N_x|k) \end{bmatrix} = \begin{bmatrix} \mathbf{CA} \\ \mathbf{CA}^2 \\ \vdots \\ \mathbf{CA}^{N_x} \end{bmatrix} \mathbf{x}(k) + \begin{bmatrix} \mathbf{CB} & 0_{n_y \times n_u} & \dots & 0_{n_y \times n_u} \\ \mathbf{CAB} & \mathbf{CB} & \dots & 0_{n_y \times n_u} \\ \vdots & \vdots & \ddots & \vdots \\ \mathbf{CA}^{N_x-1}\mathbf{B} & \mathbf{CA}^{N_x-2}\mathbf{B} & \dots & \mathbf{CB} \end{bmatrix} \begin{bmatrix} \hat{\mathbf{u}}(k+k|k) \\ \hat{\mathbf{u}}(k+1|k) \\ \vdots \\ \hat{\mathbf{u}}(k+N_x-1|k) \end{bmatrix} \tag{A.13}$$

or, in a compact matrix format,

$$\hat{\mathbf{Y}} = \mathbf{f}_y + \mathbf{H}_y \hat{\mathbf{U}} \tag{A.14}$$

• **Writing the predictions in terms of control increments**

Among different methodologies to express the prediction model in terms of control increment, one possibility consists of using an artificial state defined as

$$\boldsymbol{\xi}(k) = \begin{bmatrix} \mathbf{x}(k) \\ \mathbf{u}(k-1) \end{bmatrix} \tag{A.15}$$

Given that, from (A.1), (A.3) and (A.15), one can define an artificial model in terms of the control increments

$$\boldsymbol{\xi}(k) = \begin{bmatrix} \mathbf{x}(k) \\ \mathbf{u}(k) \end{bmatrix} = \begin{bmatrix} \mathbf{A} & \mathbf{B} \\ 0_{n_u \times n_x} & \mathbf{I}_{n_u} \end{bmatrix} \begin{bmatrix} \mathbf{x}(k) \\ \mathbf{u}(k-1) \end{bmatrix} + \begin{bmatrix} \mathbf{B} \\ \mathbf{I}_{n_u} \end{bmatrix} \Delta\mathbf{u}(k) \tag{A.16}$$

$$\mathbf{y}(k) = \begin{bmatrix} \mathbf{C}\ 0_{n_y \times n_x} \end{bmatrix} \begin{bmatrix} \mathbf{x}(k) \\ \mathbf{u}(k-1) \end{bmatrix} \tag{A.17}$$

which is equivalent to

$$\boldsymbol{\xi}(k+1) = \mathbf{A}\boldsymbol{\xi}(k) + \mathbf{B}\Delta\mathbf{u}(k) \tag{A.18}$$

$$\mathbf{y}(k) = \mathbf{C}\boldsymbol{\xi}(k) \tag{A.19}$$

Then, writing (A.14) in terms of the artificial model (A.18) a prediction model of the system outputs ($\hat{\mathbf{Y}}$) can be written in terms of the control increment sequence $\Delta\hat{\mathbf{U}}$ as

$$\hat{\mathbf{Y}} = \mathbf{f} + \mathbf{G}\Delta\hat{\mathbf{U}} \tag{A.20}$$

where

$$\mathbf{G} = \begin{bmatrix} \mathbf{CB} & 0_{n_y \times n_u} & \cdots & 0_{n_y \times n_u} \\ \mathbf{CAB} & \mathbf{CB} & \cdots & 0_{n_y \times n_u} \\ \vdots & \vdots & \ddots & \vdots \\ \mathbf{CA}^{N_x-1}\mathbf{B} & \mathbf{CA}^{N_x-2}\mathbf{B} & \dots & \mathbf{CA}^{N_x-N_u}\mathbf{B} \end{bmatrix} \quad , \ \mathbf{f} = \phi\boldsymbol{\xi}(k) \quad , \ \phi = \begin{bmatrix} \mathbf{CA} \\ \mathbf{CA}^2 \\ \vdots \\ \mathbf{CA}^{N_x} \end{bmatrix} \tag{A.21}$$

One may note that, in (A.21), the last $(N_x - N_u)n_x$ columns of are suppressed from $\mathbf{G}$

due to the input increment horizon restrictions. In this case, N_u denotes the input prediction horizon which is typically smaller than N_x.

Appendix B

Control Action Constrains Prediction

In this section, the state-space model from Appendix A, presented in Eqs. (A.1) and (A.2), is assumed considering that $\mathbf{x}$ and $\mathbf{u}$ are the state and control action vectors, respectively. Hence, the restrictions over the control actions can be described as:

$$\mathbf{u}_{min} \leq \hat{\mathbf{u}}(k-1+i|k) \leq \mathbf{u}_{max}\ , \quad i \in \{1,\ldots,N_x\} \tag{A.1}$$

where $\mathbf{u}_{min}$ and $\mathbf{u}_{max}$ are the minimum and maximum control action values which can be assumed by the system. In general, these variables are related with physical limitations of the actuators. Now, writing (A.1) in matrix format

$$\begin{bmatrix} \mathbf{u}_{min} \\ \mathbf{u}_{min} \\ \vdots \\ \mathbf{u}_{min} \end{bmatrix} \leq \begin{bmatrix} \hat{\mathbf{u}}(k|k) \\ \hat{\mathbf{u}}(k+1|k) \\ \vdots \\ \hat{\mathbf{u}}(k+N_x-1|k) \end{bmatrix} \leq \begin{bmatrix} \mathbf{u}_{max} \\ \mathbf{u}_{max} \\ \vdots \\ \mathbf{u}_{max} \end{bmatrix} \tag{A.2}$$

Assuming that, as presented in Section 8.1, the controller is composed by an inner loop regulator with a control law described by

$$\mathbf{u}_{lqr} = -\mathbf{K}_{lqr}\mathbf{x}_{lqr} \tag{A.3}$$

where $\mathbf{x}_{lqr}$ is the vector containing q regulated states , $\mathbf{u}_{lqr}$ comprises the r control action variables associated with $\mathbf{x}_{lqr}$ states and $\mathbf{K}_{lqr}$ is the control gain matrix determined by the LQR solution. Then, taking into account Eq. (A.3), the total control command can be written as $\mathbf{u}_t = \mathbf{u}_{lqr} + \mathbf{u}$, being $\mathbf{u}$ the MPC calculated control action, consequently

$$\mathbf{u}_t = -[\mathbf{K}_{lqr}\ \mathbf{0}_{(n_x-q)\times r)}] \begin{bmatrix} \mathbf{x}_{lqr} \\ \mathbf{x}_o \end{bmatrix} + \mathbf{u} = -\mathbf{K}\mathbf{x} + \mathbf{u} \tag{A.4}$$

where $\mathbf{x}_o$ are the states which are not regulated by the LQR.

At this point, it must be emphasized that the choice of the input variables can affect the manner the MPC deals with the cost function minimization and constraints. For instance, in Section 8.1, the system dynamics were decoupled in a fashion that the MPC only control the tilting angles while the LQR and LQT controllers manipulate the motor thrust. In this case, the MPC and LQR inputs become independent and, therefore, their contributions are not summed up. Meanwhile, if the complete model is considered in the inner loop, i.e. all the states are regulated through the LQR controller using tilt angles an motor thrust, the control action will be a result of the LQR and MPC contributions. Herein, the constraints prediction formulation is presented considering the most generic case were the LQR and MPC can handle motor thrust and tilt deflections. Then, the model can be particularized for the TRBC application.

Now, writing (A.3) using the prediction notation

$$\hat{\mathbf{u}}_{lqr}(k-1+i|k) = -\mathbf{K}\hat{\mathbf{x}}(k-1+i|k)\ , \quad i \in \{1,\ldots,N_x\} \tag{A.5}$$

or in the matrix format

$$\begin{bmatrix} \hat{\mathbf{u}}_{lqr}(k|k) \\ \hat{\mathbf{u}}_{lqr}(k+1|k) \\ \vdots \\ \hat{\mathbf{u}}_{lqr}(k+N_x-1|k) \end{bmatrix} = \begin{bmatrix} -\mathbf{K} \\ \mathbf{0}_{n_u \times n_x} \\ \vdots \\ \mathbf{0}_{n_u \times n_x} \end{bmatrix} \mathbf{x}(k) + \begin{bmatrix} \mathbf{0}_{n_u \times n_x} & \dots & \mathbf{0}_{n_u \times n_x} & \mathbf{0}_{n_u \times n_x} \\ -\mathbf{K} & \dots & \mathbf{0}_{n_u \times n_x} & \mathbf{0}_{n_u \times n_x} \\ \vdots & \ddots & \vdots & \vdots \\ \mathbf{0}_{n_u \times n_x} & \dots & -\mathbf{K} & \mathbf{0}_{n_u \times n_x} \end{bmatrix} \begin{bmatrix} \hat{\mathbf{x}}(k|k) \\ \hat{\mathbf{x}}(k+1|k) \\ \vdots \\ \hat{\mathbf{x}}(k+N_x|k) \end{bmatrix} \tag{A.6}$$

Following the formulation, one can write

$$\hat{\mathbf{U}}_{lqr} = \mathbf{P}_{lqr}\mathbf{x}(k) + \mathbf{H}_{lqr}\hat{\mathbf{X}} \tag{A.7}$$

Similarly, for the MPC contribution

$$\hat{\mathbf{U}} = \begin{bmatrix} \hat{\mathbf{u}}(k|k) \\ \hat{\mathbf{u}}(k+1|k) \\ \vdots \\ \hat{\mathbf{u}}(k+N_x-1|k) \end{bmatrix} \tag{A.8}$$

Therefore, the total control action prediction model can be derived combining Eqs. (A.8), (A.7) and (A.8)

$$\hat{\mathbf{U}}_t = (\mathbf{P}_{lqr} + \mathbf{H}_{lqr}\mathbf{P}_x)\mathbf{x}(k) + (\mathbf{H}_{lqr}\mathbf{H}_x + \mathbf{I}_{(n_u \cdot N_x)})\hat{\mathbf{U}} \tag{A.9}$$

where $\mathbf{I}_{n_u \cdot N_x} \in \mathrm{R}^{n_u \cdot N_x \times n_u \cdot N_x}$ identity matrix.

In summary,

$$\hat{\mathbf{U}}_t = \mathbf{P}_u \mathbf{x}(k) + \mathbf{H}_u \hat{\mathbf{U}} \tag{A.10}$$

The predicted control inputs can be obtained writing the control variation (**Δu**) in terms of the predicted variables as follows

$$\begin{aligned} \hat{\mathbf{u}}(k+i-1|k) = \; & \mathbf{u}(k-1) + \Delta\hat{\mathbf{u}}(k|k) + \Delta\hat{\mathbf{u}}(k+1|k) \\ & + \cdots + \Delta\hat{\mathbf{u}}(k+i-1|k) \; , \quad i = 1,\ 2, \ldots,\ N_x \end{aligned} \tag{A.11}$$

Putting (A.11) in matrix format

$$\begin{bmatrix} \hat{\mathbf{u}}(k|k) \\ \hat{\mathbf{u}}(k+1|k) \\ \vdots \\ \hat{\mathbf{u}}(k+N_x-1|k) \end{bmatrix} = \begin{bmatrix} \mathbf{u}(k-1) \\ \mathbf{u}(k-1) \\ \vdots \\ \mathbf{u}(k-1) \end{bmatrix} + \begin{bmatrix} \boldsymbol{I}_{n_u} & 0_{n_u} & \ldots & 0_{n_u} \\ \boldsymbol{I}_{n_u} & \boldsymbol{I}_{n_u} & \ldots & 0_{n_u} \\ \vdots & \vdots & \ddots & \vdots \\ \boldsymbol{I}_{n_u} & \boldsymbol{I}_{n_u} & \ldots & \boldsymbol{I}_{n_u} \end{bmatrix} \begin{bmatrix} \Delta\hat{\mathbf{u}}(k|k) \\ \Delta\hat{\mathbf{u}}(k+1|k) \\ \vdots \\ \Delta\hat{\mathbf{u}}(k+N_u-1|k) \end{bmatrix} \tag{A.12}$$

In other terms,

$$\hat{\mathbf{U}} = [\mathbf{u}(k-1)]_{N_x} + \mathbf{T}^{\mathbf{I}_{n_u}}_{N_x \times N_u} \Delta\hat{\mathbf{U}} \tag{A.13}$$

It is noteworthy that the last $(N_x - N_u)$ columns of $\mathbf{T}^{\mathbf{I}_{n_u}}_{N_x \times N_u}$ are suppressed if $\Delta\hat{\mathbf{u}}(k+i-1|k) = 0$ for $i = N_u + 1,\ N_u + 1, \ldots,\ N_x$. Then, the total control predictions in terms of the predictive control increments are obtained substituting (A.13) in (A.10) as follows

$$\hat{\mathbf{U}}_t = \mathbf{P}_u\mathbf{x}(k) + \mathbf{H}_u[\mathbf{u}(k-1)]_{N_x} + \mathbf{H}_u\mathbf{T}^{\mathbf{I}_{nu}}_{N_x\times N_u}\Delta\hat{\mathbf{U}} \tag{A.14}$$

Letting the total control input constraints be written as (A.14), and substituting it in (A.2)

$$\underbrace{\begin{bmatrix} \mathbf{u}_{t_{min}} \\ \mathbf{u}_{t_{min}} \\ \vdots \\ \mathbf{u}_{t_{min}} \end{bmatrix}}_{[\mathbf{u}_{min}]_{N_x}} \leq \mathbf{P}_u\mathbf{x}(k) + \mathbf{H}_u[\mathbf{u}(k-1)]_{N_x} + \mathbf{H}_u\mathbf{T}^{\mathbf{I}_{nu}}_{N_x\times N_u}\Delta\hat{\mathbf{U}} \leq \underbrace{\begin{bmatrix} \mathbf{u}_{t_{max}} \\ \mathbf{u}_{t_{max}} \\ \vdots \\ \mathbf{u}_{t_{max}} \end{bmatrix}}_{[\mathbf{u}_{max}]_{N_x}} \tag{A.15}$$

which can be rewritten as

$$\begin{bmatrix} \mathbf{H}_T \\ -\mathbf{H}_T \end{bmatrix} \Delta\hat{\mathbf{U}} \leq \begin{bmatrix} [\mathbf{u}_{max}]_{N_x} - \mathbf{H}_u[\mathbf{u}(k-1)]_{N_x} - \mathbf{f}_u \\ \mathbf{f}_u + \mathbf{H}_u[\mathbf{u}(k-1)]_{N_x} - [\mathbf{u}_{max}]_{N_x} \end{bmatrix} \tag{A.16}$$

where $\mathbf{H}_T = \mathbf{H}_u\mathbf{T}^{\mathbf{I}_{nu}}_{N_x\times N_u}\Delta\hat{\mathbf{U}}$ and $\mathbf{f}_u = \mathbf{P}_u\mathbf{x}(k)$.

As can be noted in Eq. (A.16), when writing the command constraints in terms of control increments, they become not only dependent on the maximum and minimum allowed control action ($[\mathbf{u}_{max}]_{N_x}$ and $[\mathbf{u}_{min}]_{N_x}$) but also on the last input command $\mathbf{u}(k-1)$. Additionally, by including the inner loop controller, they are function of the system actual states $\mathbf{x}(k)$. As a result, these constraints are updated at each time sample.

After describing the control restrictions in terms of $\Delta\hat{\mathbf{u}}$, those related with control increments constraints are still remaining to complement the constraint set. These are valuable when actuator dynamics are relevant to the system response. Then, one can define the total control increment constraints as

$$\Delta\mathbf{u}_{t_{min}} \leq \Delta\hat{\mathbf{u}}_t(k+i-1|k) \leq \Delta\mathbf{u}_{t_{max}}\ , \qquad i = 1,\ 2,\ \ldots,\ N_x \tag{A.17}$$

where $\Delta\mathbf{u}_{t_{min}}$ and $\Delta\mathbf{u}_{t_{max}}$ are the minimum and maximum allowed control increments, respectively.

Writing (A.17) in matrix format

$$\begin{bmatrix} \Delta\mathbf{u}_{t_{min}} \\ \Delta\mathbf{u}_{t_{min}} \\ \vdots \\ \Delta\mathbf{u}_{t_{min}} \end{bmatrix} \leq \begin{bmatrix} \Delta\hat{\mathbf{u}}_t(k|k) \\ \Delta\hat{\mathbf{u}}_t(k+1|k) \\ \vdots \\ \Delta\hat{\mathbf{u}}_t(k+N_u-1|k) \end{bmatrix} \leq \begin{bmatrix} \Delta\mathbf{u}_{t_{max}} \\ \Delta\mathbf{u}_{t_{max}} \\ \vdots \\ \Delta\mathbf{u}_{t_{max}} \end{bmatrix} \tag{A.18}$$

or, more concisely,

$$[\Delta\mathbf{u}_{t_{min}}]_{N_x} \leq \Delta\hat{\mathbf{U}}_t \leq [\Delta\mathbf{u}_{t_{max}}]_{N_x} \tag{A.19}$$

As a result, the total control increments predictions can be defined in terms of the predicted variables as

$$\hat{\mathbf{u}}_t(k|k) = \hat{\mathbf{u}}_t(k|k) - \mathbf{u}_t(k-1), \qquad i = 1 \tag{A.20}$$

$$\hat{\mathbf{u}}_t(k+i-1|k) = \mathbf{u}_t(k+i-1|k) - \mathbf{u}_t(k+i-2|k), \qquad i = 2,\ 3, \ldots,\ N_x \tag{A.21}$$

Rewriting the N_x terms of the total control increments, including the instantaneous sample time, in the matrix format

$$\begin{bmatrix} \Delta\hat{\mathbf{u}}_t(k|k) \\ \Delta\hat{\mathbf{u}}_t(k+1|k) \\ \vdots \\ \Delta\hat{\mathbf{u}}_t(k+N_u-1|k) \end{bmatrix} = \begin{bmatrix} \boldsymbol{I}_{n_u} & 0_{n_u} & \dots & 0_{n_u} & 0_{n_u} \\ -\boldsymbol{I}_{n_u} & \boldsymbol{I}_{n_u} & \dots & 0_{n_u} & 0_{n_u} \\ \vdots & \vdots & \ddots & \vdots & \vdots \\ 0_{n_u} & 0_{n_u} & \dots & -\boldsymbol{I}_{n_u} & \boldsymbol{I}_{n_u} \end{bmatrix} \begin{bmatrix} \hat{\mathbf{u}}_t(k|k) \\ \hat{\mathbf{u}}_t(k+1|k) \\ \vdots \\ \hat{\mathbf{u}}_t(k+N_u-1|k) \end{bmatrix} - \begin{bmatrix} \boldsymbol{I}_{n_u} \\ 0_{n_u} \\ \vdots \\ 0_{n_u} \end{bmatrix} \tag{A.22}$$

which yields

$$\Delta\hat{\mathbf{U}}_t = \mathbf{H}_I\hat{\mathbf{U}}_t - \mathbf{P}_I\mathbf{u}_t(k-1) \tag{A.23}$$

Now, substituting (A.14) in (A.23), the following predictions are obtained for the total control increments

$$\Delta\hat{\mathbf{U}}_t = \mathbf{H}_I\mathbf{P}_u\mathbf{x}(k) + \mathbf{H}_I\mathbf{H}_u\left[\mathbf{u}(k-1)\right]_{N_x} + \mathbf{H}_I\mathbf{H}_T\Delta\hat{\mathbf{U}} - \mathbf{P}_I\mathbf{u}_t(k-1) \tag{A.24}$$

which can be written succinctly as

$$\Delta\hat{\mathbf{U}}_t = \mathbf{f}_{\Delta u} - \mathbf{f}_I + \mathbf{H}_{\Delta u}\left[\mathbf{u}(k-1)\right]_{N_x} + \mathbf{H}_{IT}\Delta\hat{\mathbf{U}} \tag{A.25}$$

being $\mathbf{f}_{\Delta u} = \mathbf{H}_I\mathbf{P}_u\mathbf{x}(k)$, $\mathbf{f}_I = \mathbf{P}_I\mathbf{u}_t(k-1)$, $\mathbf{H}_{\Delta u} = \mathbf{H}_I\mathbf{H}_u$ and $\mathbf{H}_{IT} = \mathbf{H}_I\mathbf{H}_T$.

Thus, replacing $\Delta\hat{\mathbf{U}}_t$ by (A.25) in (A.19) results in

$$[\Delta \mathbf{u}_{t_{min}}]_{N_x} \leq \mathbf{f}_{\Delta u} - \mathbf{f}_I + \mathbf{H}_{\Delta u}\left[\mathbf{u}(k-1)\right]_{N_x} + \mathbf{H}_{IT}\Delta\hat{\mathbf{U}} \leq [\Delta \mathbf{u}_{t_{max}}]_{N_x} \tag{A.26}$$

Herein, one may note that in (A.26) the constraints are written in terms of the MPC decision variables ($\Delta\hat{\mathbf{U}}$) corresponding to the seeking solution of the minimization problem. Meanwhile, the boundaries are described by the maximum total allowed control increments which are, in fact, the actuator operational limitation.

Similarly to (A.16), (A.26) can be rearranged in matrix format as follows

$$\begin{bmatrix} \mathbf{H}_{IT} \\ -\mathbf{H}_{IT} \end{bmatrix} \Delta\hat{\mathbf{U}} \leq \begin{bmatrix} [\Delta \mathbf{u}_{t_{max}}]_{N_x} - \mathbf{f}_{\Delta u} + \mathbf{f}_I - \mathbf{H}_{\Delta u}\left[\mathbf{u}(k-1)\right]_{N_x} \\ \mathbf{f}_{\Delta u} - \mathbf{f}_I + \mathbf{H}_{\Delta u}\left[\mathbf{u}(k-1)\right]_{N_x} - [\Delta \mathbf{u}_{t_{min}}]_{N_x} \end{bmatrix} \tag{A.27}$$

Combining (A.16) and (A.27) in a single matrix system

$$\mathbf{A}_{qp}\Delta\hat{\mathbf{U}} \leq \mathbf{b}_{qp} \tag{A.28}$$

where

$$\mathbf{A}_{qp} = \begin{bmatrix} \mathbf{H}_{IT} \\ -\mathbf{H}_{IT} \\ \mathbf{H}_T \\ -\mathbf{H}_T \end{bmatrix} \quad \text{and} \quad \mathbf{b}_{qp} = \begin{bmatrix} [\Delta \mathbf{u}_{t_{max}}]_{N_x} - \mathbf{f}_{\Delta u} + \mathbf{f}_I - \mathbf{H}_{\Delta u}\left[\mathbf{u}(k-1)\right]_{N_x} \\ \mathbf{f}_{\Delta u} - \mathbf{f}_I + \mathbf{H}_{\Delta u}\left[\mathbf{u}(k-1)\right]_{N_x} - [\Delta \mathbf{u}_{t_{min}}]_{N_x} \\ [\mathbf{u}_{max}]_{N_x} - \mathbf{H}_u[\mathbf{u}(k-1)]_{N_x} - \mathbf{f}_u \\ \mathbf{f}_u + \mathbf{H}_u[\mathbf{u}(k-1)]_{N_x} - [\mathbf{u}_{max}]_{N_x} \end{bmatrix}$$

Wrapping up the presented formulation, Eq. (A.28) is a strategy to describe the input constraints as function of the decision vector $\Delta\hat{\mathbf{U}}$ solely. This condition is reasonable to be used as linear inequality constraints in quadratic programming minimization problem.

Bibliography

AGÊNCIA NACIONAL DE AVIAÇÃO CIVIL. *Regulamento Brasileiro da Aviação Civil Especial RBAC-E 94*: Requisitos gerais para aeronaves não tripuladas de uso civil. São Paulo, 2021.

ALEXIS, K.; NIKOLAKOPOULOS, G.; TZES, A. Switching model predictive attitude control for a quadrotor helicopter subject to atmospheric disturbances. *Control Engineering Practice*, Elsevier, v. 19, n. 10, p. 1195–1207, 2011. DOI:<https://doi.org/10.1016/j.conengprac.2011.06.010>.

ALMEIDA, F. A. D.; LEISSLING, D. Fault-tolerant flight control system using model predictive control. In: *Brazilian Symposium on Aerospace Engineering & Applications*. São José dos Campos, SP, Brazil: AAB, 2009.

ATHANS, M.; FALB, P. L. *Optimal Control: An introduction to the Theory and Its Applications*. New York: Dover Books on Engineering, 2006.

BACHMANN, R. et al. A biologically inspired micro-vehicle capable of aerial and terrestrial locomotion. *Mech. Theory*, n. 44, p. 513–526, 2009. DOI:<https://doi.org/10.1016/j.mechmachtheory.2008.08.008>.

BADR, S.; MEHREZ, O.; KABEEL, A. E. A novel modification for a quadrotor design. In: *2016 Int. Conf. on Unmanned Aircraft Systems*. Arlington, VA USA: IEEE, 2016. p. 702–710.

BARSK, K.-j. *Model Predictive Control of a Tricopter*. Master Thesis — University of Linköpings, Linköpings, Sweden, 2012.

BELLMAN, R. *Dynamic Programming*. Mineola: Dover, 2003.

BITTANTI, S.; BOLZERN, P. Stabilizability and detectability of linear periodic systems - addendum. *Systems and Control Letters*, v. 6, n. 1, p. 141–145, 1985. DOI:<https://doi.org/10.1016/0167-6911(85)90083-0>.

BOUABDALLAH, S. *Design and Control of Quadrotors With Application To Autonomous Flying*. Phd Dissertation — École Polytechnique Fédérale De Lausanne, À La Faculté Des Sciences Et Techniques De L'Ingénieur, Lausanne, France, 2007.

BOUABDALLAH, S.; NOTH, A.; SIEGWART, R. PID vs LQ control techniques applied to an indoor micro quadrotor. In: *IEEE Int. Conf. on Intelligent Robots and Systems*. Sendai, Japan: [s.n.], 2004. v. 3, p. 2451–2456.

BROWN, E. *BeagleBone Green drops the HDMI....and the price*. 2018. Accessed in: 2018-01-24. Disponível em: <http://linuxgizmos.com>.

BURNS, R. S. *Advanced Control Engineering*. 1st. ed. Oxford, UK: Butterworth Heinemann, 2001. 465 p. ISBN 0-7506-5100-8.

CASTELLANO, F. *Commercial Drones Are Revolutionizing Business Operation*. 2019. Accessed in: 2019-24-01. Disponível em: <https://www.toptal.com/finance/market-research-analysts/drone-market>.

CHIPPERFIELD, A. J. et al. A Genetic Algorithm Toolbox for Matlab. In: *Proceedings of the Tenth International Conference on Systems Engineering (ICSE '94)*. Coventry, UK: [s.n.], 1994. p. 200–207.

CONROY, J. et al. Characterization and enhancement of micro brushless DC motor response. In: *SPIE 9083, Micro- and Nanotechnology Sensors, Systems, and Applications VI*. Baltimore, Maryland, United States: [s.n.], 2014.

CORKE, P. A Robotics Toolbox for Matlab. *IEEE Robotics and Automation Magazine*, v. 3, n. 1, 1996. DOI:<https://doi.org/10.1109/100.486658>.

CUTLER, M. et al. Comparison of Fixed and Variable Pitch Actuators for Agile Quadrotors. In: *AIAA Guidance, Navigation, and Control Conf.* Portland, Oregon USA: [s.n.], 2011. p. 1–17.

DAVIDSON, E.; GOLDENBERG, A. Robust control of a general servomechanism problem: The servo compensator. *Automatica*, Elsevier, v. 11, p. 61–471, 1975. DOI:<https://doi.org/10.1016/0005-1098(75)90009-6>.

DU, G. X. et al. Controllability analysis for multirotor helicopter rotor degradation and failure. *Journal of Guidance, Control, and Dynamics*, v. 38, n. 5, p. 978–984, 2015. ISSN 15333884. DOI:<https://doi.org/10.2514/1.G000731>.

FAHLSTROM, P. G.; GLEASON, T. J. *Introduction to UAV Systems*. Fourth edi. Chichester, UK: John Wiley & Sons, INC, 2012.

FERREAU, H. et al. qpOASES: A parametric active-set algorithm for quadratic programming. *Mathematical Programming Computation*, v. 6, n. 4, p. 327–363, 2014. DOI:<https://doi.org/10.1007/s12532-014-0071-1>.

FRANCIS, B.; WONHAM, W. The Internal Model Principle of Control Theory. *Automatica*, Elsevier, v. 12, p. 457–465, 1976. DOI:<https://doi.org/10.1016/0005-1098(76)90006-6>.

FRANKLIN, G.; POWELL, J.; WORKMAN, M. *Digital control of dynamic systems*. 3rd. ed. Menlo Park CA: Addison-Wesley, 1998.

FRIEDLAND, B. *Control system design: an introduction to state-space methods*. Oxford, UK: Courier Corporation, 2012.

GASCO, P. S. *Development of a Dual Axis Tilt Rotorcraft UAV: Modelling, Simulation and Control*. 14–140 p. Master Thesis — Cranfield University, Bedford, UK, 2012.

HASSANALIAN, M.; ABDELKE, A. Classifications , applications , and design challenges of drones : A review. *Progress in Aerospace Sciences*, v. 91, n. April, p. 99–131, 2017. DOI:<https://doi.org/10.1016/j.paerosci.2017.04.003>.

HERNANDEZ-GONZALEZ, M.; ALANIS, A. Y.; HERNANDEZ-VARGAS, E. A. Decentralized discrete-time neural control for a Quanser 2-DOF helicopter. *Applied Soft Computing Journal*, Elsevier B.V., v. 12, n. 8, p. 2462–2469, 2012. ISSN 15684946. DOI:<https://doi.org/10.1016/j.asoc.2012.02.016>.

HUANG, H. et al. Aerodynamics and control of autonomous quadrotor helicopters in aggressive maneuvering. In: *IEEE Int. Conf. on Robotics and Automation*. [S.l.: s.n.], 2009. p. 3277–3282.

HWANGBO, J. et al. Control of a Quadrotor with Reinforcement Learning. *IEEE Robotics and Automation Letters*, v. 2, n. 4, p. 2096–2103, 2017. ISSN 23773766. DOI:<https://doi.org/10.1109/LRA.2017.2720851>.

JAFRI, M. H.; MANSOR, H.; GUNAWAN, T. S. Development of Fuzzy Logic Controller for Quanser Bench-Top Helicopter. In: *International Conference on Mechatronics*. Kuala Lumpur, Malaysia: IOP Conference Series, 2017. v. 260, n. 1. ISSN 1757899X.

JERONIMO, M. M. *Desenvolvimento de Arquitetura de Comunicação de uma aeronave multirrotora via Hardware in the Loop*. 148 p. Monography — Federal University of Uberlândia, Uberlândia, Brazil, 2019.

KENDOUL, F.; FANTONI, I.; LOZANO, R. Modeling and control of a small autonomous aircraft having two tilting rotors. *Proc. 44th IEEE Conf. on Decision and Control, and the European Control Conf.*, v. 2005, n. 6, p. 8144–8149, 2005. DOI:<https://doi.org/10.1002/ltl.370>.

KOCH, W. et al. Reinforcement learning for uav attitude control. *ACM Transactions on Cyber-Physical Systems*, v. 3, n. 2, 2019. ISSN 00741795.

KUMAR, A. *Single Board Computers – Rapberry Pi vs BeagleBone vs Arduino*. 2018. Accessed in: 2018-01-24. Disponível em: <http://www.thewindowsclub.com>.

KWAKERNAAK, H.; SIVAN, R. *Linear Optimal Control Systems*. New York: Wiley, 1972.

LAUSZUS, K. *TKJ Eletronics Kalman Filter*. 2017. Accessed in: 2021-09-12. Disponível em: <https://github.com/TKJElectronics/KalmanFilter>.

LAVRETSKY, E.; WISE, K. A. *Robust and Adaptive Control*. London: Springer London, 2013. 454 p. (Advanced Textbooks in Control and Signal Processing). ISBN 978-1-4471-4395-6.

LEE, D.; KIM, H. J.; SASTRY, S. Feedback linearization vs. adaptive sliding mode control for a quadrotor helicopter. *Int. Journal of Control, Automation and Systems*, v. 7, n. 3, p. 419–428, 2009. DOI:<10.1007/s12555-009-0311-8>.

LIU, Z. et al. Control techniques of tilt rotor unmanned aerial vehicle systems: A review. *Chinese Journal of Aeronautics*, Chinese Society of Aeronautics and Astronautics, v. 30, n. 1, p. 135–148, 2017. DOI:<10.1016/j.cja.2016.11.001>.

MACIEJOWSKI, J. *Model-Based Predictive Control*. Harlow: Prentice Hall, 2002.

MARQUES, F. M.; ASSIS, P. A. de; NETO, R. M. Position tracking of a tilt-rotor quad-copter with small attitude variation using model predictive control. In: *AIAA Aviation 2020 Forum*. Reston, VA, USA: [s.n.], 2020. p. 1–12.

MARQUES, F. M.; NETO, R. M.; SANCHES, L. Attitude and position control of a tilting rotor multi-copter. In: *25th COBEM*. Uberlândia, Minas Gerais, Brazil: [s.n.], 2019.

MARQUES, F. M. et al. Optimum trajectory tracking control of a multi-rotor aerial vehicle. In: *CILAMCE*. Florianópolis, Santa Catarina, Brazil: [s.n.], 2017.

MARQUES, F. M. et al. Modeling, control and hardware-in-the-loop simulation of a generic tilting multi-copter. In: *31st ICAS*. Belo Horizonte, Minas Gerais, Brazil: [s.n.], 2018.

MARQUES, F. M. M. *Modeling, Simulation and Control of a Generic Tilting Rotor Multi-Copter*. Master Thesis — Federal University of Uberlândia, Uberlândia, Brazil, March 2018.

MARQUES, F. M. M. Closed-Loop Poles and Zeros Analysis of a Multi-Copter System Endowed with Tilting Mechanisms. *Dynamics of Mechanical Systems: A Perspective from the LMEST-UFU*, v. 1, n. 1, p. 97–111, 2019.

MORRIS, S. Design and flight test results for micro-sized fixed-wing and VTOL aircraft. In: *Proceedings of the First International Conference on Emerging Technologies for Micro Air Vehicles*. Atlanta, GA: [s.n.], 1997.

NEMATI, A.; KUMAR, M. Modeling and Control of a Single Axis Tilting Quadcopter. In: *American Control Conf.* Portland, Oregon, USA: [s.n.], 2014. p. 3077–3082. ISBN 9781479932740.

ONEN, A. S. et al. Modeling and controller design of a VTOL UAV. In: *2015 Int. Conf. on Unmanned Aircraft Systems*. Denver, Colorado USA: [s.n.], 2015. p. 329–337. ISBN 9781479960101. DOI:<https://doi.org/10.1109/ICUAS.2015.7152307>.

OOSEDO, A. et al. Large attitude change flight of a quad tilt rotor unmanned aerial vehicle. *Advanced Robotics*, v. 30, n. 5, p. 326–337, 2016. ISSN 15685535.

PANDEY, V. K.; KAR, I.; MAHANTA, C. Controller design for a class of nonlinear MIMO coupled system using multiple models and second level adaptation. *ISA Transactions*, Elsevier Ltd, v. 69, p. 256–272, 2017. ISSN 00190578. DOI:<https://doi.org/10.1016/j.isatra.2017.05.005>.

PAPACHRISTOS, C.; ALEXIS, K. Dual–authority thrust–vectoring of a tri–tiltrotor employing model predictive control. *Journal of Intellingent Robot Systems*, p. 471–504, 2016.

PI, C. H. et al. Low-level autonomous control and tracking of quadrotor using reinforcement learning. *Control Engineering Practice*, Elsevier Ltd, v. 95, n. August 2019, p. 104222, 2020. DOI:<https://doi.org/10.1016/j.conengprac.2019.104222>.

QUANSER. *Quanser Inovate Educate*. 2020. Accessed in: 2020-03-25. Disponível em: <https://www.quanser.com/products_category/aerospace/>.

RICH, M. *Model development, system identification, and control of a quadrotor helicopter*. Master Thesis — Iowa University, Ames, Iowa, USA, 2012.

ROSSITER, J. *Model- Based Predictive Control*. [S.l.]: Taylor & Francis e-Library, 2005.

RYLL, M.; BICEGO, D.; FRANCHI, A. Modeling and control of FAST-Hex : a fully–actuated by synchronized–tilting hexarotor. In: *IEEE/RSJ Int. Conf. on Intelligent Robots and Systems*. Daejeon, Korea: IEEE, 2016. p. 1689–1694. ISBN 9781509037629.

RYLL, M.; BÜLTHOFF, H. H.; GIORDANO, P. R. Modeling and control of a quadrotor UAV with tilting propellers. In: *IEEE Int. Conf. on Robotics and Automation*. Saint Paul, Minnesota, USA: [s.n.], 2012. p. 4606–4613.

SANDERSON, C.; CURTIN, R. Armadillo: a template-based C++ library for linear algebra. *Journal of Open Source Software*, v. 1, p. 26, 2016.

ŞENKUL, A. F.; ALTUG, E. System Design of a Novel Tilt-Roll Rotor Quadrotor UAV. *Journal of Intelligent and Robotic Systems: Theory and Applications*, p. 575–599, 2016.

SERVAIS, E.; D'ANDREA-NOVEL, B.; MOUNIER, H. Ground control of a hybrid tricopter. In: *Int. Conf. on Unmanned Aircraft Systems*. Denver, Colorado USA: [s.n.], 2015. p. 945–950.

SICILIANO, B. et al. *Robotics: Modelling, Planning and Control*. London, UK: Springer, 2009.

SMEUR, E. J.; CROON, G. C. de; CHU, Q. Cascaded incremental nonlinear dynamic inversion for MAV disturbance rejection. *Control Engineering Practice*, Elsevier Ltd, v. 73, n. January, p. 79–90, 2018. ISSN 09670661. DOI:<https://doi.org/10.1007/s38313-018-0128-z>.

SMITH, S. *Digital signal processing: a practical guide for engineers and scientists*. [S.l.]: Elsevier, 2013.

SRIDHAR, S. et al. Tilt-rotor quadcopter xplored: Hardware based dynamics, smart sliding mode controller, attitude hold wind disturbance scenarios. In: *American Control Conference*. Philadelphia, PA, USA: IEEE, 2019. v. 2019-July, p. 2005–2010. ISBN 9781538679265. ISSN 07431619.

SUIÇMEZ, E. C. *Trajectory Tracking of a Quadrotor Unmanned Aerial Vehicle (UAV) VIA Attitude and position control*. Master Thesis — Midle East Technical University, Ankara, Turkey, July 2014.

SUMANTRI, B.; UCHIYAMA, N.; SANO, S. Least square based sliding mode control for a quad-rotor helicopter and energy saving by chattering reduction. *Mechanical Systems and Signal Processing*, Elsevier, v. 66-67, p. 769–784, 2016. ISSN 10961216. DOI:<https://doi.org/10.1016/j.ymssp.2015.05.013>.

TARIFA, I. O. et al. Tri-rotor tilted uav control and stability investigations based on the nonlinear dynamic inversion technique. In: *CILAMCE*. Florianópolis, Santa Catarina, Brazil: [s.n.], 2017.

WEN, F. H.; HSIAO, F. Y.; SHIAU, J. K. Analysis and management of motor failures of hexacopter in hover. *Actuators*, v. 10, n. 3, p. 1–29, 2021. ISSN 20760825.

YANG, Y. et al. Aerodynamic and aeroacoustic performance of an isolated multicopter rotor during forward flight. *AIAA Journal*, v. 58, n. 3, p. 1171–1181, 2020. ISSN 00011452. DOI:<https://doi.org/10.2514/1.J058459>.

YOON, S. et al. Computational aerodynamic modeling of small quadcopter vehicles. In: *AHS International The Vertical Flight Technical Society 73rd Annual Forum & Technology Display*. Forth Worth, Texas, USA: The Vertical Flight Society, 2017. p. 371–386. ISSN 15522938.